Numerical simulations of coupled processes in rock fractures

zur Erlangung des akademischen Grades eines

Doktors der Naturwissenschaften

von der Fakultät für Bauingenieur-, Geo- und Umweltwissenschaften
des Karlsruher Instituts für Technologie (KIT)

genehmigte

Dissertation

von

M.Sc. Tobias Kling

aus Bruchsal

Tag der mündlichen Prüfung:
12. Januar 2018

Referent: Prof. Dr. habil. Philipp Blum
Korreferent: Prof. Dr. habil. Christoph Butscher

Karlsruhe 2018

To my beloved parents,
Klaus und Birgit Kling

Abstract

Reservoir models are essential to assess the potential and risks of geothermal energy production. A significant limitation of reliable reservoir models is the availability of the required fracture parameters, which are often based on simplistic or lacking approaches or require too elaborate experimental setups. In order to define realistic fracture properties it is necessary to understand and quantify the underlying (often coupled) thermal, hydraulic, chemical and mechanical (THCM) processes by developing efficient and practical fracture analysis methods. To address these requirements, three independent approaches are introduced in this thesis:

In study 1, a novel and free web application-based contact mechanical approach, which considers elastic and elastic-plastic contact deformations within fractures, is introduced and validated for uniaxial laboratory tests on a circular granodiorite fracture. The simulation results show that particularly the elastic-plastic model fits well with experimental normal closure results. In contrast to other fast and easy-to-apply contact models, both the elastic and elastic-plastic models also consider the realistic representation of contact areas (< 2 % at a load of 10 MPa) and heterogeneous local closure. Although there is a general resistance to pronounced non-elastic deformation (even at 10 MPa), which is also confirmed by the newly derived relative hardness value of 0.14 for granitic rocks, local contact stresses confirm the higher validity of the elastic-plastic contact model.

In study 2, a novel approach based on non-destructive, *in situ* medical X-ray compute tomography (CT) scans is presented, which is appropriate to numerically approximate actual fluid flow in smooth fractures with small apertures (< 35 μm). The results are validated by applying flow through experiments of a fractured sandstone sample under loading/unloading conditions, which are performed simultaneously to the CT scans. Deviations from the experimental fluid flow results are caused by inevitable errors during the aperture calibration, rock matrix effects and resolution-caused limitations. Despite these deviations, flow simulations indicate significant stress-dependent flow channeling and permanent or temporary closure of single channels, whereas more pronounced changes of the flow regime must occur at scales below the CT resolution ($0.5 \times 0.5 \times 1.0$ mm³).

In study 3, a phase-field model of hydrothermal quartz growth is applied to investigate the influence of sealing geometries on the hydraulic properties of fractures. It is shown that fluid flow in partially sealed fractures highly depends on the crystal habit of the precipitated minerals. For more elongated ('needle') crystal geometries typically crystal bridges evolve, which form distinct flow barriers and facilitate the evolution of hydraulic fracture properties resembling a porous media. Based on the flow

simulations a novel semi-empirical equation to estimate hydraulic fracture properties of partially sealed fractures is established.

Within the scope of this thesis, three easy-to-apply approaches are introduced, which are the basis for further fracture research and can be used for different fracture issues. The web application represents a fast and free method, which can be used to study stress-dependent fracture normal closure based on conventional surface scanning methods, even for drill core samples. The proposed non-destructive medical CT scan approach can be useful, for example, to estimate hydraulic properties of tightly-closed, chemically altered fractures. The newly established equation in the third study provides a more effective alternative to common hydraulic aperture models, which can be used to straightforwardly estimate the hydraulic properties of partially sealed fractures.

Kurzfassung

Reservoirmodelle sind unerlässlich, um das Potential und Risiken bei der Gewinnung geothermischer Energie zu beurteilen. Eine wesentliche Einschränkung zuverlässiger Reservoirmodelle ist jedoch die Verfügbarkeit benötigter Kluftparameter, die oftmals auf allzu einfachen oder auch fehlenden Methoden beruhen oder extrem aufwändige experimentelle Aufbauten benötigen. Um passende Klufteigenschaften zu definieren, ist es daher nötig, die zugrundeliegenden (oftmals gekoppelten) thermischen, hydraulischen, chemischen und mechanischen (THCM) Prozesse zu verstehen und zu quantifizieren, indem man wirkungsvolle, aber anwendungsorientierte Methoden zur Kluftanalyse entwickelt. Um diese Erfordernisse anzugehen, werden in dieser Arbeit drei voneinander unabhängige Herangehensweisen vorgestellt:

In Studie 1 wird ein kontaktmechanischer Ansatz basierend auf einer neuartigen, frei zugänglichen Web-Anwendung, die sowohl elastische als auch elastisch-plastische Kontaktdeformation innerhalb der Kluft betrachtet, vorgestellt und anhand von Uniaxialtests an einer kreisrunden Granodiorit-Kluft validiert. Die Simulationsergebnisse zeigen, dass insbesondere der elastisch-plastische Ansatz eine gute Übereinstimmung mit den Ergebnissen der experimentellen Normalverschiebung aufweist. Im Gegensatz zu anderen schnellen und leicht anwendbaren Kontaktmodellen, berücksichtigen sowohl das elastische als auch das elastisch-plastische Model eine realitätsnahe Wiedergabe der Kontaktbereiche (< 2 % bei 10 MPa Auflast) und das Auftreten ungleichmäßiger lokaler Vertikalversätze. Obwohl ein genereller Widerstand gegen ausgeprägte nicht-elastische Deformation (sogar bei 10 MPa) zu beobachten ist, was auch durch die neu hergeleitete relative Härte von 0.14 bekräftigt wird, bestätigen die lokalen Kontaktbelastungen die höhere Validität des elastisch-plastischen Kontaktmodels.

In Studie 2 wird eine neuartige Vorgehensweise, basierend auf zerstörungsfreien *in situ* Scans mittels medizinischer Computertomografie (CT), vorgestellt, die sich als geeignet erweist um den Fluidfluss in weniger rauen Klüften mit kleinen Öffnungsweiten (< 35 μm) annäherungsweise numerisch zu bestimmen. Die Ergebnisse werden anhand von Durchflussexperimenten an einer geklüfteten Sandsteinprobe unter Be- und Entlastungsbedingungen validiert, die zeitgleich zu der CT-Scans durchgeführt wurden. Abweichungen von den experimentellen Durchflussergebnissen sind bedingt durch unvermeidbare Abweichungen während der Kalibrierung der Öffnungsweiten, durch Einflussnahme der Gesteinsmatrix und durch die grobe Auflösung des CT Geräts. Trotz dieser Abweichungen, zeigen die Simulationen ein ausgeprägtes lastabhängiges Fließverhalten („Channeling“) und ein permanentes oder vorübergehendes Schließen einzelner Fließwege, wobei deutlichere Änderungen des Fließregimes unterhalb der Auflösung ($0.5 \times 0.5 \times 1.0$ mm³) der CT-Scans zu erwarten sind.

In Studie 3 wird ein Phasenfeld-Model für hydrothermalbedingten Quarzwachstum angewandt, um den Einfluss der entstehenden Fällungs-Geometrien auf die hydraulischen Eigenschaften von Klüften zu untersuchen. Es wird gezeigt, dass der Fluidfluss in teilweise mineralisierten Klüften deutlich abhängig vom Kristallhabitus der ausgefällten Minerale ist. Für eher gestreckte Kristalle entwickeln sich typischerweise sogenannte „Kristallbrücken“, die ausgeprägte Fließbarrieren bilden und die Bildung von hydraulischen Klufteigenschaften begünstigen, die denen eines porösen Medium ähneln. Auf Basis der Strömungssimulationen kann eine neuartige semi-empirische Gleichung hergeleitet werden, um die hydraulischen Eigenschaften von teilweise mineralisierten Klüften abzuschätzen.

In Rahmen dieser Thesis werden somit drei einfach anwendbare Methoden vorgestellt, welche die Grundlage für weitere Untersuchungen an Klüften darstellen und für verschiedenartige Kluft-Fragestellungen verwendet werden können. Die Web-Anwendung stellt eine schnelle und frei zugängliche Methode dar, die genutzt werden kann, um die druckabhängige Normalverschiebung von Klüften basierend auf herkömmlichen Oberflächenscans zu untersuchen. Der vorgeschlagene zerstörungsfreie Ansatz für medizinische CT-Scans ist sinnvoll, um beispielsweise die hydraulischen Eigenschaften von dicht verschlossenen, chemisch alterierten Klüften abzuschätzen. Die neu hergeleitete Gleichung der dritten Studie liefert eine effizientere Alternativlösung zu herkömmlichen Modellen, die zur Bestimmung der hydraulischen Kluftöffnungsweite entwickelt wurden, und kann genutzt werden, um die hydraulischen Eigenschaften von teilweise mineralisierten Klüften relativ unkompliziert abzuschätzen.

Table of Contents

Chapter 1

Introduction

1.1 Fractures and geothermal energy production

Geothermal energy represents a natural, renewable and ubiquitous resource, which can meet the base load demand and also provides the benefit of the utilization of decentralized, inconspicuous and low-emission power plants (Meller et al. 2017). Besides this benefit of indirect use, geothermal energy also stands out because of its direct utilization options, where the produced heat energy can be used immediately or in cascade for district heating or agricultural and industrial purposes (Rubio-Maya et al. 2015). Although there are different theoretical estimations for the potential of geothermal power production in Germany, which range between two orders of magnitude (Paschen et al. 2003; BMU 2007; Jain et al. 2015), all these studies predict a potential energy supply significantly above the total energy demand (527 TWh) of 2016 (BNetzA 2017).

Generally, deep geothermal reservoir types can be distinguished in hydrothermal and enhanced geothermal systems, whose applicability always relies on the presence of fractures, which affect the hydraulic reservoir properties such as permeability or transmissivity. Typical reservoir types are schematically summarized in Fig. 1.1 and explained hereafter.

One preferred target for hydrothermal energy production are fractured-porous media such as sandstones (Fig. 1.1), which can feature high matrix permeability (up to 10^{-12} m²; Moeck 2014). However, such rocks often are associated with facies changes, so that matrix permeabilities can vary by several orders of magnitude due to varying grain size distributions, compaction, cementation and the abundance of detrital clays (Stober and Jodocy 2009; Singhal and Gupta 2010; Soyk 2015; Weibel et al. 2017). Hence, naturally occurring fractures, which can provide additional fluid pathways and enhance the (cumulative) rock mass permeability, are often decisive for the feasibility of a geothermal project. Existing fracture systems can cause an increase in permeability by several orders of magnitude (Stober and Jodocy 2009; Singhal and Gupta 2010). However, pronounced double-porosity (contributions to storativity) and/or double-permeability (contributions to overall fluid flow) of these aquifers also increase the hydraulic complexity of the reservoir (Berkowitz 2002; Singhal and Gupta 2010).

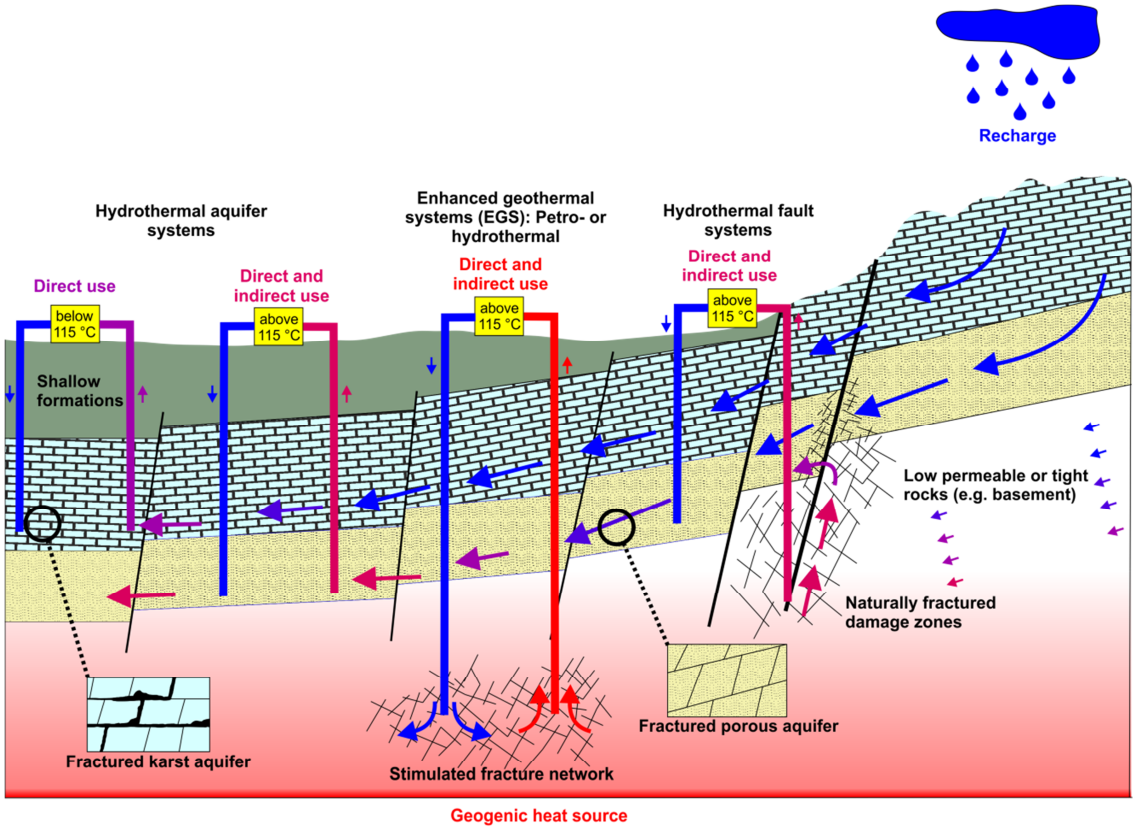

Fig. 1.1: Examples of naturally and artificially fractured geothermal reservoirs and how these reservoirs can be used with respect to their fluid temperatures.

Further hydrothermal aquifers are provided by karstic and fractured carbonate rocks (Fig. 1.1), which make up a major part of the realized geothermal project in Germany (Goldbrunner 2014). In particular, the Malm-aquifers of the southern German Molasse basin is the preferred reservoir for direct and also indirect geothermal utilization (Goldbrunner 2014). High permeabilities up to 10^{-11} m² at suitable depths can be assigned to the triple porosity of the karst aquifer (Steiner et al. 2014). However, the interaction of dissolution conduits, fractures and the matrix-porosity causes highly heterogeneous and complex flow fields in these aquifers (Ghasemizadeh et al. 2012; Steiner et al. 2014). Fractures in the fractured karst aquifers not only provide an important feature for recent fluid flow, but were also substantial for the prehistoric development of karst features by providing flow paths and reactive surfaces for carbonate dissolution (Goldscheider and Drew 2007; Ghasemizadeh et al. 2012; Xanke 2017).

A third type of hydrothermal systems is provided by active deep-reaching faults and/or their fractured damage zones (Fig. 1.1), which deliver hot fluids to shallower, more economical depths (López and Smith 1995; Schmidt et al. 2016; Agemar et al. 2017). Such a fault-zone-related rise of thermal fluids is the basis for some geothermal projects (e.g. Bruchsal, Brühl, Insheim and Landau) in the Upper Rhine Graben (URG), which is characterized by its complex fault block structures (Sanjuan et al. 2016; Meier 2016).

Similar hydrothermal systems theoretically can be found in every tectonically active region, whereas the presence of the system does not guarantee an omnipresence of active fault zones, as is evident from geothermal projects in the URG (e.g. Bühl, Trebur). Targeted fault zones of these projects were filled with secondary minerals (e.g. phyllosilicates, quartz, gypsum or calcite) clogging the fault zones (Enerchange 2016; Schmidt et al. 2016; Agemar et al. 2017). Generally, the quality of hydrothermal fault systems strongly depends on the fault geometry, the stress-field, chemical fluid-rock interactions, mechanical rock properties and potential mixing with colder fluids (Curewitz and Karson 1997; Schmidt et al. 2016; Agemar et al. 2017).

It should be mentioned that in reality, not all hydrothermal reservoirs exactly match with a single reservoir type seen in Fig. 1.1) and are rather hybrids which reach higher production rates. For instance, the exploited hydrothermal fault systems in the URG, such as Bruchsal or Landau, are also located in the Buntsandstein aquifer. Fault zones also were the preferred target of many geothermal wells of the karstic Malm-aquifers, whereas their impact on productivity is still controversial (Steiner et al. 2014).

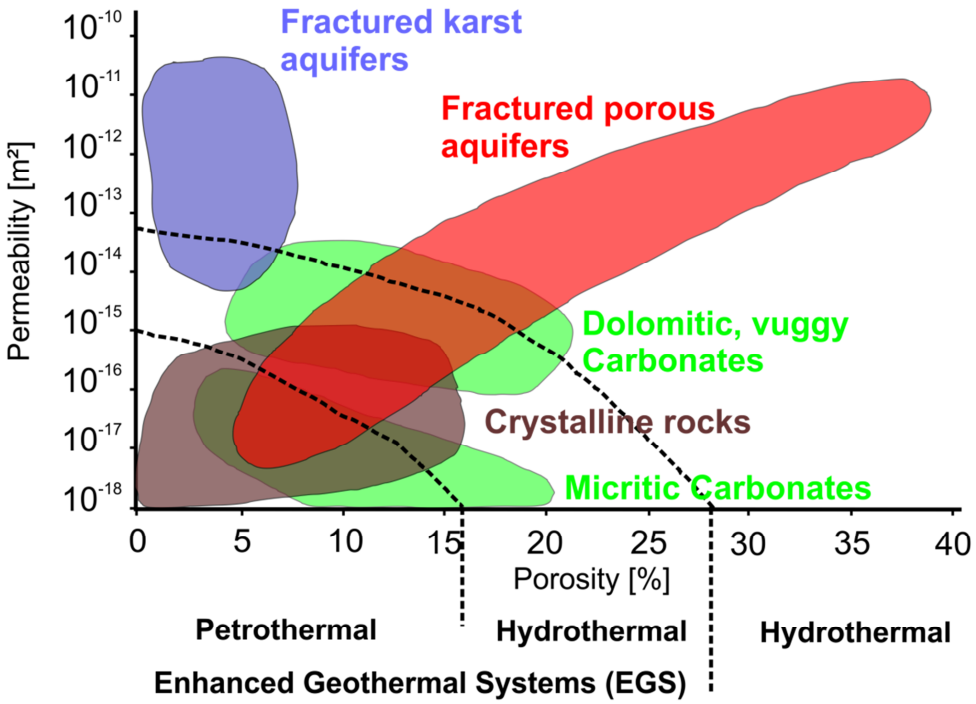

Fig. 1.2: Geothermal reservoir rock types and the effect of potential reservoir porosities and permeabilities on the characterization of the geothermal system types (after Moeck, 2014).

Enhanced geothermal systems (EGS) are naturally low-permeable reservoirs, which have to be enhanced by stimulating existing fractures or by generating new fractures. The stimulation (enhancement) of an

EGS strongly depends on the rock type and can be performed hydraulically, with gel-proppant mixtures or with hybrid slickwater treatment, which combines both aforementioned approaches (Schulte et al. 2010; Zimmermann and Reinicke 2010; Plenefisch et al. 2015). In terms of EGS, Moeck (2014) distinguishes between enhanced hydrothermal and petrothermal reservoir types, which are defined by their permeability and matrix porosity (Fig. 1.2). Similar to many unconventional hydrocarbon reservoirs, enhanced hydrothermal systems exploit low-permeable formations such as tight sandstones, dolomitic or vuggy carbonates and disrupted crystalline rocks (Moeck 2014). Petrothermal systems are defined by very low porosities and permeabilities (Moeck 2014) so that producible fluids are virtually absent and non-reservoir fluid has to be injected (Fig. 1.1). Typical EGS sites are the *in situ* downhole laboratory Groß Schönebeck, which exploits Rotliegend sandstones in the North German Basin (Moeck 2014) and petrothermal EGS pilot site Soultz-Sous-Forêt in the French part of the URG, where granitic rocks were hydraulically stimulated (Dorbath et al. 2009; Vidal et al. 2015).

1.2 Impacts of rock fractures

The presence of fractures does not unconditionally imply high production rates, but only indicates potential targets. Moreover, reservoir performance strongly depends on the fracture pattern complexity, which ideally forms an interconnected fracture network (Singhal and Gupta 2010), and features a significant hydraulic and mechanical anisotropy (Zhang and Sanderson 1995; Kulatilake and Panda 2000; Dietrich et al. 2005; Blum et al. 2007; Kohl and Mégel 2007; Müller et al. 2010). Understanding this fracture-related anisotropy is crucial when planning standardly applied directional drilling programs targeting the hydraulically most effective fractures in the reservoir (Nelson 2001; Stober and Jodocy 2009).

Apart from that, during the operation of geothermal wells (production or injection), fractured reservoirs are highly sensitive to often coupled thermal, hydraulic, chemical and mechanical (THCM) processes. Resulting fracture opening or closing and related fracture-matrix interactions, which are highly related to the matrix porosity and permeability, can have significant impacts on heat and fluid transfer (Pruess 1983; Singhal and Gupta 2010; Heinze and Hamidi 2017) and significantly contribute to the sustainability of a geothermal project.

In addition, there are also security aspects. Rock fractures can be related to potential rock swelling mechanisms in clay-sulfate rocks, which can cause a significant uplift of the surface (Butscher et al. 2016). Of course, such formations are not the primary target for deep geothermal energy production, but can be involved during well drilling due to inappropriate planning or surveillance. The shallow geothermal

drillings in Staufen and Lochwiller in the URG are examples of this unintended consequence (Fleuchaus and Blum 2017). During well drilling, fractures also play an important role concerning lost circulation of drilling "muds", which can infiltrate into intersected permeable reservoirs and implicate economical losses and eventual groundwater contaminations (Dannwolf et al. 2014). Furthermore, the fracture propagation during hydraulic stimulation theoretically can affect adjacent formations, which do not act as hydraulic or mechanical barriers and thus facilitates potential hydraulic short circuits (Dannwolf et al. 2014; Plenefisch et al. 2015). Hydraulic stimulations also are associated with stress and strain changes in the rock mass and along the fractures themselves (Gaucher et al. 2015; Vogler 2016). These changes can cause a hydro-mechanically (HM) coupled response of the reservoir, which triggers induced seismic events due to the resulting slip of pre-existing fractures (Baisch et al. 2010; McClure and Horne 2011; Vogler 2016). Although measured magnitudes of induced seismic events in Germany were relatively low (local magnitudes $M_L < 3.0$) compared to events that were induced by salt mining, coal mining or gas exploration in the past, higher magnitude events in Basel/Switzerland ($M_L < 3.4$) and St. Gallen/Switzerland ($M_L < 3.5$) bequeathed negative connotations (Plenefisch et al. 2015).

Consequently, numerical models of fractured reservoirs are essential to the execution of geothermal projects. Reliable reservoir models reduce capital expenditure and exploration risks and play an important role in forecasting, monitoring or preventing potential environmental risks (Gaucher et al. 2015).

1.3 Fractures network models

As recently stated by Alghalandis (2017) fracture network modelling and subsequent coupled or decoupled THCM simulations are a relatively young geoscientific discipline, which however have become increasingly important due to the rapid developments in computer sciences. Typically, there are different scales of fracture-related problems, which can range from the laboratory scale (single fracture), over the local fracture network scale (between 10 and 100 m²) to the superior regional scale comprising entire fault network geometries (Faybishenko et al. 2003). Hence, for fractured reservoirs a special focus lies on the so-called upscaling, where fracture investigations often are based on small-scale (and short-time) laboratory or field tests that have to be extrapolated to assess the entire reservoir (Nelson 2001). However, fractured rock masses are often characterized by heterogeneous and complex network structures, which in turn comprise a finite number of heterogeneous fractures and fracture sets (Pollard and Aydin 1988; Schultz 2000; Nelson 2001; Lei et al. 2017). Thus, Faybishenko et al. (2003) adapted the concept of the hierarchical scales subdividing the fracture system in a graded series of subsystems, whereby each subsystem affects the next-higher subsystem. The uppermost subsystem in fractured reservoir modelling often depends on the study area and implies different model approaches, which can be distinguished as

continuum, discontinuum and hybrid multiple-continuum or discontinuum-continuum methods (Dietrich et al. 2005; Lei et al. 2017).

Continuum methods represent the computationally most efficient approach, however require a sufficiently large fractured system and the applicability of the representative elementary volume (REV) concept (Dietrich et al. 2005). The REV represents the smallest volume of the considered fractured rock mass beyond which a studied reservoir parameter remains mostly constant (Min et al. 2004; Dietrich et al. 2005; Blum et al. 2007; Müller et al. 2010). Due to size-scaling, anisotropic fracture alignments, single fracture properties and spatial clustering, the applicability of the REV is site-specific and relies on the considered scale, complexity and heterogeneity of the fractured system (Neuman 1988; Barton 1995; Kulatilake and Panda 2000; Min et al. 2004; Blum et al. 2005, 2007; Müller et al. 2010). Nevertheless, finding the REV requires more accurate and computationally intensive discontinuum-based methods (Neuman 1988; Kulatilake and Panda 2000; Min et al. 2004; Blum et al. 2005, 2007).

Consequently, there are still two fundamental issues with regard to discontinuum models (Lei et al. 2017): The geometrical representation of the local or regional fracture network and the modelling approach to solve fully or partially coupled THCM processes.

1.3.1 Discrete fracture networks

Computational models, which are generated to reflect representative subsurface fracture geometries and patterns, typically are called discrete fracture networks (DFN). Depending on the model dimension (Fig. 1.3), DFNs typically are described by different geometric properties such as the number of fracture sets, fracture density, fracture intensity, fracture spacing, fracture mean length, fracture length distribution and fracture orientation (Zeeb et al. 2013b; Alghalandis 2017).

Accordingly, there are generally four methods to find representative fracture patterns:

(1) **Deterministic** DFNs are directly mapped from analogous outcrops by image analysis (e.g. Zeeb et al. 2010; Healy et al. 2017; Lei et al. 2017).

(2) **Artificial** (stochastic or fractal) DFNs (Fig. 1.3) are commonly generated based on detailed fracture surveys providing the relevant statistical parameter of the fracture network (e.g. Blum et al. 2005, 2007; Davy et al. 2010; Harthong et al. 2012; Zeeb et al. 2013b; Alghalandis 2017; Lei et al. 2017).

(3) **Hybrid approaches** are combined artificial-deterministic DFNs, where randomly generated fractures are combined with real subsurface fractures derived from borehole logs or seismic interpretations (Rogers et al. 2010; Doe et al. 2013).

(4) **Geomechanical** DFNs do not only focus on the reproduction of existing fracture networks, but numerically reproduce the entire geomechanical fracture evolution with due regard to the geologically-inferred paleo-stress conditions (Lei et al. 2017 and references therein).

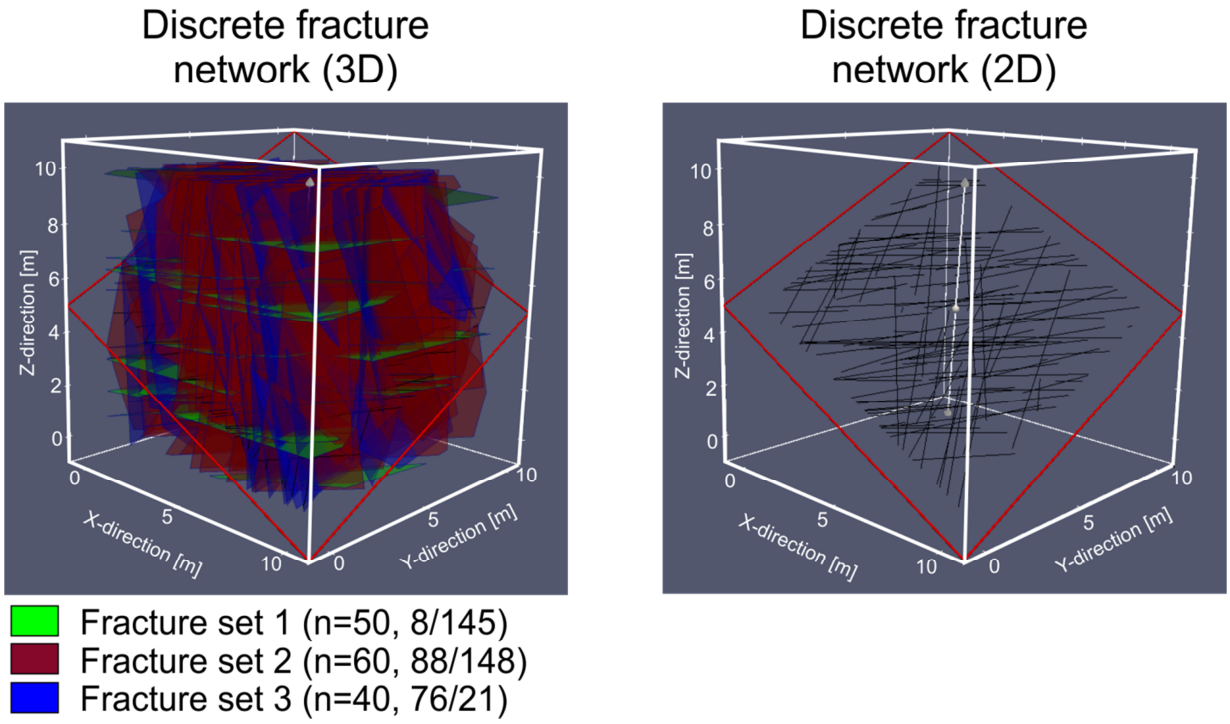

Fig. 1.3: Example of discrete fracture network (DFN) models containing three fracture sets in 3D and 2D. The 3D DFN is generated by using the open source MATLAB-code ADFNE (Alghalandis 2017). The 2D model represents a slice of the 3D model reproduced by applying the open-source visualization software ParaView (Ayachit 2015)

1.3.2 Reservoir simulations

The choice of an appropriate simulation approach most often relies on the underlying coupled or uncoupled (THCM) processes and the scale and complexity of the DFN. Thus, there are various numerical codes for DFN-based reservoir simulations (e.g. Jing 2003; Jing and Stephansson 2007; Rutqvist et al. 2009; Rutqvist 2011; Lisjak and Grasselli 2014; Steefel et al. 2015; Lei et al. 2017). However, most of these approaches only consider 2D problems or refer to "loosely coupled problems" as argued by Cacace and Jacquey (2017). Such a "loosely coupled" approach, for example, is applied by Rutqvist et al. (2013), who combine TOUGH2 for fluid flow, FLAC for rock mechanics and MINC for particle transport to simulate stress-dependent solute transport in fractured rocks. Up-to-now, there are only a few applications providing a system of fully coupled equations to solve TH(C)M problems in 3D fractured rock masses such as GEOS (Vogler 2016; Settgast et al. 2017), GOLEM (Cacace and Jacquey 2017) or REDBACK

(Poulet et al. 2017). Furthermore, there are also first computationally intensive rough-walled (RW-)DFN simulations, which are applied for (uncoupled) fluid flow simulations focusing on the interaction of heterogeneous fracture flow (Watanabe et al. 2011; Ishibashi et al. 2012; Jing et al. 2017; Kirkby and Heinson 2017).

Due to the computational requirements of RW-DFNs, most DFN simulations still rely on simplified approaches, where fractures are considered as continuous "joint elements", discrete "parallel plates" or pipe networks (e.g. Alghalandis 2017; Lei et al. 2017). These approaches require input parameters referring to representative hydraulic or mechanical fracture properties. Hence, investigations on single fractures are essential to understand fracture hydraulics and to transfer the findings into DFN simulation to obtain more reliable simulation outputs.

1.4 Single fractures

There are many definitions for the term "fracture" in geosciences, which most often reflects the different interests of the authors (Nelson 2001). In this thesis, the term "fracture" refers to the definition of Jaeger et al. (2007) and can be described as a discontinuity, which divides an intact rock mass in two parts due to brittle failure. In contrast to faults, which can be described as large-scale fractures, only little or no transverse displacement occurs along fractures. On a mechanical view, fractures can be subdivided into three generic types (Bons et al. 2012):

- **Mode I** (also tensile, extension or opening fracture): The displacement vector is perpendicular to the fracture plane
- **Mode II** (also in-plane shear or sliding fracture): The displacement vector is parallel to the fracture plane and parallel to the propagation direction.
- **Mode III** (also out-of-plane shear or tearing fracture): The displacement vector is parallel to the fracture plane and perpendicular to the propagation direction.

Mode II and mode III often are summarized as shearing fractures (Bons et al. 2012). In this thesis, mode I fractures are called tensile fractures. Fractures, which combine both tensile and shearing characteristics are termed hybrid or oblique opening fractures (Bons et al. 2012).

In fractured reservoirs typically not only a single generic fracture types occurs. Which types occur and how these features contribute to the entire fractured system, relies on the tectonic history, the state of stress and underlying processes at the time of fracturing (Nelson 2001). Hence, fault- or fold-related fractures typically are very complex and form dense networks of both shearing and tensile fractures. In

contrast, regional fractures often are tensile and reveal more consistent and simple geometries (Nelson 2001).

Additional to their mechanical genesis, Nelson (2001) also classifies fractures by their internal morphology and distinguishes between:

- **Open fractures**, which are fractures without any deformational or diagenetic material fillings and typically have a positive effect on the reservoir permeability (Nelson 2001).
- **Deformed fractures**, which are strongly altered due to pronounced shearing so that the fractures are filled with gouge, polished (slickensides) or a combination of both and often are associated with low fracture permeabilities (Nelson 2001).
- **Mineral-filled fractures,** which are extremely common and can be partially or completely filled by secondary minerals such as quartz, calcite or sulphides (Nelson 2001). Fractures, which are completely filled (or sealed) are called veins and form significant flow barriers (Nelson 2001; e.g. Bons et al. 2012).
- **Vuggy fractures,** which are caused by fluid-flow related dissolution processes inside the fracture and typically indicate an increased fracture permeability (Nelson 2001).

In rock fracture studies, there is also a further separation between natural (real), artificial (man-made or induced) and synthetic (computer-generated) fractures (e.g. Glover et al. 1998).

1.4.1 Fracture properties

Although there are many different fracture types, most of these fractures have in common that they consist of two opposing surfaces, which are rough to a certain degree and typically form a heterogeneous field of voids and contacts. The resulting morphology defines the geometric, mechanical and hydraulic fracture properties, which are essential for subsequent (coupled) THCM processes inside the fracture. The most important fracture properties are summarized by Hakami (1995) and are listed hereafter. Typically, these features are tightly coupled to each other (e.g. Pyrak-Nolte 1996; Pyrak-Nolte and Morris 2000):

- **Aperture:** Refers to the varying local distance (void space or gap) in the z-direction of the referring fracture and its x-y plane (Fig. 1.4a). Apertures used for DFN simulations or analytical solutions typically refer to the mean of the local aperture distribution.
- **Roughness:** Refers to the unevenness or smoothness of the fracture surfaces or aperture distribution (Fig. 1.4a). There are various roughness parameters used in the geoscientific

community (e.g. Belem et al. 2000; Li and Zhang 2015; Kling et al. 2017), whose choice generally depends on the subsequent numerical or analytical utilization. Typically, fractures comprise a primary (large-scale waviness or undulation) and a secondary (small-scale unevenness) roughness component, which can have different effects on fracture flow and mechanics (e.g. Tatone and Grasselli 2012a; Zou et al. 2015).

- **Contact area:** Refers to those fracture surface asperities, which are in contact (Fig. 1.4a). Contact areas are quantified as the ratio of the total area of real contact and the total fracture surface area. However, it is difficult to quantify the actual contact area of the rock surface because transitions between contacting and non-contacting areas strongly depend on experimental quantification methods, numerical contact mechanical models and corresponding fracture morphology measurements, which often cause a blurring of actual contacts (Hakami 1995; Dieterich and Kilgore 1996).

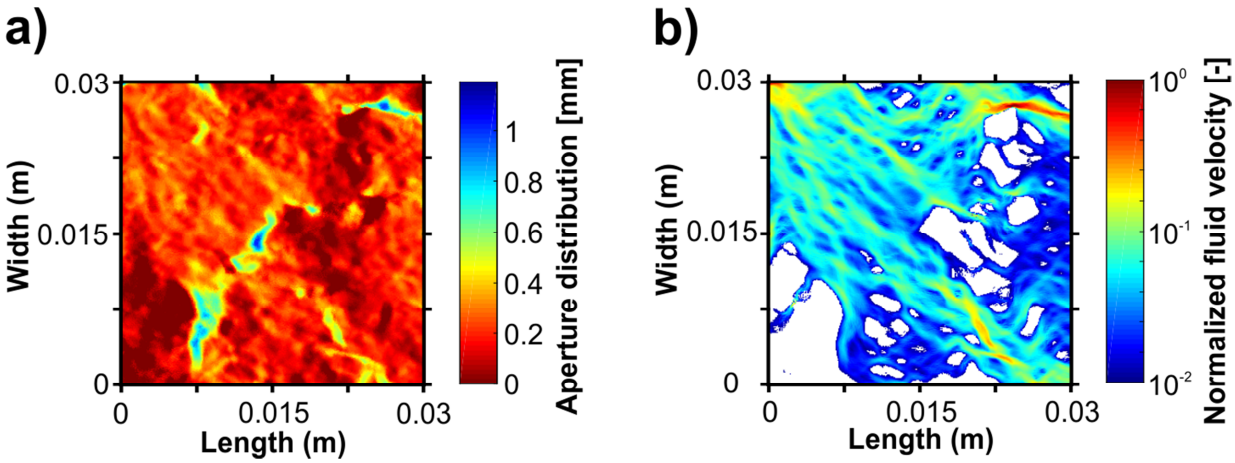

Fig. 1.4: Example of rough rock fracture with a heterogeneous aperture distribution and contact areas (a) and a potential resulting flow field featuring tortuous flow channels (b). Both figures are based on photogrammetric scans of an altered granodiorite sample for the Aspö Hard Rock Laboratory (Sweden). The normalized fluid velocities are calculated by using the classical local cubic law (LCL) approach (e.g. Brush and Thomson 2003).

- **Channeling / Tortuosity:** Refers to the flow pattern inside the heterogeneous aperture field of the fracture and directly affects the hydraulic fracture properties. Locally varying flow velocities facilitate local paths of least resistance so that most of the fluid flows along preferred and often interconnected flow paths (Fig. 1.4b; Tsang 1984; Tsang and Tsang 1989; Hakami 1995; Tsang and Neretnieks 1998). Due to the heterogeneity of local apertures, these channels are not straight-lined, but undulate through the fracture (Fig. 1.4b). The resulting relative deviation from the theoretically shortest (straight-lined) flow path is called the geometric tortuosity (Ghanbarian et al. 2013). How the tortuous channels evolve along the fracture highly depends on the anisotropy and

heterogeneity of the aperture field (Nemoto et al. 2009). Channeling also plays a significant role for the interconnectivity of different fractures in a DFN (Hakami 1995).

- **Matedness:** The matedness refers to the matching of two surfaces and describes their "pattern agreeness" or "fitness" (Zhao 1997). Although there are efforts to quantify the degree of matching (Zhao 1997), the term "matedness" often represents a descriptive measure, which affects the geometrical, mechanical and hydraulic fracture properties (Zhao 1997). For instance, Wu and Sharma (2017) indicate an logarithmic increase of mean apertures by progressively shifting surfaces of an initially mated fracture. It is worth mentioning that in nature fracture surfaces never will match perfectly, since most fracture surfaces experience individual mechanical or chemical alteration (e.g. Ogilvie et al. 2006; Schwarz and Enzmann 2013).

- **Spatial correlation:** Refers to the length over which a local fracture aperture value (or asperity height of a surface) is correlated with its neighbouring aperture (or asperity height) (Tsang and Stephansson 1996). Typically, there are various methods to quantify the spatial correlation such as statistical variogram or fractal analyses (Hakami and Larsson 1996; Candela et al. 2009). The spatial correlation provides information about matedness or mismatch of the fracture (Brown 1995; Hakami 1995; Hakami and Larsson 1996; Matsuki et al. 2006), but also provides information about scale-dependent fracture patterns. Variogram analyses of crystalline rock fractures show that correlation lengths typically are below one meter, which restricts upscaling to fracture patterns larger than 1×1 m² (Hakami and Larsson 1996; Vogler 2016; Vogler et al. 2016a). During fractal analyses, fracture surfaces are analysed for their statistical self-affinity and topothesy correlations, where latter co-determines the surface amplitudes (e.g. Schmittbuhl et al. 2008; Candela et al. 2009, 2012). For faults and fault-related fracture surfaces, self-affinity scaling has been found to be applicable over more than nine orders of magnitude from 5×10^{-5} to more than 5×10^{4} m, while topothesy correlations only show weak or no clear correlation (Brodsky et al. 2011; Candela et al. 2012; Renard and Candela 2017). Furthermore, spatial correlations can reflect morphological fracture anisotropies (Candela et al. 2009; Vogler et al. 2016a).

- **Stiffness:** Refers to the relationship between fracture surface displacement and applied shear or normal loads, and is strongly connected to the mechanical properties and roughness of the fracture (Bandis et al. 1983; Hopkins et al. 1987; Hopkins 2000; Pyrak-Nolte and Morris 2000). Generally, it can be distinguishes between the normal stiffness and shear stiffness. The normal stiffness can be evaluated from normal displacement experiments and describes the ratio of normal stress and normal displacement within a certain increment of the resulting stress-displacement curve (e.g. Goodman 1976; Campañá et al. 2011). Since the stress-displacement curve typically is non-linear, the normal stiffness is often expressed by the initial tangent of the curve (Bandis et al. 1983). The

shear stiffness can be evaluated from direct shear tests and represents the slope of the secant between the origin of the stress-displacement curve and the peak shear strength (Goodman 1976).

1.4.2 Determining hydraulic fracture properties

As mentioned above, most (recent) DFN-based reservoir simulations do or cannot directly account for real (rough) fracture geometries. Hence, representative hydraulic fracture properties such as the hydraulic aperture (Zeeb et al. 2013b; Alghalandis 2017) or the fracture permeability and transmissivity (Flemisch et al. 2017) often are important input parameters for DFN simulations.

Analytical approaches often are the simplest method to estimate hydraulic fracture properties, but also are the most inexact method because they often neglect important hydraulic, mechanical or chemical processes, which all are based on more complex rough fracture morphologies (Lang et al. 2016). One of the most common empirical approaches is defined by Barton et al. (1985), who defines the hydraulically effective aperture a_h as

$$a_h = \frac{a_m^2}{JRC^{2.5}} \tag{1.1}$$

where a_m is the (measurable) mechanical aperture and the joint roughness coefficient (JRC) characterizes the surface roughness. Additional approaches have followed, which all presume that the hydraulic aperture of a fracture mostly rely on few measurable geometric properties (e.g. Louis 1967; Renshaw 1995; Zimmerman and Bodvarsson 1996; Souley et al. 2015). Furthermore, various hydromechanical (HM) approaches are derived to estimate the stress-dependency of hydraulic fracture properties (e.g. Bandis et al. 1983; Ohnishi et al. 1996; Rutqvist and Stephansson 2003; Huo and Benson 2015). Furthermore, there are hydraulic aperture equations focusing on chemical alteration, which often rely on pure precipitation or dissolution kinetics in idealized “parallel plate” fractures (e.g. Lowell et al. 1993; Noiriel et al. 2007, 2013; Chen et al. 2014).

Laboratory experiments have the advantage that they offer a wide range of possible applications, particularly when considering coupled or uncoupled THCM processes in single fractures. Hydromechanically coupled experiments can be applied to quantify stress-dependent fracture flow, which generally decreases with increasing stress (Raven and Gale 1985; e.g. Brown 1987; Hakami and Larsson 1996; Watanabe et al. 2008, 2009; Huo and Benson 2015; Vogler et al. 2016a; Watanabe et al. 2017). Furthermore, using transparent fracture replicas and dyed fluids enables the qualitative description of fracture flow during loading (Develi and Babadagli 2015; Babadagli et al. 2015). However, applying such replicas can adulterate actual mechanical fracture properties and also neglects potential fracture-matrix

interactions. Fully coupled THCM experiments are useful to determine the coupling of mechanical closure and dissolution-precipitation processes (Moore et al. 1983, 1994, Morrow et al. 1984, 2001; Polak et al. 2003; Hilgers and Tenthorey 2004; Yasuhara et al. 2006; Ishibashi et al. 2013; Faoro et al. 2015), however are typically time-consuming. Although laboratory experiments are suitable to reveal realistic data, they are often expensive or are limited to certain fracture sizes.

Computational fluid dynamics (CFD) provide an alternative to overcome some of these experimental shortcomings. Generally, CFD codes solving the Navier-Stokes equation (NSE) or consistent Lattice-Boltzmann methods (LBM) are the physically most "exact" methods (Oron and Berkowitz 1998; Brush and Thomson 2003; Cardenas et al. 2007; Landry and Karpyn 2012). NSE and LBM methods also capture fast, non-laminar flow regimes and related local effects such as eddy formation, which are not uncommon in rock fractures (Kohl and Hopkirk 1995; Qian et al. 2007, 2011; Cardenas et al. 2007; Zou et al. 2015). Besides pure fluid flow simulations, there are also coupled THC(B) approaches focusing dissolution, precipitation or biofilm (B) dynamics on the pore-scale (Yoon et al. 2012; Steefel et al. 2013; Ankit et al. 2015a; Wendler et al. 2015). However, 3D approaches often require high computation times due to the complex fracture morphologies. A further CFD approach is the common local cubic law (LCL), which is also known as the lubrication or Reynolds equation. The LCL represents a simplified form of the NSE, where 3D aperture geometries are considered as a 2.5D distribution of local parallel plates along the fracture plane. However, the classical LCL is only applicable to laminar flow problems (Oron and Berkowitz 1998; Brush and Thomson 2003; Zimmerman and Yeo 2013) and often overestimates fracture flow (Nicholl et al. 1999; Konzuk and Kueper 2004; Wang et al. 2015). It is worth noting that Wang et al. (2015) meanwhile presented a modified LCL approach, which also accounts for tortuosity and roughness effects. The big advantages of the LCL are the fast computation times and the potential coupling with many mechanical or chemical fracture alteration codes (e.g. Crandall et al. 2014; Lang et al. 2015, 2016; Li et al. 2015; Pyrak-Nolte and Nolte 2016). Couplings of potential THCM simulation based on the LCL are summarized by Bond et al. (2017) focusing on a THCM experiment on a quartzite fracture (Yasuhara et al. 2006). These approaches reveal plausible results, however rely on some "calibration" factors (Bond et al. 2017), which indicates that further studies and more sophisticated approaches are necessary.

Up to now, there is no universal approach, which can be applied to the full spectrum of (often coupled) thermal, hydraulic, chemical and mechanical fracture processes. More sophisticated experimental or numerical approaches often are too time-consuming or elaborate for practical purposes. Instead, approaches are required, which are easy to apply and only rely on few input data that can be obtained from ordinary measurement methods.

Finding appropriate approaches not only is valuable for geothermal energy production, but also is significant for other geoscientific disciplines such as hydrocarbon extraction (e.g. oil, gas, coalbed

methane), nuclear waste disposal, tunneling, underground fluid storages (e.g. carbon sequestration or hydrogen storage), excavation and slope evaluation (e.g. tunneling or landslides) or water supply and contaminant hydrogeology (National Research Council 1996).

1.5 Objectives

The objective of this thesis is to find efficient and easy-to-apply methods for fracture studies, which can be used to find input parameters for further analytical or numerical (DFN) models. Additionally, another focus of the fracture studies is to get fundamental insights into mechanical and chemical fracture alteration processes and how these processes can affect fracture flow, which is the basis to understand their complex thermal-hydraulic-chemical-mechanical (THCM) coupling under reservoir conditions. Consequently, this thesis comprises three separate numerical approaches, which address the following aims:

(1) In a first step, it is aimed to validate a novel, free and efficient Fast Fourier Transform (FFT)-based web application for a circular granodiorite fracture. In this context, the question, which contact mechanisms (elastic, elastic-plastic or perfectly plastic) govern the normal closure of the considered fracture, is addressed

(2) A further aim is the proposal of a practical approach to combine fluid flow simulations and medical X-ray computed tomography (CT) measurements, which are applied to reproduce fracture geometries under experimental loading/unloading conditions.

(3) The last part of this thesis aims to examine how different grades of sealing and sealing structures affect fracture permeability. A numerical study based on phase-field models of hydrothermally induced quartz growth aims to answer the question whether hydraulic properties of sealing fractures can be expressed by more simplified analytical expressions.

1.6 Structure of the thesis

The presented cumulative thesis consists of three individual fracture studies (Chapter 2, 3 and 4), which are non-chronologically enclosed. The synthesis in Chapter 5 summarizes and establishes a connection between the results and findings of the presented studies. All studies were submitted to peer-reviewed (ISI-listed) journals, whereas two of them are already published and one is submitted.

Chapter 2 contains the third study, *"Numerical simulations and validation of contact mechanics in a granodiorite fracture"*. This study contains the revised manuscript, which is resubmitted to *Rock Mechanics and Rock Engineering* and discusses the validation of physically exact contact models to simulate normal closure of a granodiorite fracture under consideration of elastic and elastic-plastic contact deformation. In this context, a novel, free and efficient web application is introduced into geoscientific research, which also considers fracture geometries derived by high-resolution scans of circular surfaces. Simulations results are also compared to an alternative contact model, which is often used for analytical treatment. Furthermore, the relative hardness, an essential input parameter for the elastic-plastic contact model, is reexamined for granitic rocks.

Chapter 3 presents the first study *"Simulating stress-dependent fluid flow in a fractured core sample using real-time X-ray CT data"*, which was published in *Solid Earth*. This study proposes a practical approach based on real-time X-ray computed tomography (CT) data to reproduce stress-dependent single phase fluid flow in a fractured sandstone sample with low matrix permeability. The simulation approach comprises the aperture calibration based on a modification of the simplified Missing Attenuation approach and the application of a Navier-Stokes-Brinkman solver to simulate fluid flow though the fractured core sample. The flow simulations are validated for a flow-through experiment under loading/unloading conditions, which is conducted simultaneously to the CT scans.

Chapter 4 contains the second study *"Fracture flow due to hydrothermally induced quartz growth"*, which was published in *Advances in Water Resources*. This study examines how different grades of sealing affect fracture permeability by sequentially coupling phase-field models of hydrothermally induced three-dimensional quartz growth and Navier-Stokes simulations to model geometry-related fluid flow in rock fractures. Fluid flow simulations are performed for two types of quartz crystals (compact and elongate), which can precipitate in rock fractures. Resulting flow patterns are discussed with regards to their global and local influence on fracture flow and how the latter depends on the underlying quartz geometries.

Finally, Chapter 5 summarizes the major results of the three studies and evaluates the findings in terms of their importance for future fracture research and applications in fractured reservoir modelling. In addition, pending research questions and proposals based on this thesis are compiled.

Chapter 2

Numerical simulations and validation of contact mechanics in a granodiorite fracture

Reproduced from: Kling T, Vogler D, Pastewka L, Amann F, Blum P: Numerical simulations and validation of contact mechanics in a granodiorite fracture. Rock Mechanics and Rock Engineering [under review].

Abstract

Numerous rock engineering applications require a reliable estimation of fracture permeabilities to predict fluid flow and transport processes. Since measurements of fracture properties at great depth are extremely elaborate, representative fracture geometries typically are obtained from outcrops or core drillings. Thus, physically valid numerical approaches are required to compute the actual fracture geometries under *in situ* stress conditions. Hence, the objective of this study is the validation of a Fast Fourier Transform (FFT)-based numerical approach for a circular granodiorite fracture considering stress-dependent normal closure. The numerical approach employs both purely elastic and elastic-plastic contact deformation models, which are based on high resolution fracture scans and representative mechanical properties, which were measured in laboratory experiments. The numerical approaches are validated by comparing the simulated results with uniaxial laboratory tests. The normal stresses applied in the axial direction of the cylindrical specimen vary between 0.25 and 10 MPa. The simulations indicate the best performance for the elastic-plastic model, which fits well with experimentally derived normal closure data (root-mean-squared error = 9 μm). The validity of the elastic-plastic model is emphasized by a more realistic reproduction of aperture distributions, local stresses and contact areas along the fracture. Although there are differences in simulated closure for the elastic and elastic-plastic models, only slight differences in the resulting aperture distributions are observed. In contrast to alternative interpenetration models or analytical models such as the Barton-Bandis models and the "exponential repulsion model", the numerical simulations reproduce heterogeneous local closure as well as low contact areas (< 2 %) even at high normal stresses (10 MPa), which coincides with findings of former experimental studies. Additionally, a relative hardness value of 0.14 for granitic rocks, which defines the general resistance to non-elastic deformation of the contacts, is introduced and successfully applied for the elastic-plastic model.

2.1 Introduction

For many rock engineering issues such as geothermal or hydrocarbon reservoir engineering or nuclear waste disposal, the presence of fractures are a crucial factor determining the profitability and safety of the project (Blum et al. 2009). Unfortunately, measurements of fracture surfaces or aperture fields are taken from core drillings or outcrop analogues under zero-stress conditions so that these fractures significantly differ from their *in situ* reservoir conditions. With increasing depth, rock fractures typically are affected by increasing effective stresses and the crustal stress fields (Brace and Kohlstedt 1980; Heidbach et al. 2010), which alter the fractures under high compressive stresses, compared to their surface analogues. Since rock fractures basically consist of two opposing, rough surfaces with deformable asperities, increasing effective stresses are associated with a certain fracture closure, which in turn affects the fracture properties such as permeability or stiffness (e.g. Goodman 1976; Pyrak-Nolte and Morris 2000; Blum et al. 2005; Kling et al. 2016; Vogler et al. 2016a).

Several studies established empirical and theoretical relationships between stress and normal closure (e.g. Goodman 1976; Bandis et al. 1983; Barton et al. 1985; Evans et al. 1992; Ohnishi et al. 1996; Rutqvist and Tsang 2003; Blum et al. 2005; Huo and Benson 2015). Indeed, these models are convenient and fast approaches to approximate the fracture aperture, normal closure or permeability at the relevant effective normal stress level. However, they entail uncertainties due to several simplifications such as fitting variables or fracture-specific properties, which have to be determined in experiments. As a consequence, the most common Goodman (Goodman 1976) or Barton-Bandis (BB) models (Bandis et al. 1983; Barton et al. 1985) were found to deviate significantly from experimental data and to be insufficient for predicting *in situ* conditions (Jing et al. 1995; Ohnishi et al. 1996). This can partially be attributed to the simplified representations of fracture morphology by these models, as the response of a fracture to stress is a 3D problem relying on unique fracture morphologies (Hopkins 2000).

3D measurement techniques such as laser scanning, photogrammetry, white light interferometry (WLI) or atomic force microscopy (AFM) made rapid progress in the last years and found their way into geoscientific fracture analyses ranging from the nanometer to meter scales (e.g. Candela et al. 2009; Yasuhara et al. 2011; Seiedi et al. 2011; Candela et al. 2012; Tatone and Grasselli 2012b; Vogler et al. 2016a; Fischer and Luttge 2017). Furthermore, several methods, which facilitate the morphological reproduction of 3D fracture surfaces or aperture fields based on statistical information, have been introduced (e.g. Garcia and Stoll 1984; Nolte and Pyrak-Nolte 1991; Méheust and Schmittbuhl 2001; Ogilvie et al. 2003; Candela et al. 2009; Co and Horne 2015).

Contact models in rock fracture research most often are based on the Hertzian/Greenwood-Williams (HGW) contact theories (e.g. Greenwood and Williamson 1966; Brown and Scholz 1985; Yoshioka 1994a, b; Lespinasse and Sausse 2000), on the Hopkins method (e.g. Hopkins et al. 1987; Hopkins 2000; Pyrak-Nolte and Morris 2000; Gentier et al. 2013; Pyrak-Nolte and Nolte 2016; Wang and Cardenas 2016), straightforward finite element (FE) solutions (e.g. Walsh et al. 2008; Lavrov 2017) or on the interpenetration approach (e.g. Brown 1987; Walsh et al. 1997; Power and Durham 1997; Oron and Berkowitz 1998; van Genabeek and Rothman 1999; Kim et al. 2003; Watanabe et al. 2005, 2008; Matsuki et al. 2006; Nemoto et al. 2009; Liu et al. 2013; Souley et al. 2015). The latter represents the least physical approach assuming unconditionally deformable (or overlapping) asperities that are merged until the resulting aperture field reaches a predefined threshold such as experimentally determined closure or (relative) contact areas. However, this approach is fast, easy to implement and can yield reasonable results (e.g. Kim et al. 2003; Walsh et al. 2008). Physically more valid contact mechanics are considered by the HGW model. However, similar to the interpenetration approach, the HGW model neglects interactions between neighbouring asperities, which can have a significant effect on the fracture stiffness and resulting local apertures (Ciavarella et al. 2008; Li et al. 2015). Indeed, such interactions are considered in the Hopkins model, however this model presumes a geometrical trichotomy into three elastically deformable components, which are represented by the two fracture surfaces and cylindrically shaped asperities (Li et al. 2015; Wang and Cardenas 2016; Lavrov 2017).

In recent studies, boundary element methods based on the elastic half-space approximation (Kalker and Randen 1972), often solved using a Fast Fourier Transform (FFT)-based convolution, found its way into rock fracture analyses (Table 2.1). The FFT-based convolution method is based on the pioneering work of Stanley and Kato (1997), which is considered as the “exact” solution for purely elastic surfaces of homogeneous materials, since it maintains original fracture morphologies and accounts for interactions between local asperities (Jackson and Green 2011). Furthermore, this method has been extended to capture elastic-plastic deformation (e.g. Almqvist et al. 2007; Li et al. 2015; Wu and Sharma 2017). An advantage of the FFT-based method (also depending on the solution algorithm) is the high computational efficiency (Wu and Sharma 2017) as compared to direct or multilevel summation techniques (Polonsky and Keer 1999).

Table 2.1: Contact mechanical simulations based on the Fast Fourier Transform (FFT)-based convolution of Stanley and Kato (1997) for rock fractures. Applied mechanical properties are the static Young's modulus *E*, the Poisson ratio ν and the indentation hardness *H*.

Fracture surface (Mesh grid)	Surface generation (Dimension)	Contact deformation	Mechanical properties	Model purpose	Validation/ Verification	Reference
Artificial granite fracture (2048 × 2048)	Profilometry (12.8 × 12.8 mm²)	Elastic	N/A	Statistical study on contact stresses	Not done	Hansen et al. (2000)
Artifical novaculite fracture (1779 × 918)	Laser-scan (50.0 × 89.5 mm²)	Elastic, Elastic-plastic	*E* = 70 GPa (Quartzite); ν = 0.2 (Quartzite) *H* = 10 GPa (Quartz)	Simulation of fracture closure; Implications on pressure dissolution	Back-calculation of flow experiments	Li et al. (2015)
Synthetic quartzite fracture (256 × 256, 1024 × 1024)	Fractal surface (1.0 × 1.0 cm²)	Elastic	*E* = 95.6 GPa (Quartz) ν = 0.08 (Quartz)	Simulation of pressure dissolution	Verified by other pressure dissolution models	Lang et al. (2015)
Synthetic rock fracture (1024 × 1024)	Fractal surface (0.5 × 0.5 m²)	Elastic	*E* = 20 - 65 GPa ν = 0.15	Stiffness evolution due to pressure dissolution	Simulations are fitted to experimental results	Lang et al. (2016)
Synthetic (homo- and heterogeneous) shale fracture (128 × 128)	Gaussian surface (1.3 × 1.3 mm²)	Elastic, Elastic-plastic	*E*=20-60 GPa (Shale) ν = 0.25 (Shale) *H* = 0.6-0.9 GPa (Shale)	Stress-dependent fracture flow	Fracture flow experiments	Wu and Sharma (2017)

Until now, FFT-based convolution methods are only applied in few rock mechanical studies and only by considering rectangular fractures (Table 2.1), which can be ascribed to the intrinsically periodic nature of the underlying FFT. The studies in Table 2.1 indicate several advantages of this method such as determining contact stresses and areas, aperture distributions and the coupling with flow or reactive transport simulations. However, none of these studies performs a validation of their computational methods by using explicit, experimentally derived normal closure data. Furthermore, except for the pure numerical study of Hansen et al. (2000), all these studies consider synthetic fracture surfaces or/and homogeneous rocks such as quartzite or shale. However, when considering geothermal energy production (e.g. enhanced geothermal systems, EGS) or nuclear waste disposal, where site-specific fractures are typically obtained from core drillings during the prospection and exploration phase, particularly heterogeneous rocks such as granites or granodiorites play an important role. In order to reproduce representative down-hole fracture geometries, physically valid contact models are required, which are valid for heterogeneous rocks and which are also applicable for aperiodic (circular) fracture surfaces. Hence, there still are three major questions concerning the FFT-based convolution method: (1) How accurate does the method reproduce actual stress-dependent normal closure based on fracture surface scans of a (circular) core sample? (2) Is the underlying assumption of a homogeneous material also applicable for heterogeneous granitic rocks? (3) And what is the actual advantage of the proposed approach in contrast to other common models such as the interpenetration or the Barton-Bandis model? Furthermore there is still the question if an elastic contact model is sufficient to simulate fracture closure as stated by Wang and Cardenas (2016) or not?

2.2 Material and experiments

2.2.1 Experimental setup

The rock fracture (Specimen B) and experimental data used for the numerical simulations are adopted from a previous fracture study (Vogler 2016; Vogler et al. 2016b, 2018). The artificial tensile fracture is generated perpendicular to the axes of a granodiorite core-samples (122 mm in diameter) obtained from the Grimsel Test Site (GTS) located in the Swiss Alps. The rock sample mainly consists of quartz, alkali feldspar, plagioclase and phyllosilicates (especially biotite, Fig. 2.1) with grain sizes between 3 and 8 mm.

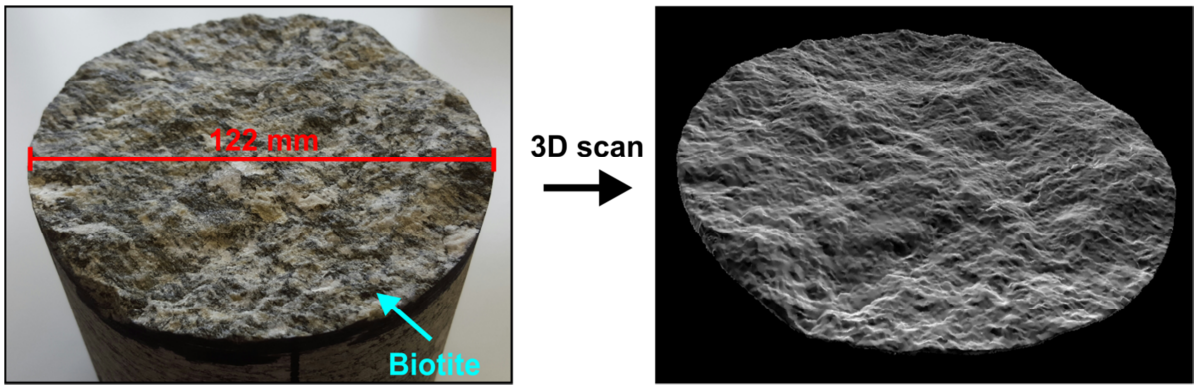

Fig. 2.1: Photo (left) and rendered 3D photogrammetry scan (right) of the fracture bottom. Darker minerals along the fracture photo are mostly biotite.

Normal closure rates are taken from a dry uniaxial compression test (Vogler et al. 2018). Experimentally determined closure data from sensors are corrected for the theoretical elastic deformation of the bulk material to obtain fracture closure data with varying applied normal loads. The theoretical deformation of the specimen is estimated with rock mass parameters obtained from separate compression tests on intact rock specimens from the same borehole. The corrected experimental data represents the stress-dependent fracture closure. The closure experiments start at a normal stress σ_n of 0.25 MPa, which incrementally increases up to 10 MPa. The pre-loading of 0.25 MPa of the fracture is required to avoid that initial seating and mating processes affect the normal closure measurements. The corrected normal closure is assumed to represent the change in mean mechanical aperture between 0.25 MPa (meaning that normal closure = 0.0 mm) and subsequent loading increments until reaching the maximum stress of 10 MPa (Rutqvist and Stephansson 2003).

2.2.2 Experimental setup

The fracture surfaces are scanned before the closure experiment using a high-resolution photogrammetric ATOS Core 3D scanner (GOM GmbH, Germany), with a calibrated measure accuracy between 9 and 27 µm. This accuracy can vary for more complex (rough and/or heterogeneous) surfaces. Due to the mineralogical heterogeneity of the rock sample (Fig. 2.1), which could cause irregular backscattering of the light, the surfaces were coated with a non-reflecting, white thin-film of a few microns before scanning in order to avoid reflectivity effects (Vogler et al. 2017, 2018). For the simulations presented in this study, the point clouds of the photogrammetry scans (Fig. 2.1) are matched with GOM Inspect software, which results in some initial overlapping contacts (i.e. normally a minimum of three contact points, which are used to consider the zero-stress surfaces as "balanced") due to the underlying matching algorithm. Afterwards, the matched stl-files of the surfaces are transferred to a Cartesian coordinate system by using MATLAB resulting in a grid resolution of 0.1 × 0.1 mm² in the x,y-plane. Finally, the aperture field is calculated by determining the difference between the local asperity heights of the upper and lower surfaces. This initial aperture field is then simplified to a composite fracture surface (Fig. 2.2a), where opposite surfaces only touch at a single point as also assumed by Li et al. (2015) and Lang et al. (2016) revealing the typical lognormal aperture distribution with a mean mechanical aperture a_m of 711 µm (Fig. 2.2b).

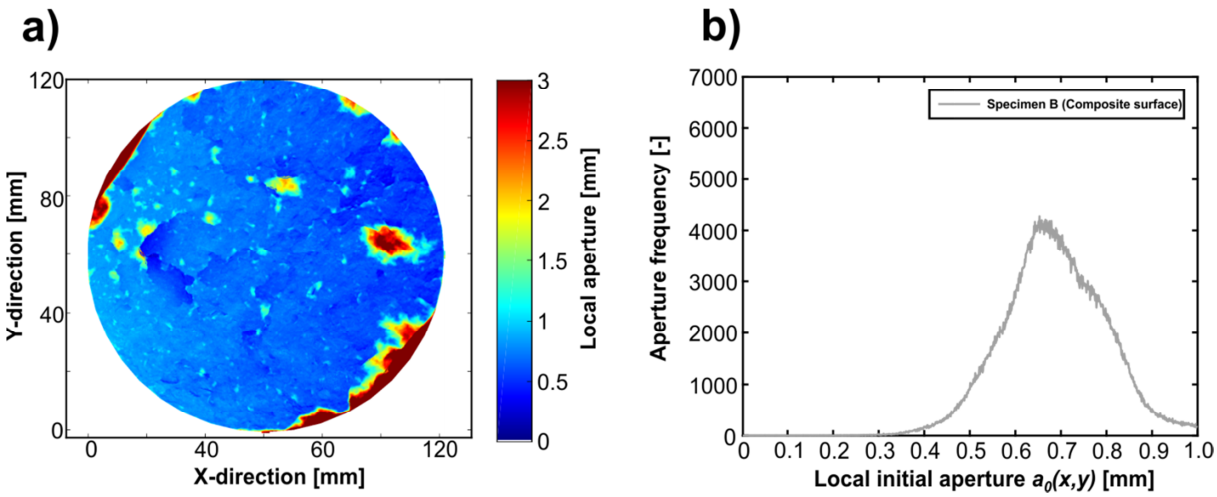

Fig. 2.2: Spatial representation (a) and histogram (b) of the initial aperture distributions of fracture (Specimen B) with the mean mechanical aperture a_m and its standard deviation s_a. Apertures >1 mm are excluded to ease comparison.

2.2.3 Material properties

The numerical contact models only require the following three material properties (Fig. 2.3): (1) static Young's Modulus *E*, (2) Poisson ratio ν and (only for the elastic-plastic model) and (3) indentations hardness *H*.

The elastic material properties of the intact granodiorite are estimated from uniaxial compression tests, which yield a static Young's modulus E between 10-12 GPa (Vogler et al. 2018) Since there are no explicit measurements of the Poisson ratio, a Poisson ratio of 0.03 is assumed in this study, which is similar to the value determined by Keusen et al. (1989) for other Grimsel Granodiorite samples. However, it is found in previous contact mechanical studies that deviations from the actual Poisson ratio have only small effects on the simulations (Hyun et al. 2004; Pei et al. 2005). Although the sample-specific E is determined through uniaxial compression tests on the Grimsel granodiorite, values from the literature are collected to define a reasonable range of E for the sensitivity analysis (Table 2.2).

Table 2.2: Potential mechanical properties of the rock fracture obtained from literature.

Material	**Young's modulus** ***E*** **[GPa]**	**Poisson ratio** **ν [-]**	**Indentation hardness** ***H*** **[GPa]**	**Hardness test / estimation**	**Relative hardness** ***H/E****	**References**
Quartz	95.6[a]	0.08[a]				a) Pabst and Gregorova (2013)
			10.0[b]	Vickers	0.21	b) Evans (1984)
			6.5-9.0[c]	Knoop	0.14-0.18	c) Winchell (1945)
			8.6[d]	Knoop	0.18	d) Zichella et al. (2017)
Westerley Granite	34	0.21	4.9	Vickers	0.30	Swain and Lawn (1976)
Grimsel Granodiorite (Literature)	47.3	0.33	2.6		0.10	Keusen et al. (1989); H estimation is based on UCS=116.9 MPa and Eq. 2.1
Grimsel Granodiorite (Specimen B)	10-12					Vogler et al. (2018)

Material properties are also taken for quartz as the theoretical uppermost material boundary (in regards to stiffness) by assuming that the asperities are only in contact along quartz grains representing the dominant rock-forming mineral (30 %) besides feldspars (55 %) of the granodiorite (Keusen et al. 1989; Wehrens et al. 2017). Furthermore, the extensively investigated Westerley granite and a granodiorite sample from another testing location of the GTS, whose mechanical properties lie in between the experimental and quartz data are taken into consideration.

Indentation hardness values, which typically describe the resistance against non-elastic deformation (Brown and Scholz 1986), are obtained from literature data. There are several hardness studies about quartz, which illustrate how relative hardness can vary due to the choice of the indentation hardness H (Table 2.2). Only for the Westerley granite directly related, possible input parameters (E, ν, H, Table 2.2) were found in literature (Swain and Lawn 1976), where Vickers indenter tests reveal an indentation hardness of H = 4.9 GPa. Similar high indentation hardness values for granitic rocks are also found for common monumental stones, where H typically ranges between 4.8 and 8.1 GPa (Fig. 2.4; Amaral et al. 2000; Zichella et al. 2017). Significantly lower hardness values between approximately 1.8 and 2.6 GPa are found for granites from the "Lucky Friday" mine, which is located within the Coeur d'Alene mining district (Jung et al. 1994). This variability of potential rock hardness values is caused by several factors such as grain size, mineral anisotropy, mineral impurities, porosity, measurement method (e.g. after Vickers, Knoop or Berkowich) and, in particular for granodiorites, on the rock forming minerals (e.g. Yoshioka 1994a, b; Amaral et al. 2000; Zichella et al. 2017), which exacerbates the selection of a representative hardness value.

However, by using the aforementioned full "Lucky Friday" data set, Momber (2015) recently derived an empirical equation that linearly correlates the indentation hardness H and the uniaxial compressive strength UCS (R^2 = 0.97) and can be written as follows

$$H = 20.2UCS + 277MPa \tag{2.1}$$

Since the indentation hardness H was not determined in this study, the correlation between H und UCS provides a reasonable means for estimating a representative hardness value for the granodiorite.

2.3. Contact mechanics

2.3.1 Material properties

The basic idea behind the Fast Fourier Transform (FFT)-based convolution method was introduced by Stanley and Kato (1997), who focused on elastic contact mechanics. Plasticity was subsequently introduced, for example by Almqvist et al. (2007). The FFT-based approach constitutes a boundary element method (BEM) that allows faster computation of the contact models than for example the solution of the full elastic problem in the finite element method (Hyun et al. 2004; Pei et al. 2005) or other BEMs such as multi-level summation (Polonsky and Keer 1999). In this study, the FFT-based convolution method is incorporated into a novel web application, which is developed concurrent to this study by Pastewka (http://contact.engineering/) and accounts for elastic and for elastic-plastic deformation of contacting fracture asperities. Accordingly, resulting simulation results afterwards are

referred to as the numerical simulations, which can be subdivided into the elastic (EL) or elastic-plastic (EP) model. The applied workflow of the elastic and elastic-plastic models is summarized in Fig. 2.3 and the theory is elucidated in the following subchapters. Furthermore, Fig. 2.3 depicts an alternative interpenetration model, which is explained in the last subchapter.

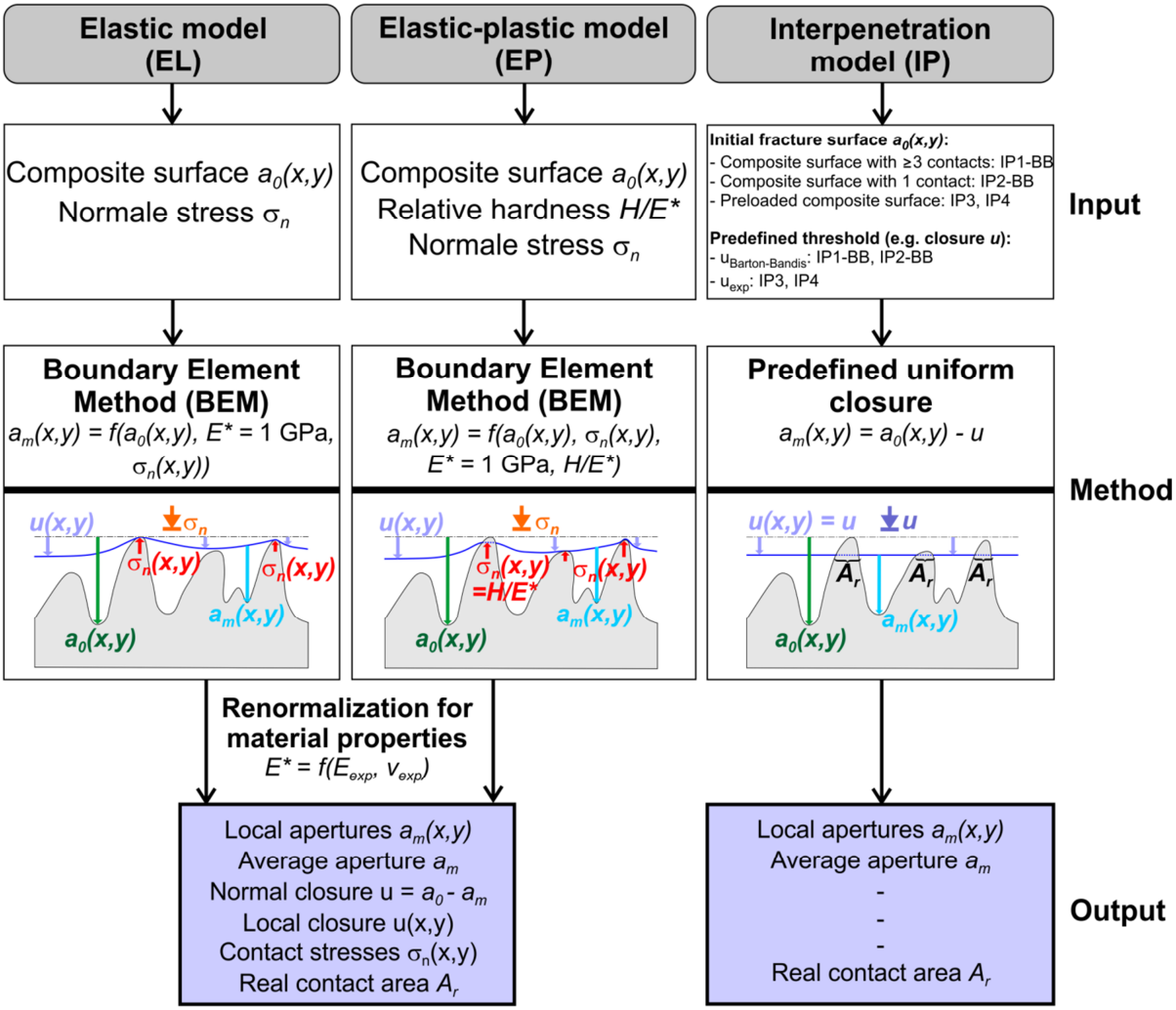

Fig. 2.3: Workflow of the adaption process for the Fast Fourier Transform (FFT)-based elastic (EL) and elastic-plastic (EP) models and the interpenetration models (IP) including the required data input, the schematic contact models and the final data output. Four approaches for the IP models are applied differing by their initial aperture field $a_0(x,y)$ and closure data (IP1-IP4). Closure data derived by the Barton-Bandis (BB) model facilitate the choice of $a_0(x,y)$ at $\sigma_n = 0$ MPa. Experimental closure data require the potential initial composite fracture surface at $\sigma_n = 0.25$ MPa.

2.3.1.1 Elastic model

The elastic model (EL) simulates the frictionless and dry contact of two surfaces, where the two surfaces can be equivalently represented by a rigid rough composite surface, which is in contact with a deformable, planar half-space (Johnson 1985). Although, the fracture surfaces are mineralogically heterogeneous, the deformable half-space is assumed to be homogeneous, but its deformation response is governed by representative bulk properties of the granodiorite.

Consequently, the elastic (EL) contact deformation model solves the equations of linear elasticity for an infinite elastic half-space during contact loading (Love 1929; Johnson 1985). The condition at contact is that of an impenetrable wall, whose hardness is assumed to be infinite to prevent non-elastic contact deformation. The elastic properties of the half-space are governed by E^*, which describes the effective Young's Modulus (often also called contact or reduced modulus) of the two surface materials and is defined by the reciprocal of

$$\frac{1}{E^*} = \frac{1-\nu_1^2}{E_1} + \frac{1-\nu_2^2}{E_2} = \frac{2(1-\nu^2)}{E} \tag{2.2}$$

where $E_1 = E_2 = E$ is the Young's Modulus and $\nu_1 = \nu_2 = \nu$ is the Poisson of the matrix material, which is supposed to be equal for both fracture surfaces (Greenwood and Williamson 1966; Johnson 1985).

In this study, only displacements normal to the surface are considered. Any cross-coupling between normal and in-plane displacements is ignored. This approach is exact for Poisson numbers of $\nu = 0.5$, where normal and in-plane displacements decouple, but errors for other ν are typically small. Furthermore, the local normal closure $u(x,y)$ is linearly related to the local surface stresses $\sigma_n(x,y)$. This linear relation can be generally expressed through a Green's function

$$u(x,y) = \int G(x-x', y-y')\sigma_n(x',y')dx'dy' \tag{2.3}$$

Many different solution procedures are proposed for Eq. 2.3 such as direct summation (Kalker and Randen 1972) and multilevel summation (Polonsky and Keer 1999). Our FFT-based solution makes use of the fact that the convolution with the Green's function G in Eq. 2.3 becomes a product in reciprocal (Fourier) space. Equation 2.3 then reads

$$\tilde{u}(q_x, q_y) = \tilde{G}(q_x, q_y)\tilde{\sigma}_n(q_x, q_y) \tag{2.4}$$

where the quantities with a tilde are the Fourier transform of the respective quantities in Eq. 2.3. In Eq. 2.4, q_x and q_y are the wavevectors in reciprocal space, i.e. $q_x = 2\pi/\lambda_x$ where λ_x is the respective length of

the corresponding wave. Since we operate on a discrete set with $N_x \times N_y$ data points, our Fourier transform becomes the discrete Fourier transform, which we compute with an FFT algorithm. In the discrete Fourier transform, both real and reciprocal space are sampled at discrete points $x = iL_x/N_x$ and $q_x = 2\pi k/L_x$, where L_x is the linear size of the fracture and i as well as k run from 0 to $N_x - 1$, Calculating Eq. 2.4 is then a simple multiplication so that all the complexity of solving the non-local, long ranged elastic interaction is absorbed in the FFT. This approach is extremely fast because highly efficient, optimized "fast" Fourier transform implementations exist.

The Green's function $G(x,y)$ or $\tilde{G}(q_x,q_y)$ depends on the problem to be solved. We here employ a regularized version of the classical Boussinesq-Cerutti expression (Love 1929; Johnson 1985) that is appropriate for half-spaces unbounded (nonperiodic) in the plane of contact. The Boussinesq-Cerutti solution is the solution for point loading that provides a divergent closure $u(x,y)$ at the point of loading. We regularize this divergence by assuming a constant load over a rectangular area (Kalker and Randen 1972; Johnson 1985) corresponding with the area of a mesh grid cell in the topography map that describes the aperture of the fracture. Equivalent Green's functions were also derived for periodic systems (e.g. Amba-rao 1969; Persson 2001; Barbot and Fialko 2010) or atomic lattices (Campañá and Müser 2006; Pastewka et al. 2012). The FFT is intrinsically periodic, but can be used to compute the response of a nonperiodic system by employing a padding region (Hockney 1970; Pastewka and Robbins 2016). Essentially, the padding region decouples the periodic images by introducing an auxiliary spatial region that experiences zero pressure σ_n. The size of this region must be at least equal to the linear dimension of the active computational domain, such that a surface load in the active region does not influence its own periodic image.

The constrained conjugate gradients algorithm of Polonsky and Keer (1999) is used to solve for the mixed boundary problem of having no penetration inside the contacting area as well as vanishing surface pressure σ_n outside. Contacts are represented by those grid points (apertures) touching the half-space (Fig. 2.3) so that the summation of the scaled grid points reveals the (real) contact area A_r, while non-contacting grid points are local apertures $a_m(x,y)$.

2.3.1.2 Elastic-plastic model

In general, solving the elastic-plastic (EP) contact problem is equivalent to the elastic (EL) approach, however requires an additional parameter input. Whether the material's response to stress is elastic or plastic most widely can be assigned to the indentation hardness H of the material. Based on the previously described code for purely elastic contact deformation, the plastic problem can be implemented by introducing a constraint of the maximum local stress $\sigma_n(x,y)$ in the algorithm of Polonsky and Keer (1999) so that $\sigma_n(x,y)$ cannot exceed H. Hence contacts, which are subjected to

plastic deformation, cannot exceed the hardness of the (softer) material (Almqvist et al. 2007). Non-elastic deformation occurs as soon as the normalized local contact stress exceeds H. Since stresses in the elastic calculation scale with E^*, the only (dimensionless) material parameter entering the elasto-plastic calculations is H/E^*. In the elastic-plastic model, plastic (or non-elastic) contact deformation is simplified by an interpenetration of the deformable half-space (Fig. 2.3), meaning that resulting local apertures ≤ 0 mm are considered as contacts. Strictly speaking, the concept of perfectly plastic deformation at contacts is not physically valid for most technically relevant rock fractures in the upper Earth's crust. However, since no considerable pronounced brittle deformation or even fracturing was found under the experimentally applied range of normal stresses, the simplified assumption of an elastic-plastic model can be assumed to be representative for the studied experiment.

2.3.2 Model comparison

The often applied, but physically simplified interpenetration (IP) model approach is used to emphasize the advantages of the numerical simulations especially in terms of morphological deviations such as aperture distribution or contact areas. In the IP model, local apertures of an initial aperture field are homogeneously reduced until reaching a specific threshold (Fig. 2.3). Apertures, which become ≤ 0 mm are generalized to a local contact area by assuming that the overlap of asperities reproduce both elastic and non-elastic deformation (Watanabe et al. 2008). There are different thresholds, when applying the IP model, represented by experimentally or analytically derived normal closure data (e.g. Walsh et al. 2008; Li et al. 2015; Souley et al. 2015), by contact area estimation methods (Nemoto et al. 2009) or by coupling fluid flow simulations in order to reproduce flow through experiments (Watanabe et al. 2008). In this study, the IP models are realised by applying both experimentally and analytically derived normal closure data.

One common analytical approach to estimate normal closure is based on the empirical hyperbolic stress-displacement relationship proposed by Goodman (1976). This assumption provides the basis for the Barton-Bandis' (BB) empirical model (Bandis et al. 1983; Barton et al. 1985), where the fitting variables of Goodman's model are replaced by the initial fracture normal stiffness ($k_{n,0}$) and the maximum possible normal closure ($u_{n,max}$) so that the stress-dependent normal closure can be written as

$$u = \frac{\sigma_n}{\left(k_{n,0} + \frac{\sigma_n}{u_{n,max}}\right)} \tag{2.5}$$

A similar approach is also used by Li et al. (2015) to verify their numerical models, however without having explicit data of $k_{n,0}$ or $u_{n,max}$. The initial normal stiffness ($k_{n,0}$) used in this study is derived from

the first stress increment (0.25 to 0.5 MPa) and is about 5.06 MPa/mm. The maximum possible closure ($u_{n,max}$) is set to 300 µm (Bandis et al. 1983; Matsuki et al. 2008; Li et al. 2015).

Based on the BB model two scenarios are considered: IP1-BB that uses the original, computationally matched surface with at least 3 (overlapping) contacts and, as applied by Li et al. (2015), IP2-BB that uses the resultant single-point-contact aperture field, which is also used for the numerical simulations. Additionally, two scenarios are considered, which are based on initial aperture fields, derived from the elastic (IP3) and elastic-plastic (IP4) models at 0.25 MPa as well as the experimentally derived closure data. IP3 and IP4 are introduced for better comparison of the resulting aperture distributions to discuss the advantages of the numerical simulations. The computations of the interpenetration models are performed by using a purpose-built MATLAB code (Version R2015b).

Furthermore, a second analytical model is employed to fit the experimental data, which is necessary to check the performance of the numerical simulations. This is necessary, since fitting the hyperbolic BB model still reveals significant disagreements with the experimental data. In this study, the alternative model is called the "exponential repulsion model" (ERM). The ERM implies that the contact normal stiffness ($k_n = d\sigma_n/da_m$) is proportional to the normal stress σ_n itself, which was also found experimentally (e.g. Bandis et al. 1983; Swan 1983; Berthoud and Baumberger 1998).

Recent investigations into the elastic contact of rough surfaces yield a simple expression, which has been confirmed numerically and is commensurate with this experimental evidence. Benz et al. (2006) suggest that compressing asperities on rough surfaces leads to an exponential repulsion. The authors present evidence from surface force apparatus experiments and earlier calculations by Hyun et al. (2004). Additionally, Pei et al. (2005) show additional numerical evidence for an exponential relationship between normal stress σ_n and normal closure u. Hence, Persson (2007) derived this relationship by using his scaling theory of contact mechanics. The result is the compact expression (Persson 2007; Yang and Persson 2008)

$$\sigma_n = \beta E^* exp\left(\frac{-a_m}{\gamma h_{rms}}\right) \tag{2.6}$$

comprising the dimensionless variables β and γ (Persson 2007; Pastewka et al. 2013), the effective Young modulus E^*, the areal root-mean-squared roughness h_{rms} and the mean mechanical aperture a_m of the composite fracture surface. Both variables β and γ only depend on the spectral properties of the composite fracture surface (Persson 2007). Numerical and analytical studies indicate that the dimensionless constant γ in Eq. 2.6 can have values between approximately 0.4 and 0.5 (Pei et al. 2005; Persson 2007; Yang and Persson 2008; Campañá et al. 2011; Akarapu et al. 2011; Almqvist et

al. 2011). The root-mean-squared roughness h_{rms} is equivalent to the common S_q roughness parameters and can be derived by

$$h_{rms} = \sqrt{\frac{\sum_{x,y} a_m(x,y)^2}{N_x N_y}} \tag{2.7}$$

where $a_m(x,y)$ represents the local mechanical aperture and $N_{x/y}$ accounts for the number of grid cells of the fracture surface. It should be mentioned that for surface analyses (e.g. for a_m or h_{rms}) the sample edges are excluded to prevent influences of non-representative asperities caused by the fracturing procedure or scanning artefacts.

Finally, the stress-dependent mean aperture can be calculated by rearranging Eq. 2.6 so that

$$a_m(\sigma_n) = -\gamma h_{rms} ln\left(\frac{\sigma_n}{\beta E^*}\right) \tag{2.8}$$

Based on this equation, the respective normal closure in this study can be calculated by the difference of the mean mechanical aperture a_m at *0.25 MPa* and resulting a_m values at higher normal stresses.

2.4 Results and discussion

Numerical simulations are applied by assuming both an elastic and an elastic-plastic constitutive relation. Since possible input parameters for the fracture are not unequivocal, elastic (EL) and elastic-plastic (EP) simulations are performed for different material properties. No general relative hardness for granitic rocks is found in literature so that the first part of this study briefly explains the derivation of a representative hardness value based on Eq. 2.1. Finally, the numerical results are compared to the interpenetration (IP) model scenarios to examine the advantages of EL and EP models.

2.4.1 Model input (relative hardness)

To find a representative relative hardness for granitic rocks, indentation hardness values for 114 granitic samples are derived by using Eq. 2.1 and are related to their respective effective Young's moduli (Fig. 2.4; Swain and Lawn 1976; Keusen et al. 1989; Leith et al. 1991; Tuğrul and Zarif 1999; Katz et al. 2000; Aydin and Basu 2005; Přikryl 2006; Ceryan 2008, 2015; Sousa 2014)). These data also contain weathered granitic rocks, where the chemical alteration results in lower static Young's moduli (E < 20 GPa) similar to the granodiorite sample. In case that no Poisson ratio was available for the single samples, ν was assumed to be 0.25. Using different values of ν (± 0.05) to calculate E^* according to Eq. 2.1 produces negligible deviations (≤ 3 %).

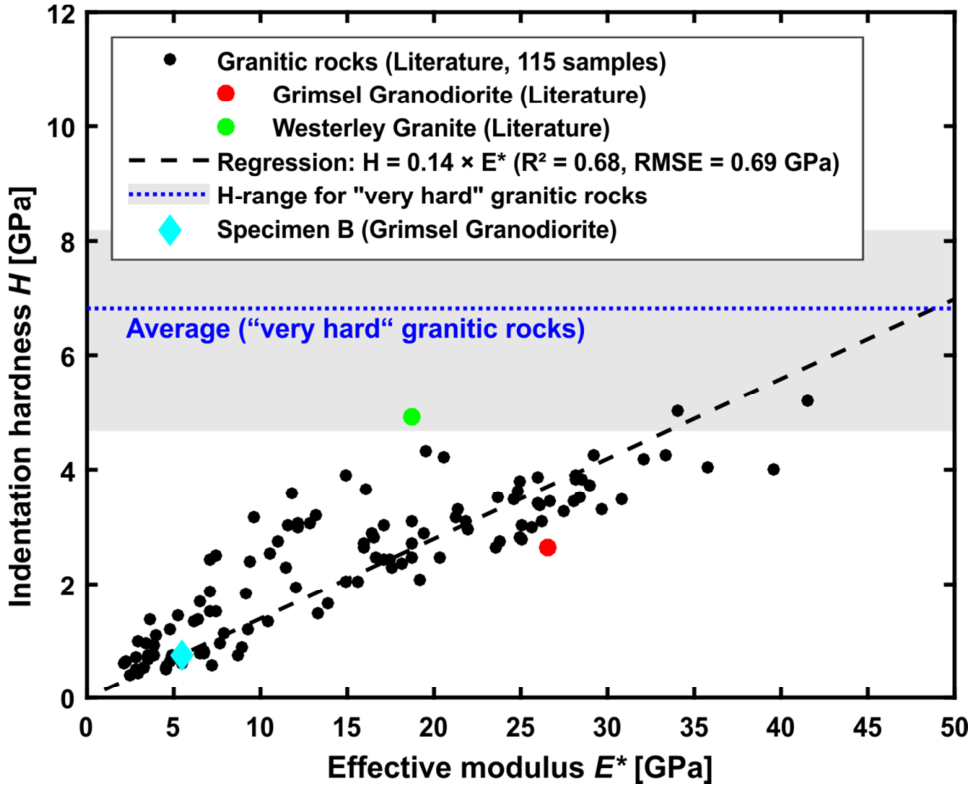

Fig. 2.4: UCS-related indentation hardness (H) changing with the effective Young's modulus E^* based on literature data for 114 granitic rocks. An upper limit for H is represented by the value range derived for 11 "very hard" granitic monumental stones with boundaries representing the averaged 25th and 75th percentiles of the sample scanlines (Amaral et al. 2000; Zichella et al. 2017). Granitic rocks that are also considered in **Table 2.2** are highlighted for comparison.

The data points indicate that the indentation hardness increases with increasing E^*. However, most of the calculated indentation hardness values are lower than those of monumental stones (H < 4.8 GPa). For a first-order approximation of the relative hardness a linear regression crossing the origin is supposed to be sufficient (Fig. 2.4). Accordingly, it can be assumed that granitic rocks as well as our sample should have a relative hardness H/E^* of approximately 0.14, which corresponds to the slope of the regression line (Fig. 2.4).

Although, there are some uncertainties in the derived relative hardness (R^2 = 0.68), H/E^* = 0.14 also matches quite well with $H/E^* \approx$ 0.1 for many crystalline ceramics or glasses (Oliver and Pharr 1992; Tan and Cheetham 2011) and shows good resistance to plastic (or non-elastic) deformation. Even very hard minerals such as corundum reveal a similar relative hardness of $H/E^* \approx$ 0.13 (Oliver and Pharr 1992). Predominantly non-elastic deformation would be facilitated by H/E^* values significantly smaller than 0.1 as found for softer rocks such as shales (Wu and Sharma 2017).

2.4.2 Model results

Three scenarios are simulated within the scope of this study: (a) Elastic contact deformation (Fig. 2.5a) for different Young's moduli (E = 11 to 95 GPa,), (b) elastic-plastic deformation (Fig. 2.5b) for identical relative hardness (H/E^* = 0.14) and different Young's Moduli (E = 11 to 95 GPa,) and (c) elastic-plastic deformation (Fig. 2.7) for identical Young's moduli (E = 11 GPa), however for different relative hardness values (H/E^* = 0.02 to 0.3). All simulated closure values represent the difference between the simulated mean mechanical aperture a_m at 0.25 MPa and the resulting a_m at subsequent loading steps up to 10 MPa.

The three simulation scenarios show that both the elastic (EL) and elastic-plastic (EP) numerical simulations generally reproduces the characteristic non-linear behaviour of the closure curve being typical for rock fracture closure (e.g. Bandis et al. 1983; Barton et al. 1985; Pyrak-Nolte and Morris 2000; Huo and Benson 2015). In order to check the single performances of the simulation scenarios an ideal fitting curve through the experimentally derived closure data is required. For this purpose, the Barton-Bandis (BB) model (Eq. 2.5) is fitted to the experimental curve ($R^2 \approx 1$) by adjusting the initial fracture stiffness ($k_{n,0}$ = 3.33 MPa/mm) and the maximum possible fracture closure ($u_{n,max}$ = 293 µm). While fitted $u_{n,max}$ is similar to the assumed value (293 µm) the $k_{n,0}$ is lower (5.06 MPa/mm) indicating lower stiffness values at normal stresses < 0.25 MPa.

The numerical results for pure elastic deformation (Fig. 2.5a) yields good model performance for lower normal stress (σ_n < 5 MPa), however indicates an overestimation at higher stresses (σ_n > 5 MPa; Fig. 2.5b and Fig. 2.7). Root-mean-squared errors (RMSE) between the simulated curves and the fitted ERM range between 8 µm and 11 µm. The model performance improves with increasing Young's modulus. Thus, the best fit (RMSE = 8 µm) is found for the high Young's modulus of quartz (E = 96 GPa). However, at the highest normal stress (σ_n = 10 MPa) the error (overestimation) between experimental and simulated results is about 8 % for quartz and even 17 % for the experimentally derived Young's modulus.

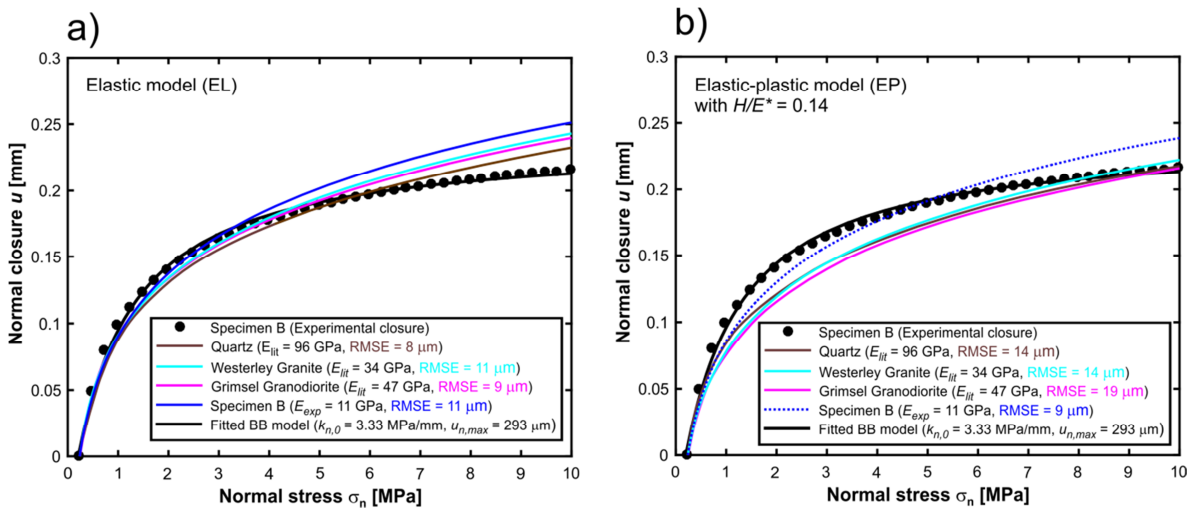

Fig. 2.5: Comparison of experimental and simulated normal closure for (a) the elastic contact models with different Young's-moduli derived from **Table 2.2** and (b) for the elastic-plastic model by applying different Young's moduli and the empirically derived relative hardness H/E^* = 0.14. The model performance is represented by the root-mean-squared error (RMSE) relative to a fitted Barton-Bandis (BB) model with $k_{n,0}$ = 3.33 MPa/mm and $u_{n,max}$ = 293 µm (according to Eq. 2.5).

More pronounced deviations are found for the elastic-plastic (EP) models (RMSE between 9 and 19 µm) by using the relative hardness (H/E^* = 0.14) derived for granitic rocks (Fig. 2.5b). For the EP models, the model with the experimentally derived Young's modulus exhibits the lowest error (RMSE = 9 µm) throughout the tested normal stress range with a maximum error of about 11 % at 10 MPa, which decreases with increasing Young's modulus (e.g. ≤ 1% for E = 96 GPa). Unlike the EL models (Fig. 2.5a), where differences in the normal closure curves can be attributed to the value range of the applied Young's moduli, the results of the EP model suggest different relations. In this context, the EP model (Fig. 2.5b) shows that for Young's moduli ≥ 34 GPa and H/E^* = 0.14, the simulated curves deviate by maximal 7 µm from each other and significantly from the experimental results at lower normal stresses (< 7 MPa). Compared to the EL model, the EP model indicates a significant stiffening for earlier loading stages of the fracture, which can be ascribed to a more pronounced contact formation during pre-loading (where σ_n < 0.25 MPa). The more pronounced, early contact formation is facilitated by the plastic collapse of few initial contacts, which promptly reach the threshold value defined by the relative hardness. While the lower Young's modulus (E = 11 GPa) still facilitates further significant elastic deformation (in combination with local plastic yielding) along existing contacts, even Young's moduli as low as 34 GPa are sufficient to significantly decelerate further closure.

Both, the elastic and elastic-plastic models (Fig. 2.5) show that that the experimentally derived Young's modulus (E = 11 GPa) reveals the closest agreement with experimental closure. Nevertheless,

there still remains the question, which approach is more valid, the elastic (EL) or the elastic-plastic (EP) approach?

Indeed, the elastic (EL) model for quartz (E = 96 GPa) yields slightly better simulation results than the elastic-plastic (EP) model based on the experimentally derived Young's modulus (E = 11 GPa, H/E^* = *0.14*), however there two main arguments raising doubts about the validity of this EL model: (1) Quartz is a major constituent of the granodiorite, however the validity of the EL model implies that contacts along the fracture only occur at quartz grains. In fact, gouge material analyses of granodiorites (Vogler et al. 2016a) indicate that contacts should include all rock forming minerals. (2) The relatively high Young's modulus presupposes intact quartz grains, whereas microstructural analyses show that the Grimsel granodiorites typically possess an interconnected network of microcracks (Schild et al. 2001), which should reduce the actual Young's modulus of quartz (Zimmerman 1985).

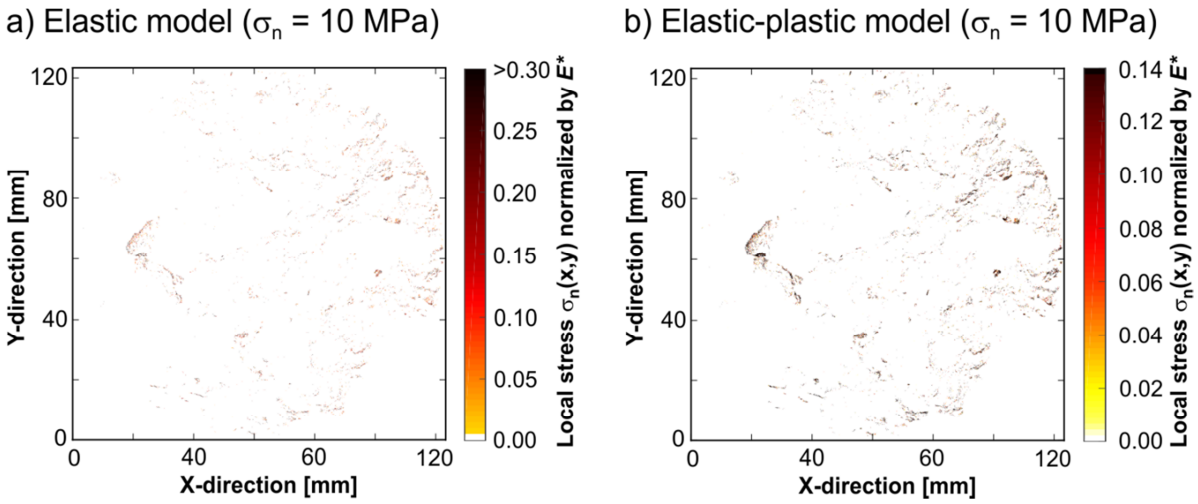

Fig. 2.6: Normalized local contact stresses over the fracture surface at a normal stress σ_n of 10 MPa for the elastic (a) and elastic-plastic (b) model based on the experimentally derived Young's modulus (and relative hardness H/E^* = 0.14).

Hence, the EP model appears to be the physically more realistic approach. This becomes clear, when considering the (normalized) local contact stresses at a normal stress of 10 MPa for the EL model with the experimentally derived Young's modulus (Fig. 2.6a), which indicates that local contact stresses are in excess of the plastic yield criterion (H/E^* = 0.14). Local stresses would be even higher for the EL model based on quartz properties, which exhibits fewer contacts being pressurized. Considering the stress distribution of the EP model (Fig. 2.6b), there is a significant amount of contacts (approximately 55 %) with H/E^* = 0.14, where non-elastic deformation of the microscopically small contacts can be

expected. This assumption is encouraged by the observation of occasional, tiny gouge material, which was found after unloading the sample.

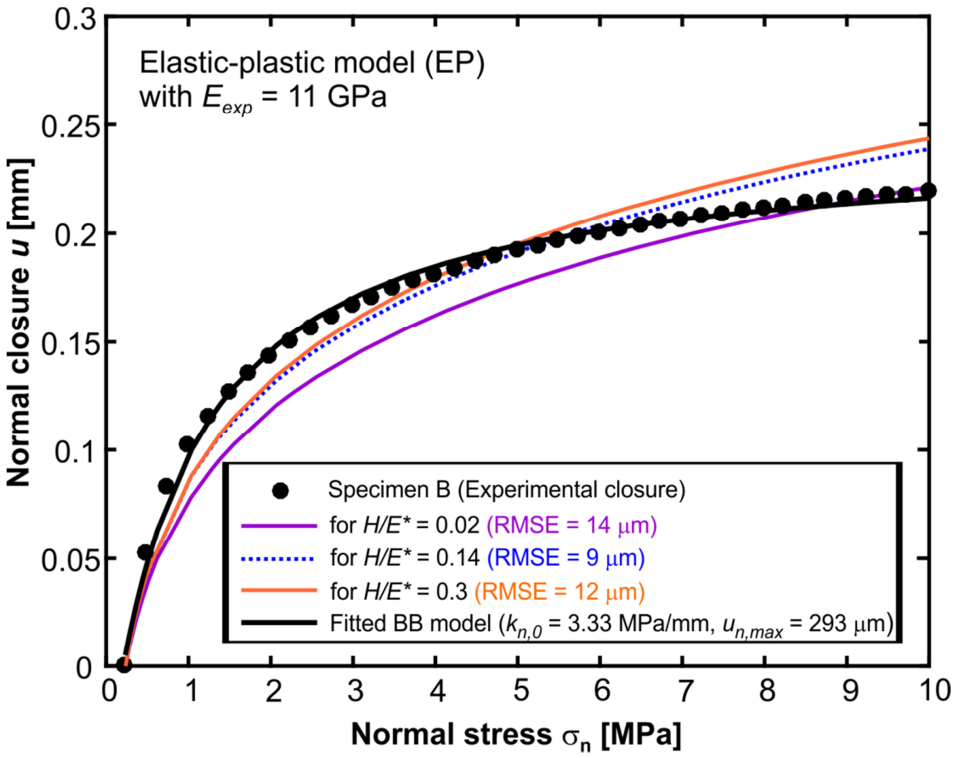

Fig. 2.7: Comparison of experimental and simulated closure for the elastic-plastic contact model using identical Young's moduli and different relative hardness values. The model performance is represented by the root-mean-squared error (RMSE) relative to a fitted Barton-Bandis (BB) model with $k_{n,0}$ = 3.33 MPa/mm and $u_{n,max}$ = 293 μm (according to Eq. 2.5).

Since elastic-plastic deformation is likely, EP simulations are also performed for different possible hardness values derived from Table 2.2, where H/E^* = 0.3 of the Westerley Granite also reflects the upper limit shown by the scatter of empirical data in Fig. 2.4. Additionally, simulations are also exemplarily performed for a very low relative hardness (H/E^* = 0.02), ascribing a pronounced but unlikely non-elastic behaviour of the fracture. Fig. 2.7 shows that the resulting closure increases with increasing hardness. At first sight, this finding appears to disagree with the results of Wu and Sharma (2017), where the total closure increases with decreasing hardness values. However, as mentioned for Fig. 2.5b significant plastic deformation occurs at pre-loading stresses below 0.25 MPa so that further closure is restricted by the stiffening of the fracture due to the earlier accumulation of contacts with decreasing hardness values. Thus, more plastic rock parameters (i.e. $H/E^* > 0.02$) cause a more pronounced stiffening due to the faster accumulation of contacts. Indeed, errors of the "plastic" fracture are very low (< 1 %) at high normal stresses (σ_n = 10 MPa), however are more significant (up to 12 %)

for lower stresses (σ_n < 6 MPa) Since the EL model implies a theoretically infinite relative hardness, it is not surprising that increasing relative hardness values of the EP model slowly approximates the results of EL model curve (cf. Fig. 2.5a). Indeed, the scatter of the empirical data indicates that relative hardness values such as H/E^* = 0.3 are not unlikely, however this value exceeds the supposed upper limit of the surface (H/E^* = 0.12 to 0.2, Table 2.2), when assuming that only quartz minerals are in contact. Thus and in accordance with the simulation results, the estimated relative hardness of 0.14 can be assumed to be representative in this study. However, comprehensive relative hardness studies based on appropriate experiments are recommended for future research.

2.4.3 Model comparison

In comparison with the (non-fitted) empirical Barton-Bandis (BB) model (Eq. 2.5), the root-mean-squared errors (RMSE) of the numerical elastic-plastic (EP) models are similar (Fig. 2.8) so that both approaches fit well with the experimental results. Particularly at normal stresses > 5 MPa the BB model indicates increasing conformance with the experiment, while the EP model performs better at lower stresses (< 5 MPa). In contrast to the BB model, the introduced, analytical "exponential repulsion model" (ERM, Eq. 2.8), which solves the geometrical dependence of the contact problem, requires a fitting (R^2 = 0.99) with the elastic (EL) model to estimate the variables γ = 0.34 and β = 0.27 for the previously assessed roughness h_{rms} = 192 µm, and thus reveals identical deviations as the EL model. It should be mentioned that both fitting parameters are sufficient for the fracture discussed in this study. For other fractures, the variables can differ due to their dependence on fracture topography, where the latter depends on the rock type and grain sizes (e.g. Ogilvie et al. 2006) as well as the fracture mode (e.g. Candela et al. 2009). In a second step, h_{rms} is additionally adjusted to the experimental data by maintaining γ and β so that h_{rms} = 176 µm (R^2 0.98, RMSE = 7 µm). Deviations between the fitted and theoretical h_{rms} (Δh_{rms} = *16* µm) and γ ($\Delta\gamma$ = between 0.06 and 0.16) values can be assigned to both, the validity of the ERM only for elastic contact deformation and uncertainties of h_{rms}, which can be affected by artefacts of the fracturing method.

Deviations of both the elastic-plastic (EP)model and the BB model can be ascribed to several concurrent shortcomings such as (a) simplifications of non-elastic contact deformation, (b) the experimental uncertainties during the back-calculation of the closure, (c) surface scan uncertainties due to the resolution and the application of coating (d) the mineralogical heterogeneity of the granodiorite, which can affect the fracture closure as found by Wu and Sharma (2017) and (e) additional mating of the fracture due to shearing and rotating at early stress stages, which is not captured by the model as previously also discussed by Li et al. 2015. Although, the fracture is located fairly perpendicular to the

cylinder axis, even a very small inclination of the fracture could cause notably lateral movements affecting the experimental closure curve.

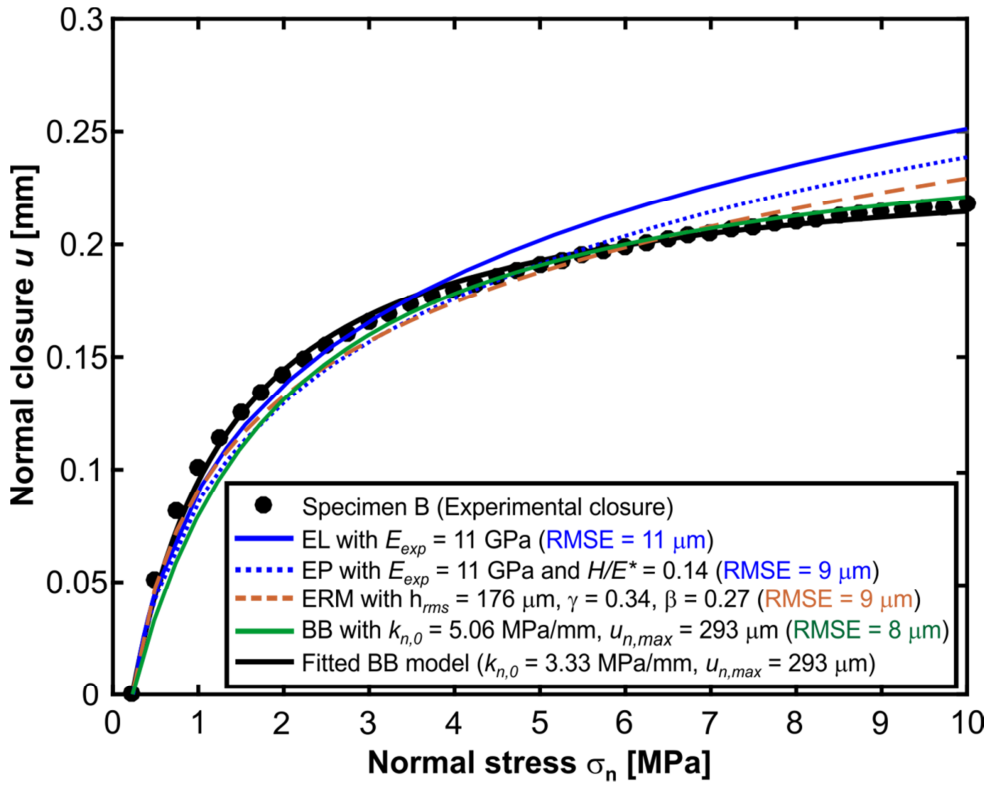

Fig. 2.8: Comparison of closure values derived by applying the elastic (EL) model, elastic-plastic (EP) model and the Barton-Bandis (BB) model for normal closure (Eq. 2.5). The model performance is represented by the root-mean-squared error (RMSE) relative to a fitted Barton-Bandis (BB) model with $k_{n,0}$ = 3.33 MPa/mm and $u_{n,max}$ = 293 µm (according to Eq. 2.5).

Since the mean closure data alone do not confirm the quality of the numerical simulations, resulting apertures are discussed here. Unfortunately, no direct *in situ* aperture measurements are available for the experiment. Hence, the numerical results of the EP model are assumed as a benchmark for the most exact representation of the local apertures. Fig. 2.9a describes the development of the stress-dependent mean mechanical aperture a_m of the EL and EP models, the four interpenetration scenarios (IP1-BB, IP2-BB, IP3 and IP4) and mechanical apertures calculated by the best fitting ERM (h_{rms} = 176 µm). Considering the Barton-Bandis (BB)-based models (IP1-BB and IP2-BB) there are notable deviations to the EL and EP results (Fig. 2.9a). The deviations of IP1-BB and IP2-BB indicate that the BB model combined with the interpenetration approach is not able to properly capture stress-dependent fracture closure. Particularly the large overestimation of the IP2-BB model as also applied by Li et al. (2015) indicates that early deformation and collapses of the initial contacts play an important role for the

subsequent stress-dependent behaviour. By contrast, IP3 and IP4 reveal similar evolutions of stress-dependent mean apertures (Fig. 2.9a). The best fit with the elastic-plastic models is represented by IP4, which for that reason is used for subsequent comparisons on the local scale (Fig. 2.9b, Fig. 2.10 and Fig. 2.11). Notably, the (fitted) analytical ERM approach still is close to the curves of simulated elastic and elastic-plastic models. Hence, the ERM, which only depends on geometrical and elastic properties (E^*), represents a practical alternative to approximate stress-dependent fracture closure as well as aperture evolution and should be reexamined in future studies.

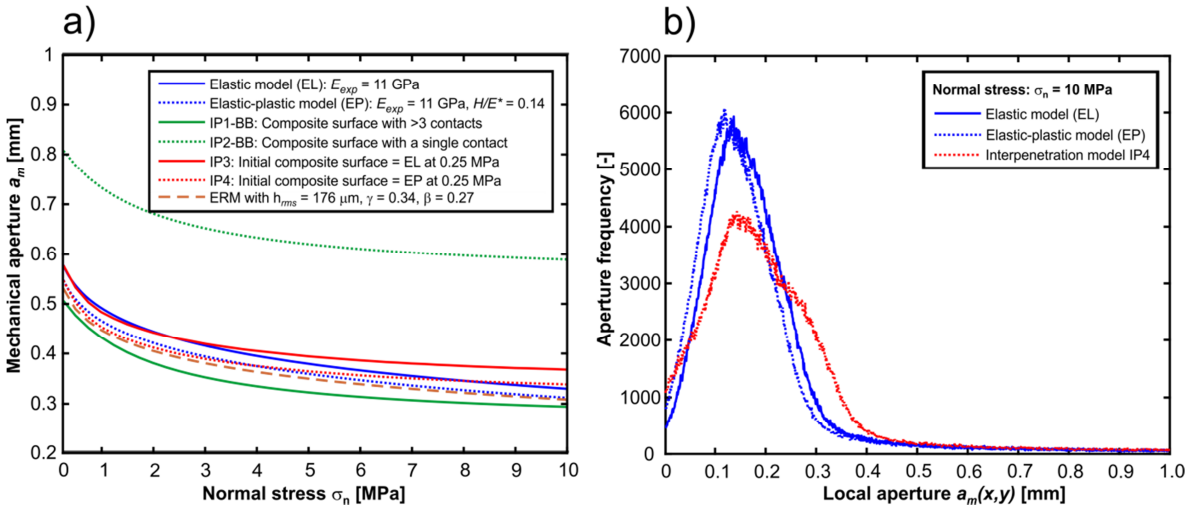

Fig. 2.9: Aperture evolution (a) of the fracture for the elastic (EL) and elastic-plastic (EP) models and four interpenetration scenarios (IP) using the Barton-Bandis model (IP1-BB, IP2-BB) or experimental closure data (IP3, IP4). IP1-BB and IP2-BB start with a hypothesized initial composite surface at 0 MPa. IP3 (and IP4) are based on aperture distributions at 0.25 MPa normal stress received from the EL (and EP) model. Aperture distribution histograms at 10 MPa (b) are shown for the EL and EP models and the IP4 model.

Conforming with the basic idea, the interpenetration model (IP4) reflects its uniform aperture closure by shifting the initial histogram of the aperture distribution towards smaller apertures (Fig. 2.9b). Although IP4 is based on the aperture fields of the elastic-plastic model at 0.25 MPa, the histogram shape of the initial composite surface is observed (Fig. 2.2b), indicating that the simulated "pre-experimental" contact deformations only have negligible effects. Although there are significant differences of simulated normal closure, both the numerical elastic (EL) and elastic-plastic (EP) results at 10 MPa indicate similar mean apertures and aperture distributions as well as fundamental stress-dependent aperture changes inside the fracture (Fig. 2.9b). With increasing stresses the aperture distributions of the numerical simulations become slightly truncated, more right skewed and also reveal longer tails. The increasing right skewness of the aperture distribution curve indicates that local closure inside the fracture must be heterogeneous. This finding also agrees with experimental observations of

stress-dependent fracture closure using *in situ* X-ray computed tomography (CT) scans (Muralidharan et al. 2004; Huo and Benson 2015) and also emphasizes the validity of EP model.

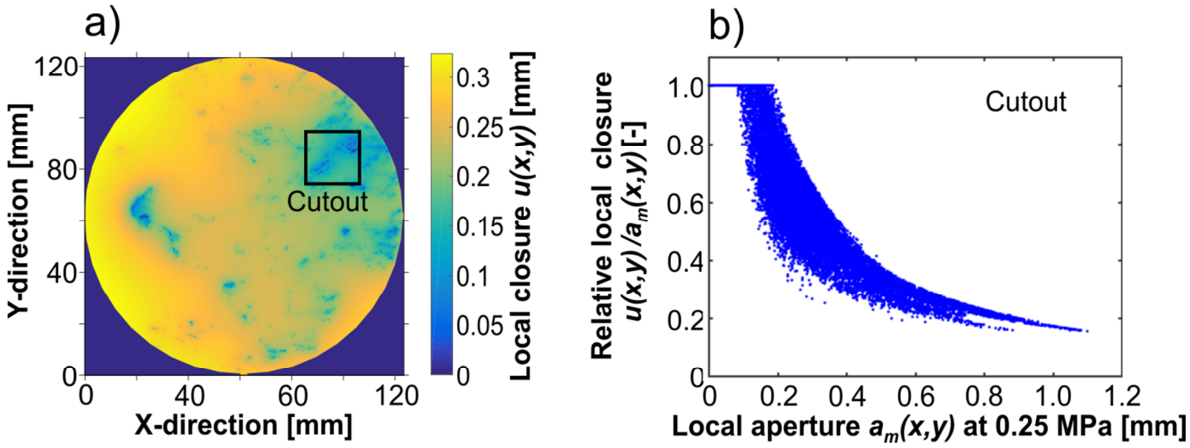

Fig. 2.10: (a) Local closure $u(x,y)$ representing the difference of the aperture fields $a_m(x,y)$ at σ_n = 0.25 MPa and σ_n = 10 MPa for the elastic-plastic (EP) model. Local closure data at σ_n = 10 MPa and local aperture data at σ_n = 0.25 MPa in the cutout of are used to describe (b) the heterogeneous relative closure of local apertures. A relative closure of 1 indicates the complete closure of the aperture.

Referring to this heterogeneity of local closure, Fig. 2.10a shows for the elastic-plastic (EP) model that the most significant local closure (u = 250 to 300 µm) occurs in regions with larger initial apertures. A similar relationship between initial local aperture sizes and magnitudes of stress-dependent closure is also observed for CT-based laboratory tests (Huo 2015), which show that absolute local closure tends to increase linearly with increasing initial aperture size. Based on a cutout, Fig. 2.10b reveals that the smaller the initial aperture size, the larger is the range of possible closure. Hence, the local closure also depends on the vicinity to zones with contact areas, where local contact stresses are concentrated and contact mechanics significantly affect neighboring areas. In such zones, the relative local closure is highly heterogeneous and follows an exponential trend (Fig. 2.10b). Hence, the increasing right skewness of the aperture distribution (Fig. 2.9b) can be explained by more pronounced closure of larger apertures, which was also observed by Huo and Benson (2015), and the incomplete, more heterogeneous closure of smaller apertures.

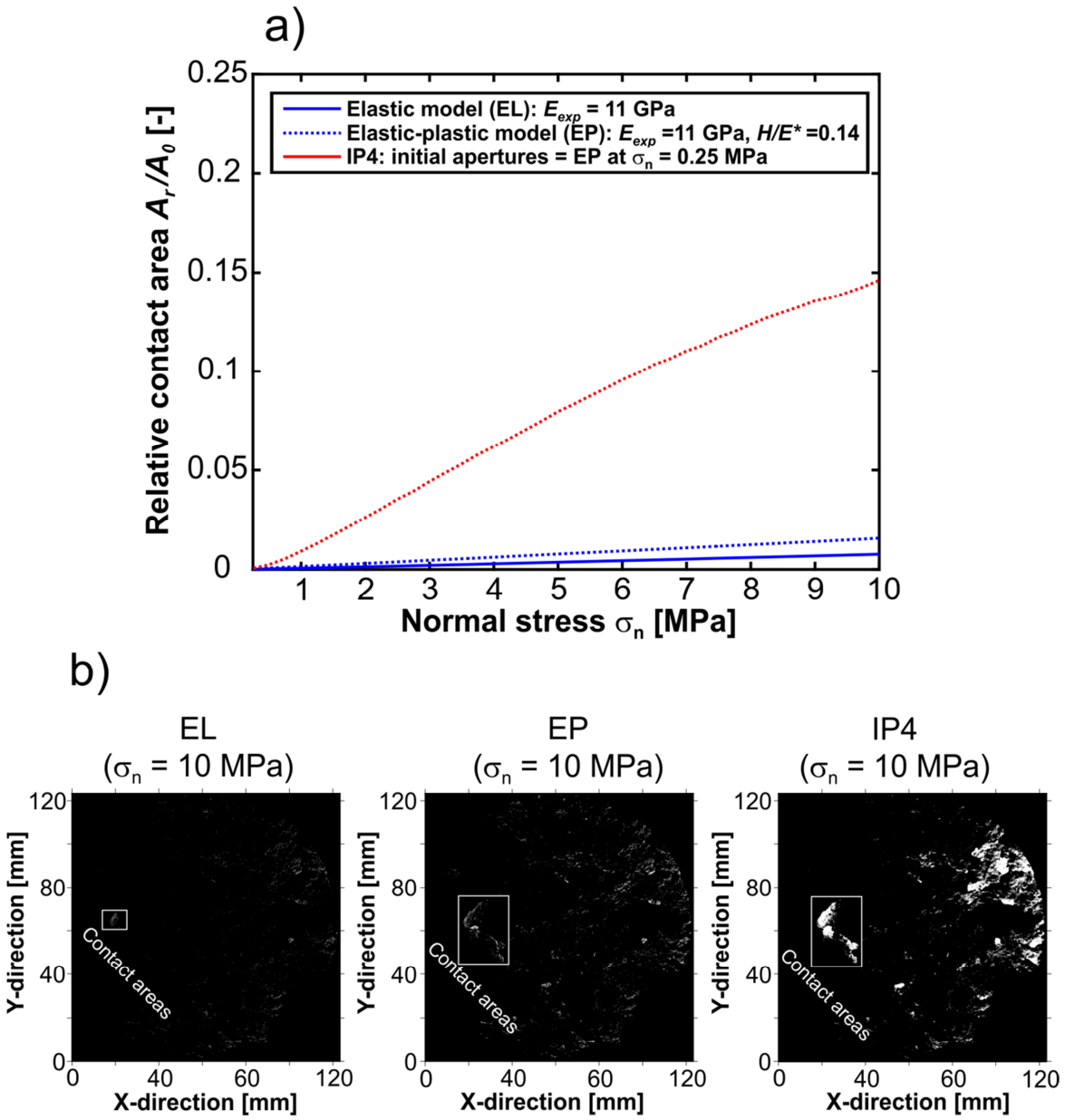

Fig. 2.11: (a) Evolution of the relative contact area of the elastic and elastic-plastic contact model compared to the interpenetration model IP4. (b) Additionally, the spatial contact area distributions of the elastic and elastic-plastic models at 10 MPa are compared to the results of IP4 (b).

Considering simulated contact areas, IP4 show a non-linear increase of contact areas up to 15 % (Fig. 2.11a, Table 2.3). Indeed, contact areas of this magnitude were experimentally observed (e.g. Nolte et al. 1989; Nemoto et al. 2009; Huo and Benson 2015), but should be considered cautiously due to uncertainties of the applied experimental methods such as the resolution of the CT-based imaging techniques, the penetration depth of applied casting materials or the finite thickness of the impression materials. Instead, a high-resolution optical method has shown for roughened calcite and quartz

surfaces at normal stresses up to 10 MPa that contact areas can be significantly below 1 % and reveal a stress-dependent linear increase of contact areas (Dieterich and Kilgore 1996). A linear increase of accumulated contact areas is also observed for the EL and EP models, where relative contact areas are significantly below 2% (Fig. 2.11a). However, while maximum relative contact areas for the fracture are about 1.6 % for the EP model, the EL model only reveals half of it (0.8 %). On a local view (Fig. 2.11b), contact areas of the numerical simulations (EL and EP) are more scattered as the interpenetration models that form more compact "island structures" along regions of low apertures (Pei et al. 2005). Accordingly, the elastic-plastic (EP) model indicates a transition state between the elastic (EL) model and interpenetration model (e.g. IP4, Fig. 2.11b). In accordance with the experimental finding of Dieterich and Kilgore (1996), the linear increase of contact areas indicates that the non-linear closure curve or stiffening of the fracture can be assigned to the rearrangement of local stress along newly closed, expanding and coalescing contact zones, which decelerate further closure.

The key results for the most reliable fracture-closure models (EL, EP and IP4) are summarized in Table 2.3. The main advantages of the EP model are the higher validity with the experimental results and the higher physical reliability, which is emphasized by the more realistic evolution of contact areas and the consideration of heterogeneous local closure. Furthermore, the numerical simulations only require surface scans and reliable material properties (E, υ, H), which can easily be obtained even for closure simulations of multiple fractures, because the only requisite are standard experiments such as uniaxial compression tests on representative (intact) matrix material. In contrast, normal closure analyses of multiple fractures with the interpenetration model would require closure data (e.g. IP3 or IP4) or fracture properties (e.g. IP1-BB or IP2-BB) derived from various fracture-specific and time-consuming experiments.

Table 2.3: Summary of the simulation requirements and results for the numerical elastic (EL) and elastic-plastic (EP) models and the interpenetration model (IP4).

	Elastic model (EL)	Elastic-plastic model (EP)	Interpenetration Model (IP4)
Input			
Closure experiment required	No	No	Yes
Real material properties necessary	Yes	Yes	No
Output			
Closure root-mean-squared error [µm]	11	9	0
Physically valid local stresses	No	Yes	-
Heterogeneous local closure	Yes	Yes	No
Maximum contact areas at 10 MPa [%]	0.8	1.6	14.6
Mechanical apertures a_m at 10 MPa [µm]	323	305	336
Standard deviation s_a at 10 MPa [µm]	615	615	623
Relative roughness s_a/a_m [-]	1.9	2.02	1.85

From a quantitative point of view, there are differences of the aperture histogram shapes (Fig. 2.9b), however deviations in the mean mechanical apertures a_m and their standard deviations s_a of the numerical results and IP4 are minor (Table 2.3). In comparison with the initial standard deviation (s_a = 624 µm) of the composite surface (Fig. 2.2b), s_a of the EL and EP models decreases by approximately 9 µm after applying 10 MPa, while s_a of IP4 only decreases by 1 µm (Table 2.3). Such a decrease of s_a is also observed by *in situ* CT scans, where s_a is 61 µm lower after applying 10 MPa on a sandstone fracture (Muralidharan et al. 2004). It has to be mentioned that calculated mean mechanical apertures a_m considered in this study, also comprise larger apertures at the boundary of the fracture, which implicate a systematic overestimation of a_m. Hence, a_m (at 10 MPa) is also calculated for rectangular cutout, which does not involve these boundaries, indicating for the three scenarios significant lower a_m (between 177 and 195 µm) and s_a (between 184 and 189 µm) revealing a relative roughness of about 1.

Thus, applying the discussed fracture properties (s_a and a_m) in order to estimate hydraulic properties with simple empirical approaches (Kling et al. 2017 and references therein) would not show any significant differences between the three models. However, actual fracture flow typically depends on

the contact areas (e.g. Zimmerman et al. 1992; Zimmerman and Bodvarsson 1996; Oron and Berkowitz 1998) and local apertures forming a connected and tortuous channel network (e.g. Tsang 1984; Kling et al. 2016). In this context, Dapp et al. (2012) show that using an equivalent numerical simulation approach for elastic contact deformation of a rough surface instead of an IP model significantly affects the scale-dependent percolation behaviour. Hence, the local differences of the numerical simulations (EL and EP) and the interpenetration model (IP4) could also affect subsequent simulations considering reactive or non-reactive transport (e.g. Bodin et al. 2003; Kosakowski 2004; Walsh et al. 2008; Zhao et al. 2011; Lee et al. 2015) and multiphase problems (e.g. Chen and Horne 2006; Yang et al. 2013; Develi and Babadagli 2015; Ye et al. 2015), where contact areas and local apertures play an important role. Another advantage of the numerical simulations is that they provide information about local contact stress, which is important for reactive transport simulations, where pressure-dissolution can play a significant role (e.g. Lang et al. 2015, 2016; Li et al. 2015). Thus, the elastic-plastic (EP) model is recommended due to its model performance and the physically more valid treatment of local contact stresses. However, for simple (non-reactive) fracture flow studies and in the case of hard rock samples such as studied here, the elastic (EL) model is expected to reveal similar results due to the slight deviations of the simulated aperture and contact distributions.

2.5 Conclusion

A Fast Fourier Transform (FFT)-based contact mechanical simulation approach for a circular granodiorite fracture was validated, considering the general and local stress-dependent closure behaviour of the fracture, which provided the following key findings:

- The results for the elastic-plastic contact model fit well with experimentally derived closure data. Although it is often presumed for hard rock samples such as granodiorite that an elastic model is sufficient, local contact stresses along the fracture indicate that non-elastic deformation cannot be neglected. Nevertheless, stress-dependent aperture evolution indicates that both the elastic and elastic-plastic model should reveal similar results, when considering subsequent single-phase flow studies. However, the elastic-plastic model is recommended particularly for subsequent fracture studies focussing coupled thermal-hydro-mechanical-chemical (THMC) simulations as well as for softer rock samples such as many evaporites (e.g. limestone, halite and anhydrite) or mudstones.
- The performance of the elastic-plastic models mostly depends on the appropriate choice of material properties such as Young's modulus and indentation hardness. It was found that the choice of the experimental Young's modulus (E = 11 GPa) reveals the best results. Using too high values (E >> 11 GPa) leads to a larger mismatch between numerical and experimental

results. Additionally, a theoretical relative hardness of 0.14 for granitic rocks was derived, which was found to be applicable for the granodiorite fracture in this study.

- In comparison with often applied analytical and interpenetration models, the elastic-plastic model has the advantage that it reproduces heterogeneous local closure and provides contact areas significantly below 2 % even at normal stresses of 10 MPa, which agrees well with experimental observations from literature.

Acknowledgement

This study was mainly carried out within the framework of the Helmholtz Association of German Research Centres (HGF) portfolio project “Geoenergy” and is part of the comprised reservoir engineering cluster. LP acknowledges funding by the Deutsche Forschungsgemeinschaft (grant PA 2023/2). Daniel Vogler gratefully acknowledges funding from the Swiss Competence Center for Energy Research – Supply of Electricity (SCCER-SoE). We thank Mark Robbins for useful discussion. Finally, we also thank the Editor-in-Chief Prof. Barla and the anonymous reviewer for their helpful comments and suggestions that improved the manuscript.

.

Chapter 3

Simulating stress-dependent fluid flow in a fractured core sample using real-time X-ray CT data

Reproduced from: Kling T, Huo D, Schwarz JO, Enzmann F, Benson S, Blum P (2016): Simulating stress-dependent fluid flow in a fractured core sample using real-time X-ray CT data. Solid Earth, 7:1109-1124, doi:10.5194/se-7-1109-2016.

Abstract

Various geoscientific applications require a fast prediction of fracture permeability for an optimal workflow. Hence, the objective of the current study is to introduce and validate a practical method to characterize and approximate single flow in fractures under different stress conditions by using a core-flooding apparatus, *in situ* X-ray computed tomography (CT) scans and a finite-volume method solving the Navier–Stokes–Brinkman equations. The permeability of the fractured sandstone sample was measured stepwise during a loading–unloading cycle (0.7 to 22.1 MPa and back) to validate the numerical results. Simultaneously, the pressurized core sample was imaged with a medical X-ray CT scanner with a voxel dimension of 0.5 × 0.5 × 1.0 mm³. Fracture geometries were obtained by CT images based on a modification of the simplified missing attenuation (MSMA) approach. Simulation results revealed both qualitative plausibility and a quantitative approximation of the experimentally derived permeabilities. The qualitative results indicate flow channeling along several preferential flow paths with less pronounced tortuosity. Significant changes in permeability can be assigned to temporal and permanent changes within the fracture due to applied stresses. The deviations of the quantitative results appear to be mainly caused by both local underestimation of hydraulic properties due to compositional matrix heterogeneities and the low CT resolution affecting the accurate capturing of sub-grid-scale features. Both affect the proper reproduction of the actual connectivity and therefore also the depiction of the expected permeability hysteresis. Furthermore, the threshold value CT_{mat} (1862.6 HU) depicting the matrix material represents the most sensitive input parameter of the simulations. Small variations of CTmat can cause enormous changes in simulated permeability by up to a factor of 2.6 ± 0.1 and, thus, have to be defined with caution. Nevertheless, comparison with further CT-based flow simulations indicates that the proposed method represents a valuable method to approximate actual

permeabilities, particularly for smooth fractures (< 35 µm). However, further systematic investigations concerning the applicability of the method are essential for future studies. Thus, some recommendations are compiled by also including suggestions of comparable studies.

3.1 Introduction

Naturally and artificially induced hydromechanical coupling is essential for the understanding of many geologic processes within the Earth's crust and for the successful realization of a wide range of geoscientific applications. A more detailed overview about these applications such as geothermal energy generation, nuclear waste disposal or hydrocarbon production is presented by Rutqvist and Stephansson (2003). Since there are different phenomena of direct and indirect hydromechanical coupling in geosciences, this study only deals with the direct solid-to-fluid coupling, which is defined as the stress-induced changes in fluid dynamics (Wang 2000).

In the past, the stress dependency of fracture permeability and its hysteretic behavior due to stepwise loading and subsequent unloading were investigated by various authors (e.g. Snow 1965; Gangi 1978; Kranz et al. 1979). Various empirical models were developed that approximate stress-dependent fracture permeability by adding roughness-based variables to the common cubic law approach (Gangi 1978; Witherspoon et al. 1980; Walsh 1981; Gale 1982; Swan 1983; Bernabe 1986a; Zimmerman et al. 1992; Huo and Benson 2015). However, flow in rough fractures is governed by several additional morphology-related features, such as the grade of connectivity, variations in tortuosity, flow separation and stagnant zones (Tsang 1984; Konzuk and Kueper 2002), that are hard to quantify empirically.

Hence, numerical simulations that allow the implementation of much more sophisticated physical solution approaches and boundary conditions represent a powerful tool in modern geosciences. Accordingly, there is an immense number of computational fluid dynamics (CFD) studies concerning different topics such as single-phase and multi-phase flow (Sahimi 2011), natural (Crandall et al. 2010) and artificial fractures (Brush and Thomson 2003) or fractured porous media (Landry and Karpyn 2012). The same applies to CFD methods, which are most frequently represented by finite- difference, finite-element, lattice gas and lattice Boltzmann methods (Madadi and Sahimi 2003). In particular, the lattice methods are suggested by Madadi and Sahimi (2003) as the ideal computational base for arbitrary geometries. In addition to that, the finite-volume method has been increasingly and successfully used to simulate fracture flow in the last few years (Brush and Thomson 2003; Al-Yaarubi et al. 2005; Crandall et al. 2010; Huber et al. 2012; Schwarz and Enzmann 2013). However, in practice, solving three-dimensional (3-D) mathematical models such as the Navier–Stokes equation with these methods can be computationally elaborate so that many simulations prefer simplified flow models such as the "local cubic law" approach (Oron and Berkowitz 1998; Konzuk and Kueper 2002; Brush and Thomson 2003; Koyama et al. 2008; Zimmerman and Yeo 2013).

Table 3.1: Numerical simulations of stress-dependent single-phase fracture flow considering the sample and fracture type, the method to reproduce fracture apertures, the model dimensions and simulation methods.

References	Core sample (length/diameter)	Fracture type	Source of model geometry (Aperture translation method)	Volume element dimension (represented fracture area)	Dimen-sions	Simulation type (Solver)
Pyrak-Nolte and Morris (2000)	Granites (literature data)	Artificial	Fractal aperture distributions (Stratified Percolation method)	300 × 300 cubic grid blocks (100 × 100 mm²)	2.5D	Network model (Hardy-Cross method)
Kim et al. (2003)	Granite (16.4 cm/14.0 cm)	Tensile (mated and offset)	Profilometer measurements	0.05 × 0.05 mm × >0.008 mm³ (111 to 116 × 128 mm²)	3D	LB (Navier-Stokes)
Dicman et al. (2004)	Sandstone (2.54 cm/5.99 cm)	Tensile	Average aperture (Stochastic aperture distribution map)	1 × 1 ×1 grid block (10 × 10 ×15 grid blocks)	3D	FD (Local cubic law)
Watanabe et al. (2008)	Granite (15.0 cm/10.0 cm)	Tensile (mated and offset)	Laser-scanning equipment	0.25 × 0.25 mm² (sample scale)	2.5D	FD (Local cubic law)
Nemoto et al. (2009)	Granite (15.0 cm/9.5 cm)	Shear fracture for experiment, tensile (offset) for simulation	Laser-scanning equipment and thin film technique	0.25 × 0.25 mm² (50× 50 mm²)	2.5D	FD (Local cubic law)
Liu et al. (2010)	Coal and Sandstone (10.0 cm/5.0 cm)	Shear fracture	Conceptual side view	100 × 25 four-node mesh (none)	2D	FE (Fluid/solid coupling model)
Watanabe et al. (2011; 2013)	Granite (15.0 cm/10.0 cm)	Tensile (mated) and natural (double fractured)	Medical CT scanner (Peak Height method)	0.35 × 0.35 × 0.50 mm³ (sample scale)	3D	FD (Local cubic law)
Indraratna et al. (2015)	Sandstone (11.4 cm/5.4 cm)	Tensile (mated)	Laser-scanning equipment	1.0 × 1.0 mm² (sample scale)	2.5D	FV (Navier-Stokes)
Current	Sandstone (6.7 cm/5.0 cm)	Saw cut (smooth, mated)	Medical CT scanner (Missing Attenuation method)	0.50 × 0.50 × 1.00 mm³ (sample scale)	3D	FV (Navier-Stokes-Brinkman)

Various studies concerning numerical simulations of stress-dependent fracture flow in core-scale dimensions have been performed until now. Table 3.1 provides a chronological list of previously performed studies. All these simulations focus on dynamic changes of fracture permeability due to loading conditions. However, they do not address residual changes as a result of mechanical deformation within the fracture, which can be addressed by subsequent unloading. Except the study by Watanabe et al. (2008), who highlight qualitative insights into the flow structures, all other studies in Table 3.1 quantify and intend to validate simulated fracture flow. In a subsequent study which is not listed in Table 3.1, Watanabe et al. (2009) applied a similar (non-quantitative) procedure for other fracture types. By contrast, quantification of fracture flow was performed by Indraratna et al. (2015), who performed CFD simulations based on initial laser-scanning measurements, where the flow model

is coupled with a deformation criteria simulating fracture closing. Similar, but more simplified, deformation procedures were performed for statistically derived aperture distributions (Pyrak-Nolte and Morris 2000), profilometer measurements (Kim et al. 2003), laser-scan data (Watanabe et al. 2008, 2009; Nemoto et al. 2009) and a conceptual 2-D model (Liu et al. 2010). Furthermore, Dicman et al. (2004) described changes in aperture distribution by combining laboratory data and stochastic approaches. Considering this study and further information provided in Table 3.1, most of the used fracture geometries can be assumed to be not directly correlated to the actual fracture geometries under loading conditions used for validation. For this reason, more recent studies introduced X-ray computed tomography (CT) that enables the scanning of *in situ* conditions during the experiment within the sample and creates "real-time" images of the fracture (Watanabe et al. 2011, 2013).

In the past, *in situ* imaging of experiments based on CT technologies was applied to a wide range of studies including geomechanical behavior of fractures (Re and Scavia 1999), evaluations of triaxial tests (Vinegar et al. 1991; Ge et al. 2001; Feng et al. 2004; Ren and Ge 2004; Lenoir et al. 2007; Zhou et al. 2008), shear tests (Tatone and Grasselli 2015), sand production experiments (Santos et al. 2010) as well as various single-/multi-phase core-flooding experiments in fractured and unfractured rocks (Schembre and Kovscek 2003; Rangel-German et al. 2006; Shi et al. 2009; Perrin and Benson 2010; Watanabe et al. 2011; Krevor et al. 2012; Pini et al. 2012; Oh et al. 2013; Pini and Benson 2013; Huo and Benson 2015). CT technology generally represents a 3-D non-destructive method to image material contrasts in high resolution and, therefore, is well suited to reproduce dynamic processes *in situ* and in "real time". Detectable material contrasts can be caused by significant changes in density, such as the transition from solid to air, or chemical composition affecting the X-ray attenuation. In this study, the term "real time" refers to a non-continuous but stepwise imaging of a sample being subjected to a dynamic process.

Comparing other appliances such as industrial, micro- or synchrotron-based CTs, medical CT scanners admittedly operate with the lowest resolutions. However, they generally have the advantage of lower scanning times and are more flexible in terms of sample/equipment weights and sizes (Watanabe et al. 2011). Currently, medical CT scanners represent the most economical option to conduct such experiments and also provide, particularly in regard to their importance in medicine, a good accessibility.

The central issue concerning CT measurements and fractured rocks is given by the aperture calibration based on measured material contrasts. Considering a transect perpendicular to the fracture plane, there are generally four methods to calibrate apertures caused by the fracture-related density anomaly (Ketcham and Carlson 2001; Ketcham et al. 2010). (1) The peak height (PH) method is based on the gap between the idealized matrix density and the negative peak of the anomaly, which was successfully

applied by Watanabe et al. (2011) but typically is more applicable for homogeneous materials (Ketcham et al. 2010). The PH method requires a careful calibration. 2) The missing attenuation (MA) method, which integrates the entire anomaly area, was meanwhile refined for smaller apertures and can also be used for heterogeneous rocks and, theoretically, does not require calibration (Huo et al. 2016). (3) The full-width-half-maximum (FWHM) method uses the midpoint between matrix and peak value; however, it is only applicable to larger apertures (Ketcham 2010) and less accurate than the MA method (Van Geet and Swennen 2001). (4) The inverse point-spread function (IPSF) method represents a hybrid between PH and MA methods and iteratively reconstructs fractures by using an IPSF accounting for the blurring of the CT image. Indeed, IPSF method is well suitable to calculate apertures and also is applicable for heterogeneous materials. However, this method is computationally expensive due to the complex numerical deconvolution (Ketcham et al. 2010). Indeed, Watanabe et al. (2011) introduced a useful method to simulate stress-dependent fluid flow based on CT images and in fracture-scale before. However, their method revealed several limitations: (A) simulations are very sensitive to image noise due to the core holder; (B) the aperture calibration that is based on the PH method needs a careful and very time-consuming calibration; and (C) the applied CFD simulation relies on a simplified fluid dynamics represented by the "local cubic law" approach. Particularly for field work, where time often plays a significant role, a functional approach without time-consuming operation procedure and costly equipment can be an asset. Thus, a method would be necessary that only requires a fast CT scan of a pressurized dry sample to predict fluid flow under predefined boundary conditions.

The objective of this study is therefore to propose a practical approach based on real-time X-ray CT data to numerically validate and reproduce stress-dependent single-phase fluid flow in a fractured sandstone sample. This simulation approach consists of (1) an aperture calibration approach for 3-D simulations based on a modification of the simplified MA method (MSMA) and (2) a sophisticated simulation method that accounts for fracture and matrix flows by solving the Navier–Stokes–Brinkman equation. To demonstrate the effectiveness of this method and to also indicate the transferability to real reservoir rocks such as an enhanced geothermal system (EGS), a fractured low-permeable sample is used. In the present study, the fluid flow is simulated under loading and unloading conditions to prove the extent to which it is possible to reproduce flow characteristics and residual fracture changes. Imaging is performed by simultaneously conducting medical CT scans and core-flooding experiments, allowing the validation of the simulated results. Furthermore, current simulations are compared to corresponding studies (Watanabe et al., 2011, 2013) providing various insightful recommendations for the successful implementations of future CT-based CFD simulations.

3.2 Material and Methods

3.2.1 Sample

In this study a Zenifim sandstone is used, which was obtained from the former (unproductive) hydrocarbon prospection well Ramon-1 located in the central Negev area in southern Israel (Fig. 3.1). The rock belongs to the sea marginal deposits of the arkosic Zenifim Formation (Precambrian age) and originates from 1770 m below surface. Additional information on geology and stratigraphy can be obtained by Weissbrod and Sneh (2002). According to Huo and Benson (2015), who used the same sample in their study, the sample is sedimentologically classified as an immature feldspathic greywacke. The sample is composed of poorly sorted and rounded grains with a mean grain size of 0.2 mm. The matrix is cemented by quartz resulting in low mean permeability of 5.92×10^{-19} m² and porosity of 2.5 to 3.9 % with a bulk density of 2,490 kg m^{-3} (mercury injection capillary pressure (MICP) analysis). However, microscopic analyses (Huo and Benson 2015) and visible fine laminations with a thickness of a few millimeters, which dip towards the core axis, indicate a significant porosity heterogeneity within the core.

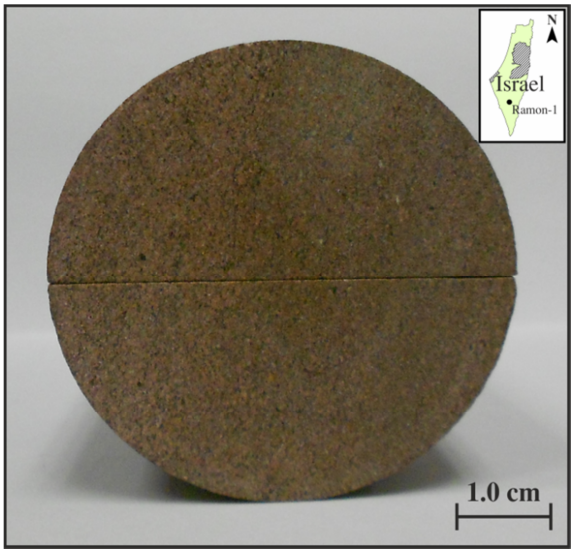

Fig. 3.1: Top view of the fractured Zenifim sandstone with a diameter of 5.0 cm and a length of 6.7 cm.

The utilized rock sample is a continuously cylindrical core sample with a length of 6.7 cm and a diameter of 5.0 cm (Table 3.1, Fig. 3.1). Before the coupled experiments, the sample was bisected along the core axis by generating a saw-cut fracture intersecting the previously mentioned laminations resulting in a discontinuity, which can be described as a (mated) smooth-walled and relatively tight

fracture. It should be noted that abrasion processes and local grain disruptions due to the sawing process result most likely in some minor artifacts along the fracture surface.

3.2.2 Experiment

An aluminum core holder was used for the core-flooding experiment (Fig. 3.2). This experimental setup is based on the a porosity heterogeneity study by Perrin and Benson (2010) and was modified and successfully adapted for core-flooding experiments in porous (Pini et al. 2012) and fractured rocks (Huo and Benson 2015). The fractured core is positioned in an aluminum core holder with alternating interlayers of Viton rubber, heat-shrinkable Teflon and nickel foil that can also be seen on the CT image (Fig. 3.3). For further technical details please refer to Huo and Benson (2015), who used the same experimental setup.

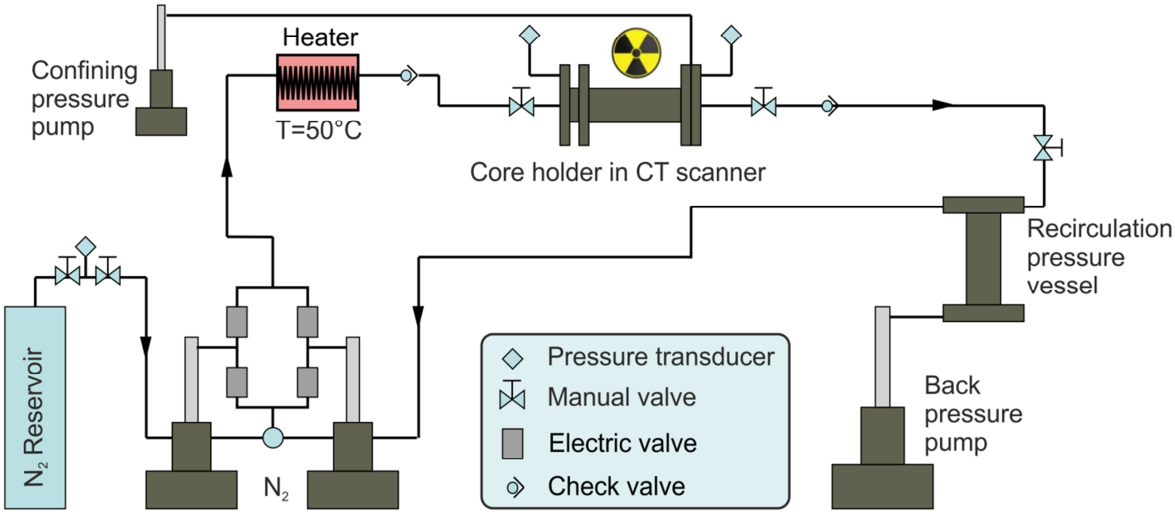

Fig. 3.2: Schematic setup of the core-flooding apparatus for single phase (N_2) flow experiments (after Huo and Benson (2015)).

Permeability measurements of the core sample are based on the steady-state method. After saturating the encapsulated sample with nitrogen (N_2), three different flow rates (12, 16 and 20 mL min^{-1}) are successively applied. A constant pore pressure of 2.1 MPa is applied to suppress the slippage effect. Hence, the applied low flow rates and corresponding small pressure drops reveal a linear relationship indicating laminar fluid flow. Hence, in this study the fluid can be treated like an incompressible fluid and permeability can be determined by using Darcy's law (Huo and Benson, 2015).

According to this, permeabilities are determined under stepwise changes of effective stress (σ'). Here, σ' is defined as the difference between applied confining pressure and pore pressure. In order to

characterize stress dependency of the fractured sample comprehensively, changes in σ' represent a full loading–unloading cycle. Following this, σ' is increased stepwise from 0.7 MPa (2.1, 3.5, 5.5, 11.0 MPa) to 22.1 MPa under loading conditions and, subsequently, are decreased by applying equivalent stress intervals.

Contemporaneously, the core holder is positioned in a medical X-ray CT scanner (General Electric Hi-Speed CT/I X-ray computed tomography) to reveal "real-time" images of the sample for every stress stage. Scans were performed at an energy level of 120 keV, a tube current of 200 mA and a display field of view of 25 cm. We use CT scans to obtain an x−y resolution in the plane of 0.5 × 0.5 mm² and a slice thickness of 1 mm resulting in corresponding voxel dimensions. As a result of the CT scans each voxel is assigned to a specific CT number in Hounsfield units (HU). Furthermore, at each stress stage, multiple (five) scans are conducted and averaged afterwards, representing a practical method to reduce the random noise of CT scans by 50 % as extensively discussed by Huo et al. (2016) and Pini et al. (2012).

3.2.3 Image processing

The geometry of the model is based on the averaged, multiple CT scan revealing a cylindrical set with a total dimension of 256 × 256 × 68 voxels that still contains the multilayer construction of the core holder as well as the filter plates of the fluid in- and outlet. Full processing is performed by using a customized MATLAB code. After reading the five data sets, every CT scan is resampled to an isotropic voxel size (one voxel of 0.5 × 0.5 × 1.0 to 16 voxels of 0.25 × 0.25 × 0.25 mm³) required for a proper computation of the CFD program. Subsequently, the five scans are averaged to a single image (Fig. 3.3). In a further step, geometric information stored by single CT numbers of the (resampled) voxels are transformed voxel-wise to according geometric (local apertures) and hydraulic (local permeabilities) properties being essential for the flow simulations. The corresponding calibration approach is explained fully in the next paragraph. Finally, the core holder and filter plates are numerically cropped based on known core dimensions and obvious density contrasts, resulting in a final sample dimension of 194 × 194 × 258 voxels. Note that marginal voxels of the sample are directly affected by the adjacent core holder so that the processed sample is slightly smaller than expected (200 × 200 × 268 voxels).

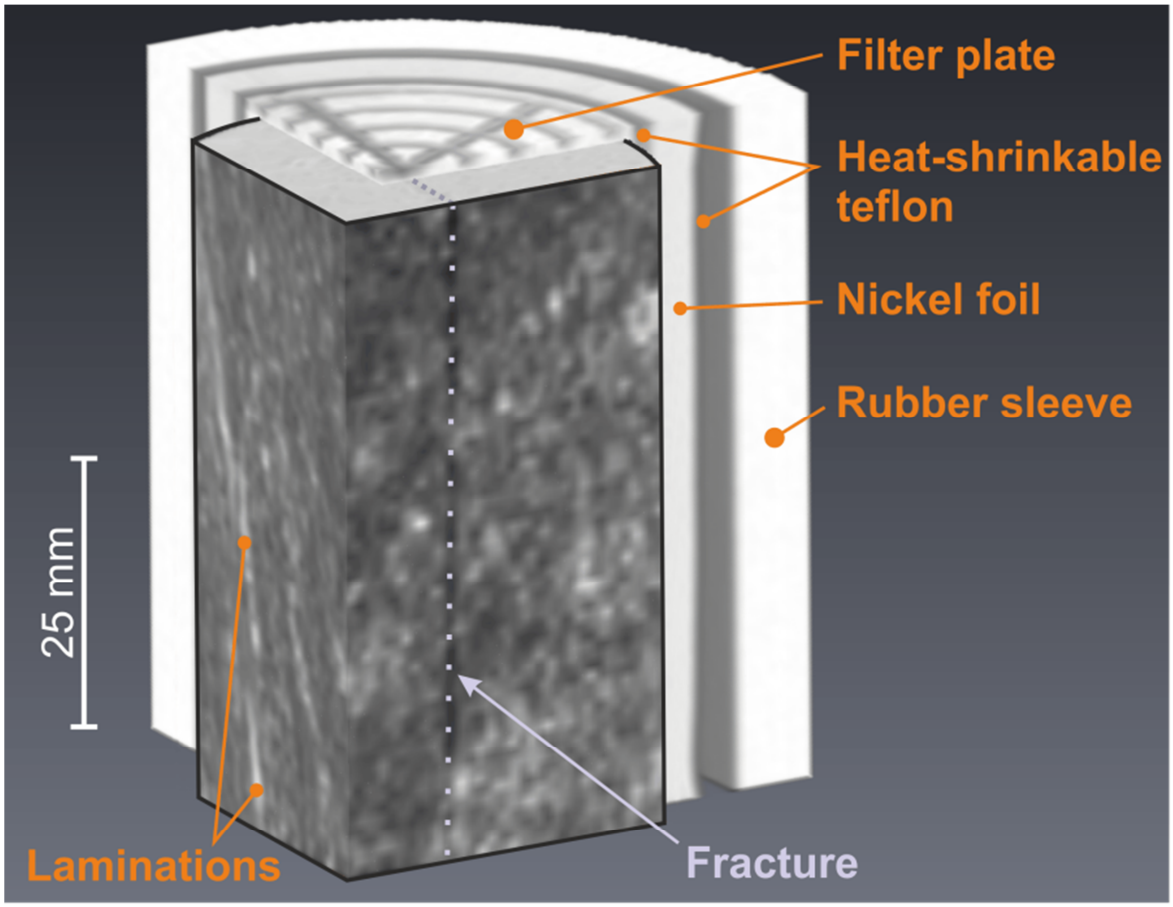

Fig. 3.3: The computed tomography (CT) image of the rock sample with a rescaled voxel dimension (0.25 × 0.25 × 0.25 mm³). The upper filter plate, the units of the core holder and lamination of the sample are highlighted in orange. The fracture is indicated by a dotted purple line.

Aperture calibration is based on the phenomena that the presence of (low-density) air or nitrogen, as used in this study, in a homogeneous rock matrix reduces CT numbers of voxels containing present voids. Considering a fractured homogeneous rock along a cross section perpendicular to the fracture plane, the resulting density contrasts can be perceived as a more or less pronounced anomaly depending on fracture width. Thus, an aperture calibration method (MA method) was developed by Johns et al. (1993) assuming that all X-ray attenuation is conserved in the CT image and that local apertures can be derived by integrating the available density anomalies. Dispersion of X-ray attenuation and partial volume effects can cause an expansion of the anomaly over adjacent voxels that gather this "missing attenuation" (Johns et al. 1993) and, in particular for larger fractures, represent a large portion of the entire anomaly. According to that, Johns et al. (1993) suggested a calibration-based linear relationship between aperture width and the integral of the full measured anomaly which was subsequently confirmed in several fracture aperture studies (Keller 1997; Bertels et al. 2001; Van Geet and Swennen 2001; Vandersteen et al. 2003; Ketcham et al. 2010; Weerakone and Wong 2010;

Heriawan and Koike 2015; Huo and Benson 2015) and physically established by Huo et al. (2016). Accordingly, the linearity between missing attenuation (CT_{MA}) and fracture aperture *a* can be simply described as

$$CT_{MA} = C \cdot a \tag{3.1}$$

where the constant C is given by the slope of the calibration line. Furthermore, CT_{MA} is defined as

$$CT_{MA} = \sum_{i=1}^{N} (CT_{mat} - CT_i) \tag{3.2}$$

where CT_i represents the CT number of the voxel along the cross section affected by the missing attenuation and N localizes the considered voxel. In this study, CT_{mat} represents an idealized global threshold value for the matrix material assuming a homogeneous rock matrix as also assigned in previous studies (Johns et al. 1993; Keller 1997; Keller et al. 1999). Indeed, using a global CT_{mat} is a simplified assumption and provides additional errors particularly for heterogeneous rocks (Keller 1997) but is sufficient for the intended straightforward purposes of this study. Usually, heterogeneous rocks would require the usage of local CT_{mat} values (e.g. Huo et al. 2016) which would result in a large number of possible simulation results and would not improve the validity of the presented results. CT_{mat} is determined by averaging the single modes of all CT numbers at every pressure stage, assuming that the most frequent CT number dominates the matrix of the rock sample. Our results reveal a matrix number of CT_{mat} = 1862 HU, which is in line with other CT-based sandstone studies (Vinegar et al. 1991; Akin and Kovscek 2003; Kling et al. 2016).

Careful calibration with different spacers (0.19, 0.29, 0.41, 0.52 mm) within the fracture indicates a slope of the linear calibration line of 5890 ± 38.3 HU mm^{-1} (Fig. 3.4, after Huo et al. 2016). According to Eq. (3.1) and (3.2), apertures can therefore be calculated by

$$a = \frac{\sum_{i=1}^{N}(CT_{mat} - CT_i)}{5890 \pm 38.3\ HU/mm} \tag{3.3}$$

As a consequence, Eq. (3.3) (with N > 1) can be used to describe local apertures along the fracture; however, it is not practical to model the entire core sample. Typically, the MA in voxels adjacent to the voxel containing the fracture depends on rock type and aperture size (Huo et al. 2016). Considering several cross sections through the fracture used here indicates that occasional local apertures affect 2 – 3 voxels, where the vast majority (≥ 99 %) of the attenuation is captured by the central voxel causing a local but marginal information loss. Hence, assuming that the main information about fracture aperture

is stored in one voxel, we define N = 1, which also benefits the calculation of apertures for every single voxel of the core sample. However, it is worth mentioning that the applied calibration method would get more and more erroneous with increasing fracture widths. However, whether a fracture is large or not is also coupled to the CT resolution; thus, the voxel-wise calibration would cause artifactual apertures in the adjacent voxels actually representing the matrix and also would underestimate apertures in the voxels containing the fracture. In this study, most voxels containing the fracture range between 1700 and 1820 HU, suggesting that calculated (and summarized) apertures of each aperture cannot exceed 0.15 mm and most widely are significantly smaller than 0.1 mm. This corresponds to Huo and Benson (2015), who determined mean apertures between 0.025 and 0.031 mm. Negative apertures due to $CT_i > CT_{mat}$ as a result of the heterogeneity of the matrix or due to remaining image noise are defined as "zero apertures" with $a = 0$ mm.

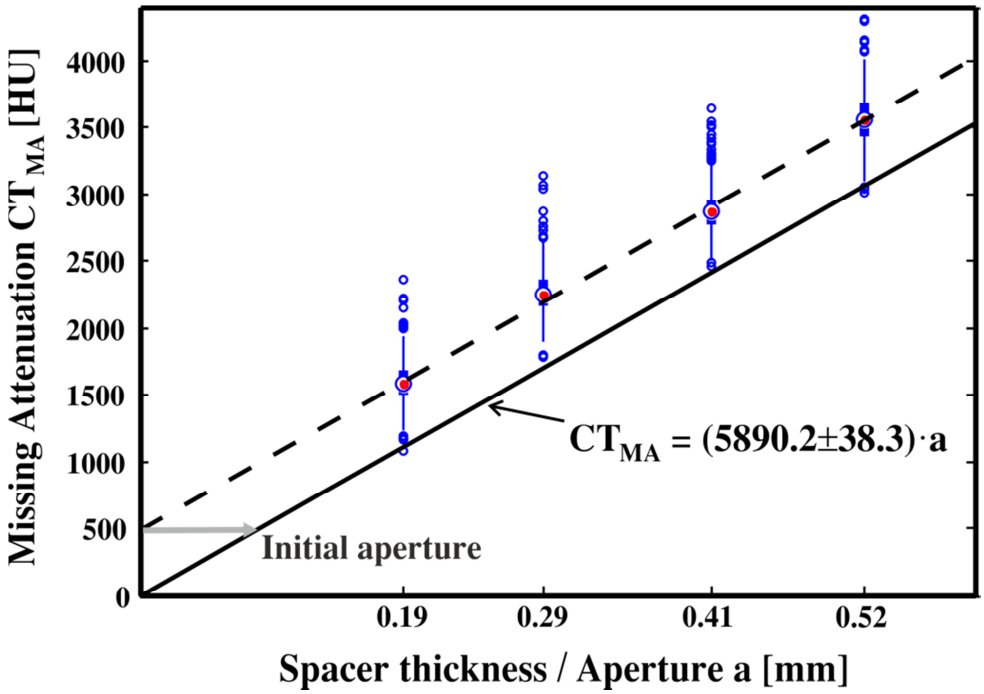

Fig. 3.4: Calibration based on a total of 380 points at each spacer in order to apply the missing attenuation method. The circles with the red dot represent the medians for every spacer while smaller circles without dot are outliers. The thin and thick blue lines show 25 % confidence intervals and 75 %, respectively. The dashed line corresponds to the regression line of all calibration points. The solid line corresponds to the adjusted regression line used for further aperture calculations by neglecting an apparent aperture (0.08 mm) caused by the fracture roughness (after Huo et al. 2016).

Although this strategy does not describe the basic intention of the common MA method, it provides a convenient solution to include data for the entire core and also enables integrations of regions with higher porosity within a homogenous matrix material where fluid inclusions should decrease CT_{mat}.

Hence, voxels representing sections of the matrix with significant porosity should reveal lower CT numbers ($CT_i < CT_{mat}$) so that these voxels, in simplified terms, are treated as equivalent apertures. These equivalent apertures represent the effective hydraulic diameter, which can be applied to characterize tube-like fluid flow in porous media (Debbas and Rumpf 1966), and describes these tubes as rectangular ducts comprising the same area as the tubes (Janna 2010). Since simulating fluid flow does not work only with aperture information, each voxel has to be assigned to a potential hydraulic property. Assuming laminar flow and that fluid flow within the core is mainly controlled by fracture properties, the "cubic law" approach (Boussinesq 1868; Snow 1965) is chosen to derive appropriate local permeabilities (K_{MA}) based on the MSMA aperture calibration, which is defined as

$$K_{MA} = \frac{a^2}{12} \tag{3.4}$$

3.2.4 Simulation

Fluid flow within the processed CT scan image is simulated using the FlowDict module of the multidisciplinary commercial GeoDict® program package (Math2Market, Kaiserslautern, Germany), which has been developed to predict (microstructure-based) physical material properties (Pfrang et al. 2007). In the past, GeoDict was successfully applied to several studies with geoscientific background concerning fluid flow or particle tracking in fractured as well as porous media (Khan et al. 2012; Schwarz and Enzmann 2013; Pudlo et al. 2014; Leu et al. 2014; Rücker et al. 2015). The utilization of the FlowDict module is based on three basic prerequisites: (1) a 3-D voxel-based image of a permeable object, (2) experimental parameters such as mass flow and flow direction and (3) an incompressible Newtonian fluid. Indeed, the used fluid (N_2) is actually a compressible fluid but can be treated as an incompressible fluid due to experimental boundary conditions (e.g., pore pressure, flow rates) as mentioned earlier. FlowDict only supports two simulation types: predicting the mean fluid velocity based on pressure drop boundary conditions and vice versa. Afterwards, entire sample permeability can be derived by applying Darcy's law (only for considering laminar flow).

In this study, fluid flow simulations are based on an explicit finite-volume method that solves the Navier–Stokes–Brinkman equation according to Iliev and Laptev (2004). The governing equation comprises both incompressible isothermal flow in pure fluid regions represented by the Navier–Stokes equation and flow in solid (matrix) regions defined by hydraulic properties represented by the Brinkman extension of Darcy's law (Iliev and Laptev 2004):

$$\underbrace{-\mu\Delta\,\boldsymbol{u} + (\rho\boldsymbol{u}\cdot\nabla)\boldsymbol{u}}_{Navier-Stokes} + \overbrace{\underbrace{\mu K_x^{-1}\cdot\boldsymbol{u} + \nabla P = 0}}^{Darcy's\ law} \tag{3.5}$$

$$\nabla\cdot\boldsymbol{u} = 0 \tag{3.6}$$

where μ is the fluid viscosity, ρ the fluid density, P represents fluid pressure and $\boldsymbol{u}$ is the 3-D velocity vector. Furthermore, the reciprocal local permeability K_x^{-1} represents locally assigned permeability based on the aperture calibration (x = MA), in voxels representing the solid matrix (x = solid) and further materials such as filter materials (x = filter). Equation (3.5) outlines the momentum conservation which contains viscous forces, an advective acceleration term, the Brinkman extension to Darcy's law and the applied pressure gradient. Concurrently, the continuity equation (Eq. 3.6) describing the conservation of mass has to be valid. In order to solve the pressure–velocity relationship, a guess-and-correct procedure represented by the Semi-Implicit Method for Pressure-Linked Equation (SIMPLE) algorithm (Patankar and Spalding 1972) is implemented.

Fluid flow is simulated parallel to the core axis for nitrogen at 50 °C with respective values for density (1.2 kg m^{-3}) and viscosity (1.9×10^{-5} Ns m^{-2}). The simulations compute the velocity field for the given pressure drop using periodic boundary conditions on the computational box and Dirichlet boundary conditions for the pressure. Pressure drops for each stage of σ' are arbitrarily defined by measured values obtained for a flow rate of 16 mL min^{-1}. K_{solid} (5.92×10^{-19} m^2) were obtained by MICP analysis (Sect. 2.1). In addition, in order to stabilize the simulation and to provide homogeneous in-/outflow as experimentally accomplished by filter plates, two artificial filter plates with $K_{filter} = 1 \times 10^{-10}$ m² are attached to the inlet and outlet according to the experimental setup (cf. Fig. 3.3). Indeed, hydraulic properties of these filter plates are also included into flow simulations and associated permeability calculations; however, affectations can be assumed to be negligible due to the proportionally small extent of the filter plates (194 × 194 × 5 voxels) compared to the sample dimensions (194 × 194 × 258 voxels).

Simulations are terminated by either reaching the accuracy criterion (ratio of current to former calculated permeability during iteration) of 1.5×10^{-4} or exceeding 10^6 iterations. Simulations are performed with a high-performance computer containing four Interlagos processors (64 cores) with 512 GB of total RAM. Dependent on available capacity (24 or 48 cores in this study) and aperture calibration, computation time of a single simulation ranges between 2 and 4 h.

3.3 Results and discussion

3.3.1 Simulation

In this section, only the results of the simulations are discussed. For more detailed discussion and analysis on the experimental results, which particularly emphasize the hydraulic and geometric properties of the fracture as well as the applicability of empirical models, we refer to Huo and Benson (2015). However, some of their findings are discussed in the context of the quantitative and qualitative simulation results presented in this study.

Qualitative results mainly highlight the visualization of fluid flow simulations that can be used for flow path analysis. In contrast, quantitative results refer to fluid volumes for the different stress stages that can be directly validated by corresponding core-flooding experiments and are compared to the effectiveness of other simulation approaches.

Visualizations of all simulation results indicate that principal fluid flow in the core is governed by a few preferential flow channels along the fracture plane that are partially interconnected (Fig. 3.5). Differentiating fluid flow simulations for single stresses shows the expected stepwise closure of the fracture and containing channels. This becomes clear for considering changes in local fluid flow with changes in effective stress. Applying loading conditions indicates a significant decrease in connectivity and local permeabilities within most parts of the fracture. In reverse, the same is observed for unloading conditions. This behavior is in line with an increasing (decreasing) percentage of contact areas and an increase (decrease) of smaller apertures due to loading (unloading) presented by Huo and Benson (2015). Furthermore, applying unloading conditions includes the re-increase of connectivity and permeability due to the opening of several channels and branches. However, some channels and especially branches remain closed or disconnected as a result of irreversible deformation (Fig. 3.5). Hence, it can be assumed that changes in fracture connectivity can be directly related to the strength of the present asperities (Pippan and Gumbsch 2010; Huo and Benson 2015). Accordingly, plastic deformation and brittle failures along asperity tips cause irreversible changes that are associated with the permanent local closings and constrictions as also depicted by Fig. 3.5. Elastic deformation can be assumed to be most widely reversible and facilitates local reopenings.

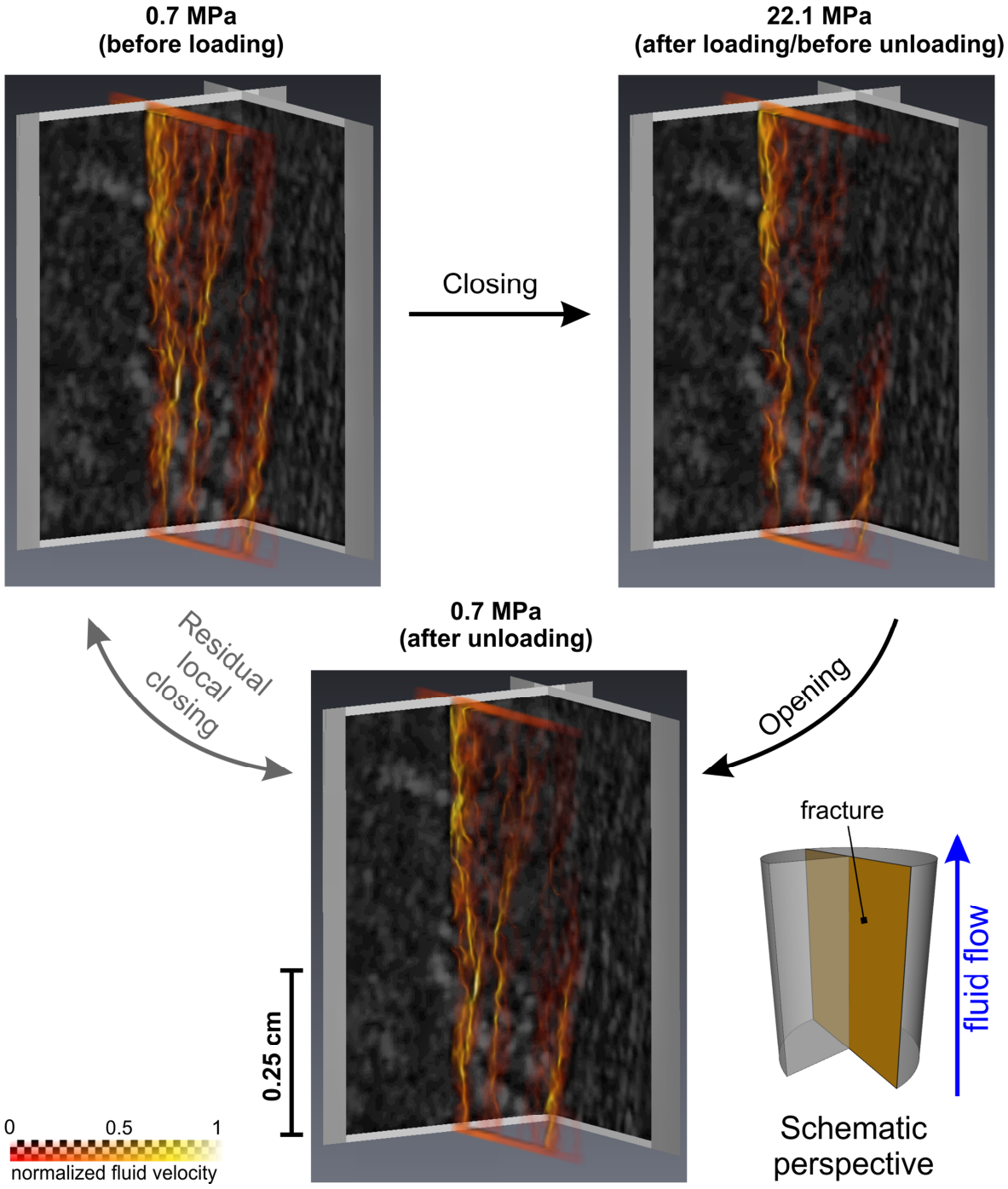

Fig. 3.5: Changes in 3-D fluid flow only along the fracture plane due to closing during loading conditions (from 0.7 to 22.1 MPa) and due to reopening caused by unloading conditions (from 22.1 to 0.7 MPa) by applying forward modeling with an explicit finite volume method solving the Navier–Stokes–Brinkman equation. Fluid flow is visualized by fluid velocity per voxel normalized by the maximum fluid velocity at the given pressure stage. Fluid velocity increases from red to yellow. Velocity fields of the initial and residual pressure stage (0.7 MPa) indicate permanent local closings along the fracture. A schematic perspective is included for better 3-D orientation.

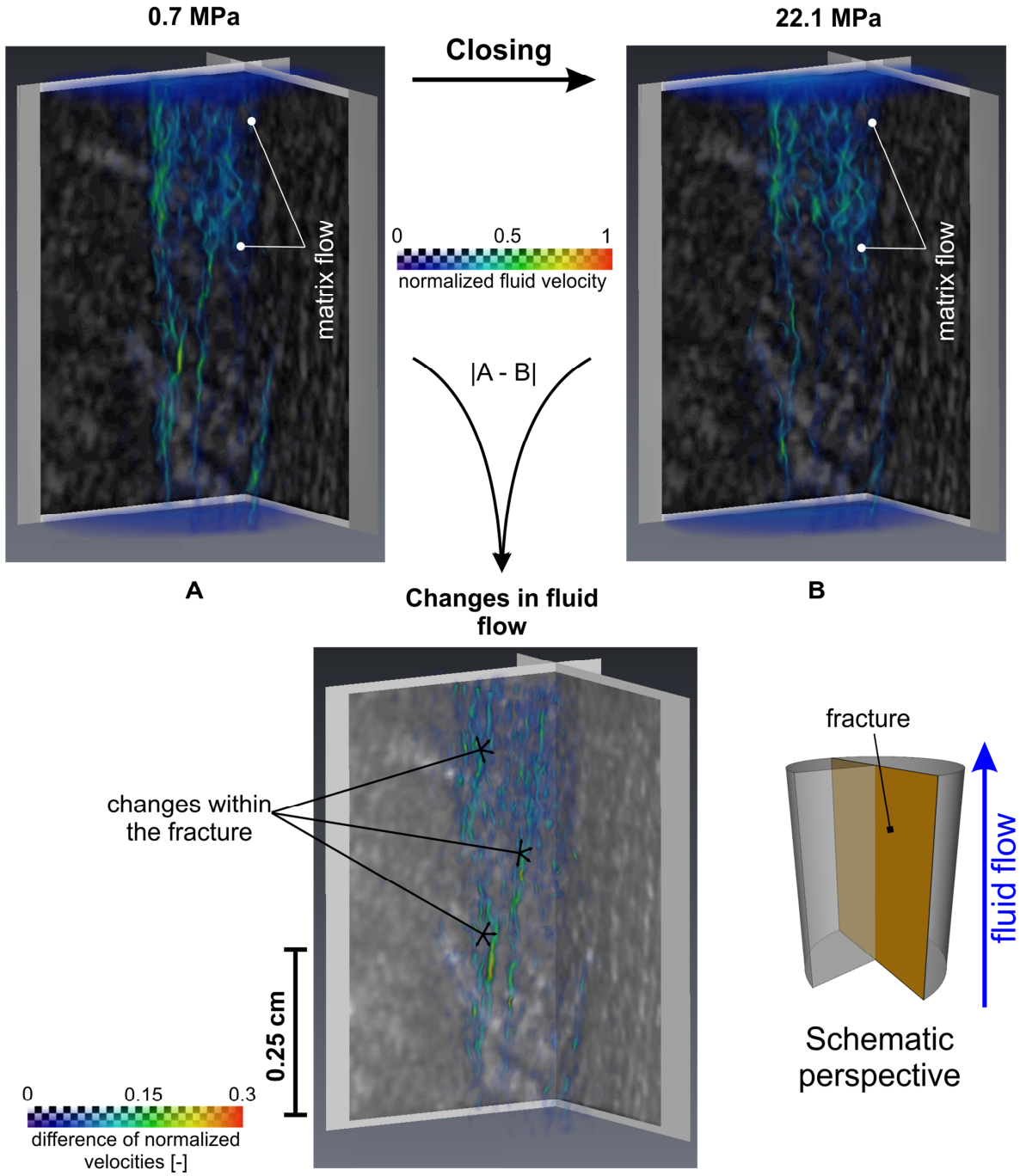

Fig. 3.6: Changes in 3-D fluid flow sample due to closing (A and B) during loading conditions (from 0.7 to 22.1 MPa) by applying forward modeling with an explicit finite volume method to solve Navier–Stokes–Brinkman. Flow visualizations comprise fracture as well as matrix flow. Fluid flow is visualized by fluid velocity per voxel normalized by the maximum fluid velocity at the given pressure stage. Fluid velocity increases from purple to red. Absolute changes in fluid flow (|A-B|) are shown in the lower part. Most changes occur within the fracture. Absolute changes increase from purple to red. A schematic perspective is included for better 3-D orientation.

Furthermore, additionally enhanced fluid flow is observed in single parts within the matrix (Fig. 3.6). Comparing with the CT image (Fig. 3.6) indicates that this flow occurs along laminations containing darker matrix voxels with $CT_i < CT_{mat}$ according to Eq. (3.3). In homogeneous media CT_{mat} simply should represent the predominant mineral phase. In fact, the rather heterogeneous sandstone in this study is dominated by quartz (detrital grains and cement) but is also enriched in feldspar. This feldspar component predominantly consists of plagioclase with minor alkali feldspars (Weissbrod and Sneh 2002). Although there are compositional differences, quartz and plagioclase typically reveal similar and, compared to most other minerals, relatively low CT_i values (Ketcham 2005; Tsuchiyama et al. 2005). Thus, the assumed CT_{mat} (1862.6 HU) most widely can be ascribed to these dominant mineral phases. Hence, regions with significantly lower CT_i values are caused by significant porous regions. This porosity heterogeneity is also observed in thin sections (Huo and Benson 2015; Huo et al. 2016). Nevertheless, the simulated overall matrix permeability can be assumed to be rather low, which is also clarified by carefully examining the propagation of the pressure fields corresponding to the predefined bulk matrix permeability of 10^{-19} m². Concurrently, propagation of the pressure fields also reinforces the assumption that major fluid flow occurs along the fracture. Furthermore, comparing absolute changes in fluid flow (Fig. 3.6) due to loading between the lowest (0.7 MPa) and the highest (22.1 MPa) pressure stage indicates that most changes within the sample occur along the fracture plane while the simulated matrix flow remains nearly equal. Unfortunately, core permeability is derived by solving the Navier–Stokes–Brinkman equation for the measured pressure drop over the entire sample (as stated in Sect. 2.4), which prevents the quantification of the matrix permeability. Due to the missing appropriate validation experiments and the negligible matrix flow, possible fracture–matrix interaction is not further discussed in this study and can be considered as uninfluential artifacts of the matrix material. Nevertheless, the MSMA method can provide a promising approach to simulate such issues, especially considering laminated sandstones, which were experimentally investigated in the past (Clavaud et al. 2008; Karpyn et al. 2009; Grader et al. 2013). Indeed, this method can be erroneous for heterogeneous rocks such as granite, but Watanabe et al. (2011) found that affectations of locally resulting non-real apertures in the matrix are marginal.

In contrast to qualitative analysis, quantitative results of the simulation significantly differ from expected results (Fig. 3.7a). Although there are significant deviations, quantitative results exhibit several characteristics also observed in the experiment (Huo and Benson 2015) such as (weakened) hysteretic behavior, discernible decreases of permeability with increasing pressure and subsequent reactivation of fluid paths under unloading conditions. A first simple (straightforward) simulation is based on an aperture calibration that applies a global CT number for the matrix material (CT_{mat} = 1862.6 HU) as introduced in Sect. 2.3. Additionally, two further simulations are based on modified CT_{mat} values. For the latter, the standard deviation of the voxels is considered. Commonly, image

quality of CT scans can be affected by random noise caused by imprecisions during CT image reconstruction (Pini et al. 2012; Huo et al. 2016) or by the reduction of X-ray intensity due to the presence of metal filters to reduce beam hardening (Ketcham and Carlson 2001; Watanabe et al. 2011; Nakashima and Nakano 2014). As a result of the induced noise, Huo et al. (2016) ascertained a mean standard deviation of ±17.7 HU for each of the voxels. Thus, two "worst-case" scenarios are considered by implementing the terms CTmat ±17.7 HU as input parameters for model calibration of these scenarios to account for uncertainties in CT_{mat}.

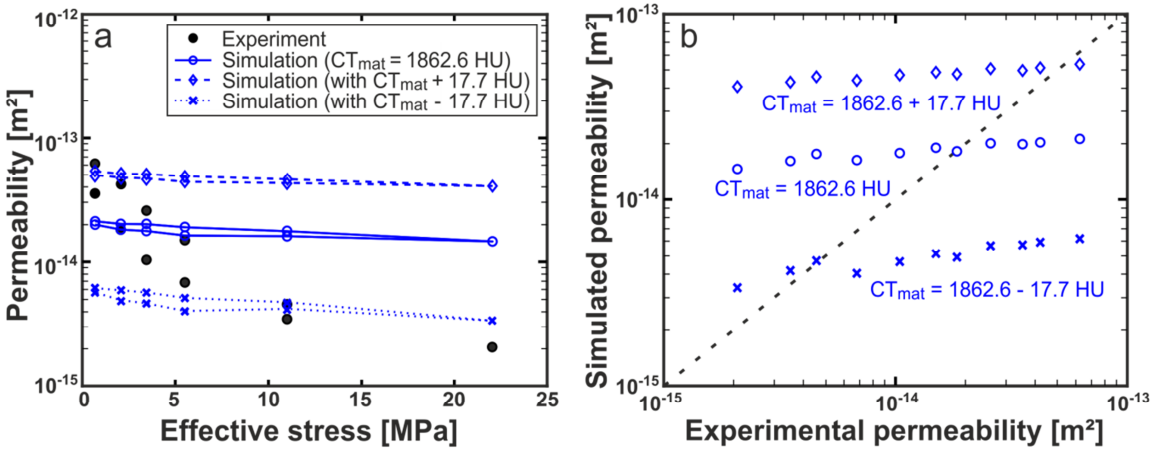

Fig. 3.7: (a) Measured and simulated permeabilities of the entire core sample versus effective stress. Simulation results are obtained by forward modeling (cf. Eq. 3.3) and by changing CTmat according to the mean standard deviation of the CT measurements (cf. Eq. 3.7) and (b) corresponding deviations between experimental and simulated permeabilities indicating a systematic error.

Considering the simple modeling approach, the simulated permeabilities are in the range of minimum and maximum measured permeabilities. However, the permeabilities are clearly underestimated (up to a factor of 0.3) at lower σ' and significantly overestimated (up to a factor of 7.1) at higher σ'. As a result, slopes of the stress-dependent permeability curve diminishes for lower σ' under loading as well as unloading conditions, which consequently contributes to a declined hysteresis area compared to experimental results. This reduction of hysteresis area indicates that intensity of fracture closing derived from CT images appears to be depressed. Possible explanations for this observation are discussed hereinafter.

Comparing the deviation between predicted and observed results indicates that there appears to be a systematic error affecting the simulation results (Fig. 3.7b). Of course, this could be caused by uncertainties of the pressure drop measurements during the experiment. However, permeabilities calculated by considering pressure drop uncertainties indicate deviation by a maximum factor of 1.2

and a minimum factor of 0.9 at the lowest loading stage (Huo and Benson 2015). Most factors of other pressure stages are about 1.0 so that this uncertainty seems to be negligible. Counterchecking of the model input data and boundary conditions showed that the error of the simulation mainly relies on the aperture calibration. For that reason, we tested the sensitivity of the simulation focusing constants (slope and CT_{mat}) and shape of the calibration line.

Varying the slope (5980.2 HU mm^{-1}, according to Eq. 3.3) between ±1 and 5 % hardly reveals any effect on the hysteresis except a very slight shift along the ordinate. This should be explained by very low apertures within the fracture, as represented by mean apertures between 0.025 and 0.031 mm as shown by Huo and Benson (2015), so that changes within the slope hardly affect apertures at the considered scale.

Furthermore, in order to be valid and as introduced in Sect. 2.3, the MSMA method requires a linearity of the calibration line as reinforced by a careful calibration according to Huo et al. (2016) who also physically derived the linear relationship which justifies the extrapolation of apertures as performed here.

An additional factor that can contribute a major part to the simulated deviations is represented by CT_{mat} describing an averaged threshold value for the matrix material. Being apparent from Fig. 3.3, there are significant material heterogeneities within the sample. While darker voxels (with $CT_i < CT_{mat}$) can be assumed to contain more porous regions as discussed above, there are also significant brighter voxels (with $CT_i > CT_{mat}$). These significantly higher CT (partially $CT_i > 1900$ HU) values can be ascribed to the local accumulation of alkali feldspars, typically revealing much higher CT values (up to 100 HU) than quartz due to the high attenuation of potassium (Ikeda et al. 2000). Thus, locally present alkali feldspar in a voxel can cause a local underestimation or even closing of the calibrated local aperture according to Eq. (3.3), most likely making a significant contribution to the underestimation of permeabilities at lower pressures (cf. Fig. 3.7a).

Additionally, this local underestimation can be reinforced by an inappropriate choice of the threshold value CT_{mat}, which also implies some uncertainties. Hence, we focus here on the sensitivity of the simulations caused by uncertainties in CT_{mat}. Thus, CT_{mat} is varied by the uncertainties provided by random noise by including the averaged standard deviation (±17.7 HU). Adding the standard deviation (+17.7 HU) to CT_{mat} indicates that simulated results at lower σ' are shifted towards the experimental data while results at higher σ' significantly overestimate the measurements. The opposite happens for CT_{mat} −17.7 HU, where simulations rather approximate measurements at higher σ' and strongly under estimate measurements at lower σ'. According to Eq. (3.3) and Fig. 3.4 this is obvious since a higher CT_{mat} causes the calibration of larger apertures and, therefore, partially opens new flow channels by

ascribing apertures that are zero for non-adjusted CT_{mat}. Vice versa, non-adjusted channels are constricted or closed by slightly tighter apertures applying a lower CT_{mat}. Hence, the simulation results are highly sensitive to changes in CT_{mat}. Modifying CT_{mat} just by +17.7 HU increases simulated permeabilities up to a mean factor of 2.6 ±0.1. In contrast, reducing CT_{mat} by −17.7 HU diminishes simulation results up to a mean factor of 0.3 ±0.02. Hence, the simulated results that contain the standard deviation of the CT scan are able to cover the full range of experimental values. However, the latter also clearly demonstrate that the used simulation is unable to explicitly reproduce the measured permeability hysteresis. Indeed, the simulations can be fitted by varying CT_{mat} within the mentioned range but the compression and resulting strain on the fine-grained sample as well as the evaluation of the single images do not endorse such a proposal.

A further reasonable explanation for the deviations of the simple simulation approach (with CT_{mat} = 1862.6 HU) from the experimental hysteresis is the presence of potential sub-grid-scale features. This means that variations in the fracture topography most likely are significantly below the CT resolution ($0.5 \times 0.5 \times 1.0$ mm³) so that the actual roughness cannot be captured accurately. Thus, in addition to compositionally caused underestimation of local apertures, the resolution-caused generalization of these features per voxel underestimates experimental permeabilities at lower stresses due to a reduction in actual (sub-grid-scale) connectivity. While at higher stresses the permeability is overestimated by suggesting generalized flow paths. Actually, it can be assumed that there is a significant amount of contact areas within the single voxels causing sub-scale inhibition of fluid flow or connectivity. Therefore, the transferred fracture roughness represents only an approximation of a finer and more complex flow pattern within the smooth fracture where connectivity and tortuosity can be assumed to play a more significant role.

3.3.2 Comparison

As stated above (Table 3.1), several authors have published stress-dependent fluid flow studies based on variously derived fracture geometries and numerical approaches. Until now, medical CT data and, thus, most untreated input data were solely applied by Watanabe et al. (2011; 2013). In their first study (Watanabe et al. 2011), the authors used an aluminum core holder for core-flooding experiments on tensile single-fractured (SF for single fracture) and naturally double-fractured (MF for multiple fractures) granites. In Fig. 3.8a simulated permeabilities resulting from their approach are compared to the results of this study (only loading conditions are shown). As one might expect, measured permeabilities of the four core-flooding experiments decrease with increasing σ'. Although both rock types, Zenifim sandstone and granite, reveal similar matrix permeabilities (10^{-18} to 10^{-19} m²), fluid flow experiments with the fractured sandstone obtain higher permeabilities (between 10^{-14} and 10^{-15} m²) than

granite experiments (between 10^{-15} and 10^{-17} m²). Typically, mean apertures of mated tensile fractures in Inada granite should decrease from 0.071 to 0.065 mm, applying loading from 10 to 100 MPa (Watanabe et al. 2008). Mean apertures of the sandstone sample are significantly lower and range between 0.031 and 0.024 mm (Huo and Benson 2015). Nevertheless, with increasing stresses, hydraulic apertures of the granite fracture decrease from 0.009 to 0.003 mm (Watanabe et al. 2008) while hydraulic apertures of the sandstone fracture decrease from approximately 0.030 to 0.005 mm (Huo and Benson 2015). These significant hydraulic differences of the samples appear to be caused by higher tortuosity as described by Tsang (1984) due to a higher roughness of the tensile granite fractures as compared with the smooth sandstone fracture. In addition, this dependency between fluid flow and tortuosity is reinforced by considering CFD-based flow visualizations of the granite sample, indicating a highly tortuous network of flow channels along the fracture (Watanabe et al. 2011).

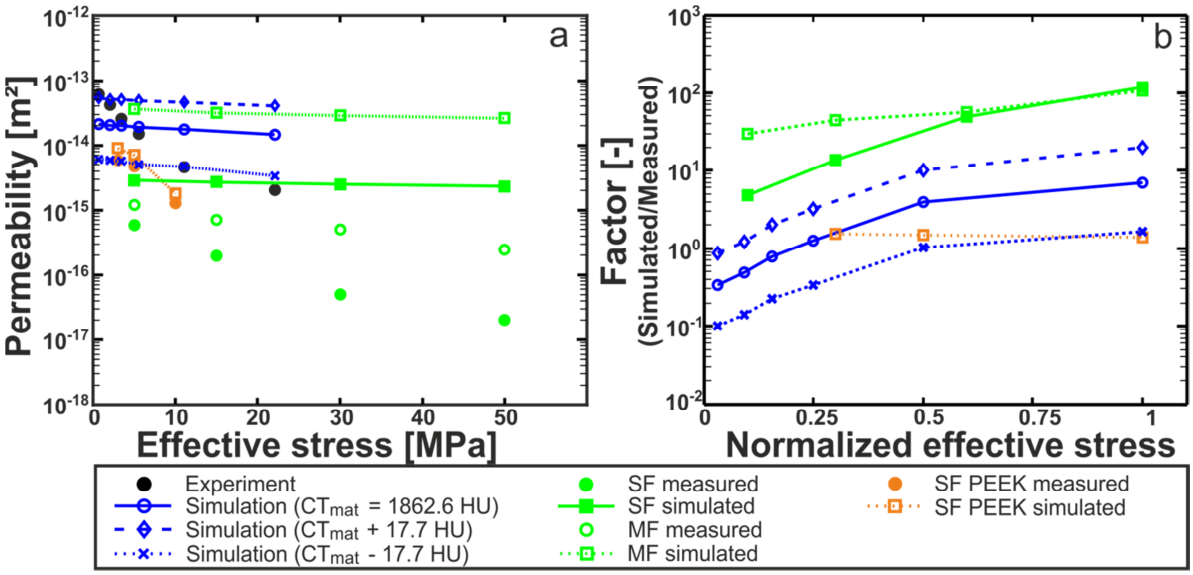

Fig. 3.8: Comparison of experimental and simulated data of the sandstone sample with results obtained from the literature using CT technology to realize simulations (Watanabe et al., 2011, 2013). Literature data are based on a three granite core samples with a single tensile fracture (SF), multiple, natural fractures (MF) and a single tensile fracture measured by using an improved core holder (SF PEEK). Furthermore, the effectiveness of the simulations is shown in (b) as factors, describing the discrepancy between each simulated and corresponding experimental permeability value, versus the normalized effective stresses depending on the highest stress stage applied during the associated experiment.

In order to clarify the effectiveness of the compared simulation approaches, discrepancies between simulated and experimental permeabilities of each sample are plotted as factors against the normalized effective stress in Fig. 3.8a. It can be seen that simulated permeabilities of the SF sample are 5 (at 5 MPa) to 116 times (at 50 MPa) higher than predicted by the experimental data, while simulations based on the MF sample overestimate experimental results by a factor of 30 (at 5 MPa) and 106 (at 50 MPa).

Overestimations are supposed to be primarily caused by image noise due to the core holder causing "non-zero apertures" and, in consequence, extended flow paths within the fracture and the matrix (Watanabe et al. 2011). Considering the three simulation scenarios conducted within the scope of this study, experimental permeabilities are over- or underestimated ranging between a minimum factor of 0.1 and a maximum factor of 20. Considering only the simple simulation approach (with CT_{mat} = 1862.6 HU) numerical results show a maximum overestimation by a factor of 7.1 and a minimum underestimation by a factor of 0.3. Accordingly, the MSMA method appears to reveal slightly better simulation results than Watanabe et al. (2011), although the considered fracture is significantly smaller which indicates an effective noise reduction by applying multiple scans. However, in a subsequent study Watanabe et al. (2013) improved their approach (Fig. 3.8a) with an adjusted experimental setup on a granite containing a single tensile fracture (SF PEEK) by using a carbon fiber reinforced polyether ether ketone (CFR PEEK) core holder. Applying the PEEK core holder significantly reduced the image noise and revealed nearly concurrent experimental and simulated results.

Accordingly, the introduced MSMA method represents a further approximating step for successful CFD simulations but also exposes current limitations. Although applying the method with a global CT_{mat} affirm a loss in accuracy as predicted by Keller (1997) for smooth fractures (< 35 µm), simulation results still are valuable to approximate actual permeabilities in such fractures. Indeed, compositional heterogeneities provide inaccuracies as also predicted by Keller (1997) but are not so dominant that they cause a complete loss of information, as indicated by the kinematics of several reproducible flow channels. Nevertheless, inaccuracy is provided not only by compositional heterogeneities but also by sub-grid-scale features, particularly regarding higher confining pressure and, thus, closing local apertures.

Focussing on our own experiences and including the pioneering research by Watanabe et al. (2011; 2013), we provide the following recommendations for future medical CT-based fracture flow studies:

- The determination of more detailed pore data of the matrix, especially when considering heterogeneous porous rocks, is done by introducing additional MICP measurements and technologies such as micro-CT, environmental scanning electron microscopy (ESEM) or nuclear magnetic resonance (NMR) spectrometry. Additionally, an upscaling of micro-CT data to core scale and coupling this matrix with a medical CT-based aperture distribution of the fracture would provide more realistic pore-geometry data for simulating fracture–matrix flow interaction.

- Before fracture flow experiments start, some "blank tests" should be considered. Core-flooding experiments of the unfractured core sample can provide additional information about the actual

hydraulic properties of the matrix. Furthermore, scans of the unstressed fractured sample with a PEEK core holder (to reduce the beam hardening effect) can be used to detect image noise, which is caused by the metal core holder used in common core-flooding experiments as presented by Watanabe et al. (2013). In this study, image noise cannot be explicitly assigned to the core holder and is most widely due to the imperfections of the CT image reconstruction as also stated for equivalent experimental setups (Pini et al. 2012; Huo et al. 2016). However, an additional affectation due to the core holder cannot be excluded so that a "blank test" would be very beneficial. Since both mentioned noise sources create random noise in the CT image both quality improvement methods, the PEEK core holder and the multiple scan method, should be tested for their effectiveness. Ideally, both methods should be combined to diminish affectations of both possible noise sources. However, PEEK core holder technology was only successfully applied for maximum confining pressure between 36 and 50 MPa at room temperatures (23 °C; Ito et al. 2013; Watanabe et al. 2013) and, thus, is a useful option for experiments focussing on similar conditions. Typically, the strength of PEEK strongly depends on temperature (Searle and Pfeiffer 1985) and the chemical composition of the fluid used for the experiment (Pritchard 1994) and, thus, appears to be challenging for experiments that simulate reservoir conditions or processes in the deeper Earth's crust. Additionally, this study is based on low voxel resolutions ($0.5 \times 0.5 \times 1.0$ mm³) generalizing the area, which is covered by the voxel, to a single aperture value. Thus, high-resolution fracture measurements such as laser-scanning or profilometer measurements should be helpful to detect the effect of generalized fracture morphologies within the voxel scale by comparison with unstressed "blank test" data.

- Typically the common MA method is used to determine apertures only perpendicular to the fracture plane, rather favoring 2-D aperture distributions. Despite that, the MSMA indicates a good transferability of present apertures to a 3-D problem favored by the tightness of the studied fracture with mean apertures between 0.031 and 0.024 mm, where the fracture-caused anomaly predominantly affects the voxel containing the fracture. However, with increasing fracture width it becomes more likely that the anomaly also affects adjacent voxels and the aperture calibration becomes invalid. Thus, the applicability of the introduced method should be validated for additional scenarios: (1) for different fracture widths where apertures must be smaller than the x−y resolution of the CT scan; (2) for different fracture types such as smooth and rough fractures or tensile and shear fractures; (3) for different materials highlighting the influence of different heterogeneities caused by the mineralogical composition or porosity; (4) for different applicable x−y resolutions provided by medical CT scanners (e.g., 0.2×0.2 or 0.3×0.3 mm²). However, most of the suggested scenarios depend on each other and should be

critically considered. In addition, a similar procedure is recommended for the PH method used by Watanabe et al. (2011) to underline the scope of applications and limitations of both methods.

- In this study, aperture calibration is based on the general assumption of a linear relationship between MA and aperture width (e.g. Keller 1997; Bertels et al. 2001; Van Geet and Swennen 2001) and, thus, on a crude spacer calibration (with four spacers ≥ 0.2 mm). However, Mazumder et al. (2006) found a significant nonlinear relationship by applying an optimized MA approach to minimize affectations due to heterogeneities of their coal sample. They found that the slope of the line significantly increases with decreasing apertures (< 0.25 mm). Therefore, future studies should focus on a more accurate spacer calibration, particularly with spacers < 0.1 mm, which corresponds to many apertures under confining pressure.

- In order to validate qualitative fluid flow, new contrast agents should be introduced. Conventionally used iodine was shown to cause beam hardening effects that exacerbate the interpretation of flow paths within the fracture (Watanabe et al. 2011). Meanwhile, sodium polytungstate $Na_6H_2W_{12}O_4$) was proposed as a promising contrast agent for hydrological CT experiments by significantly reducing the undesirable beam hardening effect (Nakashima 2013; Nakashima and Nakano 2014). Alternatively, further technologies such as positron emission tomography could be applied (Kulenkampff et al. 2008; Fernø et al. 2015).

3.4 Conclusions

An alternative method to simulate fluid flow in a fractured porous core sample under loading and unloading conditions based on medical CT measurements was introduced. Simulation results reveal qualitative plausibility but also reveal shortcomings considering quantitative results. Generally, the proposed method is able to approximate experimentally derived permeability data even in smooth fractures (< 35 µm); however, it merely indicates the stress dependency of fracture permeability.

Qualitative results reveal satisfactory accordance with the well-established flow channeling approach, indicating that major flow is governed by several preferential flow paths along the fracture with less pronounced tortuosity. The simulations reproduce temporal and permanent closing of some flow channels due to increasing effective stress, causing significant changes in connectivity and associated permeability.

Despite the quantitative deviations, the simulated permeabilities indicate stress dependency of the sample represented by a slight decrease in permeability with increasing effective stress and even imply hysteretic behavior. Besides minor calibration errors, the deviations are mainly caused by

compositional heterogeneities of the matrix material and resolution-caused limitations. The former facilitates underestimation of local hydraulic properties, while the latter prevents an accurate capturing of sub-grid-scale features. Both error sources affect the reproduction of actual connectivity playing an important role in smooth fractures. Furthermore, the simulation is very sensitive to the choice of an adequate threshold value CT_{mat} (1862.6 HU in this study). Small deviations from the ideal CT_{mat} (±17.7 HU in this study) can cause enormous changes in simulated permeability by up to a factor of 2.6 ± 0.1. Thus, CT_{mat} has to be defined with caution and can cause additional problems for rocks with significant mineralogical heterogeneities.

Nevertheless, the comparison with an analogous CT-based CFD study by Watanabe et al. (2011) reveals that the introduced MSMA approach can be a valuable method to analyze quantitative and qualitative fracture flow. Considering the aforementioned comparative study a list of recommendations for future research is compiled, including a systematic investigation concerning different experimental and model setups, rock types, fracture modes as well as validation techniques.

Acknowledgement

This study was mainly carried out within the framework of the Helmholtz Association of German Research Centres (HGF) portfolio project ‘Geoenergy’ and is part of the comprised reservoir engineering cluster. In addition, we acknowledge the postdoctoral grant to JOS, which was funded within the framework of DGMK (German Society for Petroleum and Coal Science and Technology) research project 718 "Mineral Vein Dynamics Modelling". The latter is funded by the companies ExxonMobil Production Deutschland GmbH, ENGIE E&P Deutschland GmbH, DEA Deutsche Erdoel AG and Wintershall Holding GmbH, within the basic research program of the WEG Wirtschaftsverband Erdöl- und Erdgasgewinnung e.V. The authors also want to thank Rani Calvo from the Geological Survey of Israel for providing the Zenifim sandstone sample used in this study. In particular, we thank Math2Market for providing the GeoDict software package for fluid flow simulations. We acknowledge support by Deutsche Forschungsgemeinschaft and Open Access Publishing Fund of Karlsruhe Institute of Technology. Last but not least, we thank the anonymous referees for their constructive comments and valuable hints.

Chapter 4

Fracture flow due to hydrothermally induced quartz growth

Reproduced from: Kling T, Schwarz J-O, Wendler F, Enzmann F, Blum P (2017): Fracture flow due to hydrothermally induced quartz growth. Advances in Water Resources, 107:93-107, doi:10.1016/j.advwatres.2017.06.011.

Abstract

Mineral precipitations are a common feature and limitation of initially open, permeable rock fractures by forming sealing structures or secondary roughness in open voids. Hence, the objective of this numerical study is the evaluation of hydraulic properties of fractures sealed by hydrothermally induced needle and compact quartz growth. Phase-field models of progressive syntaxial and idiomorphic quartz growth are implemented into a fluid flow simulation solving the Navier–Stokes equation. Flow simulations for both quartz types indicate an obvious correlation between changes in permeability, fracture properties (e.g. aperture, relative roughness and porosity) and crystal growth behavior, which also forms distinct flow paths. Thus, at lower sealing stages initial fracture permeability significantly drops down for the 'needle fracture' forming highly tortuous flow paths, while the 'compact fracture' records a considerably smaller loss. Fluid flow in both sealing fractures most widely is governed by a "parallel plate"-like cubic law behavior. However, the 'needle fracture' also reveals flow characteristics of a porous media. A semi-theoretical equation is introduced that links geometrical (a_m) with hydraulically effective apertures (a_h) and the relative fracture roughness. For this purpose, a geometry factor α is introduced being α = 2.5 for needle quartz and α = 1.0 for compact quartz growth. In contrast to most common a_h-a_m-relationships this novel formulation not only reveals more precise predictions for the needle (RMSE = 1.5) and the compact fractures (RMSE = 3.2), but also exhibit a larger range of validity concerning the roughness of the 'needle' (σ/a_m = 0–2.4) and the 'compact fractures' (σ/a_m = 0–1.8).

.

4.1 Introduction

In the Earth's crust, rock fractures are responsible for the fluid flow and mass transfer. They can be tectonically or anthropogenically (e.g. excavation damage, hydraulic stimulation) induced and contribute decisively to the permeability of rocks as a benefiting or limiting factor depending on the geoscientific matter. While geoscientific applications such as tunnelling or nuclear waste disposal require best possible fluid tightness of the host rock, particularly reservoir engineering projects (e.g. geothermal energy, hydrocarbons or water supply) aim for permeable pathways facilitating high fluid productivity. In general, fluid flow in fractures relies on miscellaneous hydraulic properties (e.g. roughness, tortuosity or connectivity) that most widely are controlled by the geometry of the fracture and its grade of closure (Tsang 1984; Hakami and Larsson 1996). Fracture closure and geometry in turn are closely related to the fracture history, which, especially under subsurface conditions, quite often underlies thermal-hydrological-chemical-mechanical (THCM) couplings. However, to provide reliable THCM models, e.g. to assess formation permeability, a deeper understanding of binary couplings is required. The most important binary couplings concerning single fractures in rocks are HM and HC processes as reviewed by Tsang (1991). In particular, HM processes were extensively studied in the past (Kling et al. 2016; Vogler et al. 2016b), not least because of the straightforwardness of required boundary conditions that are predefined by hydraulic and mechanical fracture properties (Rutqvist and Stephansson 2003), but also due to the availability of several imaging methods as summarized by Huo et al. (2016). In comparison, the description of HC couplings is less investigated due to the complexity of occurring chemical processes.

In general, HC couplings can be caused by physicochemical (Yasuhara et al. 2006; Cohen et al. 2008; Chi and Xue 2011) or biochemical processes such as microbially induced mineral precipitation (De Muynck et al. 2010; Cuthbert et al. 2013; Mountassir et al. 2014). The latter increasingly has become the focus in recent times, especially for engineered applications such as the reconsolidation of building stones (De Muynck et al. 2010) or grouting of contamination pathways (Cuthbert et al. 2013). Nevertheless, the present study solely addresses physicochemically driven fluid-fracture interactions, where hydraulic properties of a fracture typically evolve with time in response to either fracture sealing, wall-rock dissolution or coupled sealing/dissolution processes (Dijk and Berkowitz 1998; Singurindy and Berkowitz 2005; Lang et al. 2015; Pandey et al. 2015). In order to limit the major field of this study merely the influence of pure sealing processes as a limiting factor on fracture permeability is investigated. In this study, the term ‘sealing’ is defined by the ratio of the present solid volume and the initial non-solid (fluid) volume in the interior of an open fracture.

In this context, particularly quartz represents the dominating phase in most hydrothermal fluids and therefore facilitates the precipitation of respective mineral modifications in the case of silica

supersaturation due to mixing, cooling or depressurisation (Fournier 1985). Thus, hydrothermally induced precipitation of quartz in fractures does not only play an important role in the formation of epithermal mineral systems (Dong et al. 1995; Moncada et al. 2012). It also can be a considerable feature when exploiting geothermal energy (Fischer et al. 2003) or hydrocarbons (Laubach 1988; Nelson 2001) from fractured reservoirs, as scaling during the extraction process of fluid within the pipes (Gunnarsson and Arnórsson 2005) or as clogging of permeability when subsequently reinjecting the cooled down fluid in the subsurface (Horne 1982).

When considering progressive quartz sealing in fractures, most permeability models still maintain parallel plate approaches combined with rate law based kinetic models (Lai et al. 1985; Robinson and Pendergrass 1989; Malate and O'Sullivan 1992; Lowell et al. 1993; Pandey et al. 2015). However, mineralization processes inside the inherently rough fractures can cause an additional roughening within the fracture voids, so that actual fracture geometries significantly differ from the supposed parallel plate approach. Typically, there are four types of sealing that are explicitly described by Bons et al. (2012): (1) Antitaxial, (2) unitaxial (unidirectional), (3) syntaxial (or bitaxial/bidirectional) and (4) ataxial (or stretched) growth. The present study only refers to the most prominent sealing process in the Earth's crust (Ankit et al. 2015b): syntaxial sealing, where growing crystals coalesce after starting from both fracture walls of an open fracture.

Experiments studying the relation between hydrothermal conditions and quartz growth in fractures are sparse (Tenthorey et al. 2003; Okamoto et al. 2010; Okamoto and Sekine 2011; Saishu et al. 2014). These experiments provide some indications about quartz textures forming at the given conditions. However, none of them addresses a direct relationship between apparent sealing and permeability reduction. Fortunately, experimental conditions and crystallographic analysis of quartz textures by Okamoto and Sekine (2011) provide sufficient information to reproduce and validate hydrothermal quartz growth by using a three-dimensional phase-field approach (Wendler et al. 2015). Wendler et al. (2015) not only were able to reproduce the quartz textures of the experiment, but subsequently also found indications how silica supersaturation of the simulations affects crystal habits. While higher supersaturations ($S = 3.6$) tend to form compact and contiguous (elongate-blocky) quartz morphologies, lower supersaturations ($S = 1.8$) favor a more isolated growth of rather elongate-slender crystals. In the present study, these respective growth types are termed as compact (for elongate-blocky) and needle (for elongate-slender) quartz. It should be mentioned that the needle quartz described here does not correspond to the classical (crystallographic) acicular habit, but rather represents slender prismatic crystals. Both growth types can be natural sealing features occurring in the Earth's crust. For instance, needle-like quartz textures are found in quartzite fractures of the geothermal exploratory site at Long Valley Caldera (USA), where fractures have a hydrothermal sealing

background (Fischer et al. 2003). Compact quartz textures are common features and most widely described in the context of epithermal mineral deposits (Dong et al. 1995; Christie et al. 2007; Moncada et al. 2012; Shimizu 2014).

Both, compact and needle quartz have in common that the idiomorphic crystals typically require a low degree of silica supersaturation below $S_{max} \approx 3.5–3.7$ (Fournier 1985; Okamoto et al. 2010; Saishu et al. 2014; Shimizu 2014). Typically, silica supersaturations in natural reservoirs are between 1.1 and approximately 10 (Ross et al. 1994; Putnis et al. 1995; Hilgers et al. 2004). Exceeding Smax causes a more rapid nucleation of crystallization seeds so that primarily blocky (microcrystalline) crystals dominate the fracture (Saishu et al. 2014). Unfortunately, only little is known about *in situ* supersaturations and idiomorphic quartz crystal shapes found in naturally sealed fractures. In fact, it is hard to generalize a direct relationship between the amount of supersaturation and crystalizing quartz textures. Quartz crystals growth not only depends on silica supersaturations, but also depends on various other factors such as the amount and nature of further dissolved chemical species (Okamoto et al. 2010), kinematics of the fracture (Ankit et al. 2015b; Lander and Laubach 2015) or the grain size diameter (Wendler et al. 2015) and mineralogy of the host rock (Okamoto and Sekine 2011) resulting in a variety of possible quartz habits and phases in natural fractures (Dong et al. 1995; Bons et al. 2012; Moncada et al. 2012).

According to that, there is a wide range of possible morphologies within sealed or partly sealed fractures that can have an additional effect on the anyway existing inherent roughness of natural fractures. In particular, sealing specific features such as “crystal bridges” (Laubach et al. 2004), intercrystalline porosity (Gale et al. 2010) or the roughness of diverse growth fronts can significantly affect fracture permeability, but are also hard to quantify until now (Nelson 2001). Thus, numerical crystal growth models such as phase-field models (PFMs) can overcome this limitation by delivering realistic developing structures.

Hence, the objective of this study is to examine how different grades of sealing affect fracture permeability, assuming two cases with different crystal growth habits. This numerical study is based on a phase-field model introduced by Wendler et al. (2015) simulating hydrothermally induced three-dimensional growth of needle or compact quartz crystals. Progressive sealing stages are used as input for fluid flow simulations delivering information about intrinsic flow conditions of the different flow patterns. Emphasis is placed on the progressive growth of the two quartz modifications and their global and local influence on fluid flow and hydraulic properties focusing on fracture aperture, porosity and roughness. Empirical models such as the cubic law and the Kozeny–Carman equation are applied to obtain direct relationships between fracture permeability and hydraulic properties especially for partially sealed fractures.

4.2 Methods

4.2.1 Phase-field modeling

In the past, many numerical methods such as purely kinetic front tracking (Bons 2001), cellular automaton models (Lander et al. 2008; Lander and Laubach 2015) or continuum-based reactive transport models (Li et al. 2008) were used to simulate different fracture sealing scenarios. However, recently, phase-field models (PFMs) have become a common tool in material sciences to simulate the evolution of complex geometries such as solidification of melting, grain growth, crack propagation or solid-state sintering (Moelans et al. 2008). In comparison to other simulation approaches, PFMs excel by sophisticated thermodynamic implementations capturing the transition between multiple phases and also enable a three-dimensional depiction of the simulated structures. PFMs focus on the numerical reproduction of mineralization processes in rock fractures at the scale of the mineral crystal grains that consider a physically profound scenario including interface kinetics, thermodynamic driving forces such as the supersaturation of the fluid and the influence of interface energy. Thus, in geosciences, PFMs have been proven to correctly capture the dynamics of crystal growth for various growth scenarios such as single olivine crystals in the Fe-Mg-system (Miura 2013), monomineralic thin-film growth (Hubert et al. 2009; Wendler et al. 2011), uni- and bitaxial crack-sealing processes (Ankit et al. 2013, 2015b) as well as experimentally based syntaxial fracture sealing (Ankit et al. 2015b; Wendler et al. 2015).

The basic ideas behind PFMs is to introduce an additional, smooth indicator field $\phi_\alpha(x,t)$ (the phase field) in the simulation domain that captures the actual position of each phase α (Qin and Bhadeshia 2010). The index α indicates the liquid phase and the differently oriented crystalline phases, so that $\boldsymbol{\phi} = \phi_\alpha(\alpha = 1\ldots N)$ is the set of all existing phases. ϕ_α is defined in the interval [0, 1], and interfaces are given by a steep transition from the exterior ($\phi_\alpha = 0$) to the interior ($\phi_\alpha = 1$) of the phase. The driving force for the crystallization from solution is derived here from a local minimization of the Helmholtz free energy $F(\boldsymbol{\phi}, \boldsymbol{c}, T)$, which additionally depends on the mole fractions $c = c_i$ of all species and the temperature T. Mathematically, the free energy functional can be formulated as the spatial integral of interface and bulk energy contributions over the numerical domain Ω,

$$F = \int_\Omega \left(\left(\varepsilon a(\boldsymbol{\phi}, \nabla\boldsymbol{\phi}) + \frac{1}{\varepsilon} w(\boldsymbol{\phi}) \right) + f(\boldsymbol{\phi}, \boldsymbol{c}, T) \right) dx \tag{4.1}$$

where ε controls the (small) interface width, and $a(\boldsymbol{\phi}, \nabla\boldsymbol{\phi})$ and $w(\boldsymbol{\phi})$ together constitute the interface free energy. The bulk free energy density $f(\boldsymbol{\phi}, \boldsymbol{c}, T)$ considers the thermodynamic stability of solid and

fluid. It is defined as an interpolation of the individual Helmholtz free energy densities of the local coexisting phases, whereas the difference of the free energy between two phases results in a driving force for crystallization.

In Eq. (4.1), the gradient energy $a(\boldsymbol{\phi}, \nabla\boldsymbol{\phi})$ incorporates the anisotropic evolution of the crystal facets in equilibrium, comprising information about the solid-liquid interface tension and the capillary anisotropy. The latter determines the crystal shape under equilibrium conditions, the Wulff shape. The addend $w(\phi) = w(\phi_1,\phi_2,...\phi_N)$ denotes a multidimensional potential-type function, which adds an energy penalty for the interfaces ($0 < \phi_\alpha < 1$) and, hence stabilizes a transition of constant width (Wendler et al., 2015).

The evolution equations for each phase field are derived from Eq. (4.1) by demanding a monotonous decrease of the free energy in time. This means that the rate of change of ϕ_α must be negatively proportional to the variational derivative of F with respect to ϕ_α, giving the following set of N equations (Allen-Cahn equations)

$$\begin{aligned}\varepsilon\frac{\partial\phi_\alpha}{\partial t} &= \omega(\boldsymbol{\phi},\nabla\boldsymbol{\phi})\left(\frac{\partial F}{\partial\phi_\alpha}-\lambda\right)\\ &= \omega(\boldsymbol{\phi},\nabla\boldsymbol{\phi})\left(\varepsilon\left(\nabla*\frac{\partial a(\boldsymbol{\phi},\nabla\boldsymbol{\phi})}{\partial\nabla\phi_\alpha}-\frac{\partial a(\boldsymbol{\phi},\nabla\boldsymbol{\phi})}{\partial\phi_\alpha}\right)-\frac{1}{\varepsilon}\frac{\partial w(\boldsymbol{\phi})}{\partial\phi_\alpha}-\frac{1}{T}\frac{\partial f}{\partial\phi_\alpha}-\lambda\right).\end{aligned} \tag{4.2}$$

Here, a Lagrange multiplier λ establishes the necessary constraint of the volume fractions ϕ_α. The prefactor $\omega(\boldsymbol{\phi}, \nabla\boldsymbol{\phi})$ is an anisotropic kinetic coefficient, which accounts for the lattice-plane dependent difference in attachment kinetics of quartz and, thus represents the orientation dependency of growth rates. The kinetic coefficient of the solid-liquid transition was adapted to previous dissolution experiments for the system under consideration (Okamoto et al. 2010).

In general, the phase field Eq. (4.2) is numerically solved together with a diffusion-advection equation for the silica concentration, which induces a bidirectional coupling to the Navier-Stokes equation for fluid flow. Thus, this results in the formulation of a microscale reactive transport model, where the shape of the growing crystals is governed by the superposed effect of the anisotropy of kinetics and surface energy (Sekerka 2005) as well as basic chemical kinetics. Within the scope of this study, formerly simulated structures for syntaxial quartz growth of needle as well as compact crystal habits are adopted from (Wendler et al. 2015) by applying identical input parameters. The authors and references herein present a detailed review of the applied PFM.

Nevertheless, it was found that under the given supersaturation and flow conditions the effect of silica depletion in the fluid is very small, so that we can omit the concentration equation and assume a constant supersaturation (Wendler et al. 2015). Hence, in this study we apply a unidirectional coupling where crystal growth effects the flow field, not vice versa.

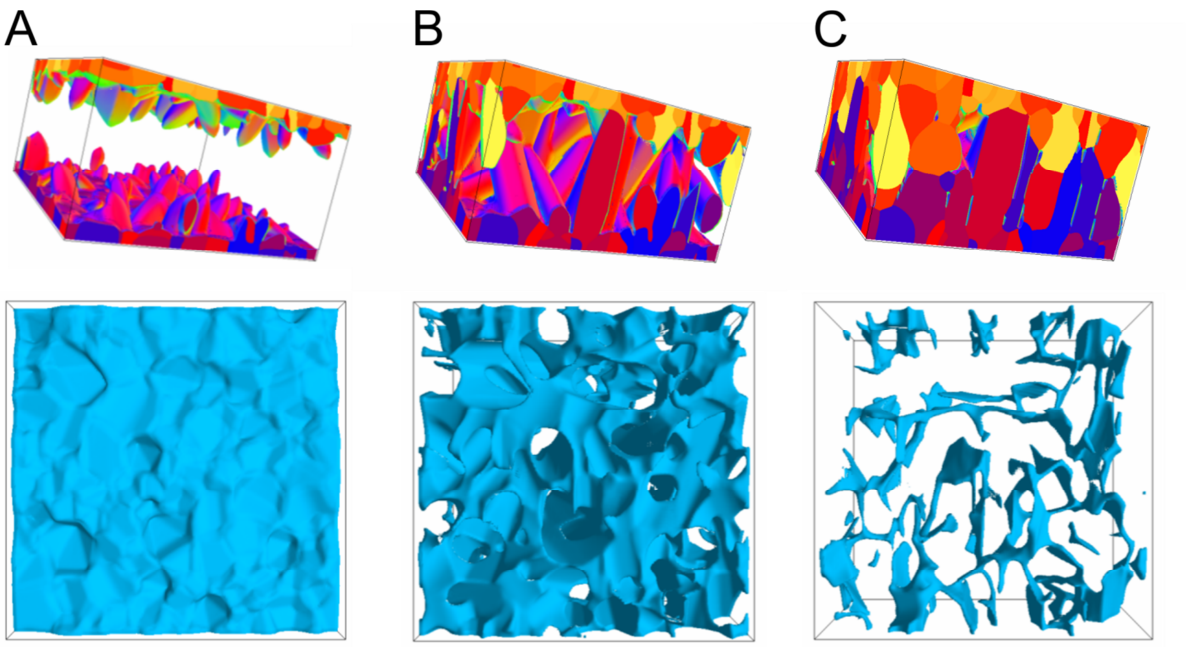

Fig. 4.1: Upper panel: phase-field model (PFM) of needle quartz sealing of a planar fracture with 300 grains. Initial aperture was 80 µm with average grain size 7 µm. Lower panel: top view on the evolving 3D liquid surface filling the fracture at time steps according to upper panel. (A) Needle quartz growth creates rough surfaces (~7% sealing). (B) Development of crystal bridges that are visible as holes (~13% sealing). (C) At the final stage, porosity decreases down to 1.5% and pore channels are formed (~95% sealing).

Wendler et al. (2015) calibrate and validate the adapted model by incorporating hydrothermal flow-through experiments mimicking sealing of artificial sandstone and metachert fractures (Okamoto and Sekine 2011). Hence, boundary and fluid conditions (with a silica supersaturation of S = 3.6), except the initial fracture widths, are equivalent to the validation study by Wendler et al. (2015). However, differences in simulated crystal habits that are a consequence of different seed crystal sizes also imply differences in crystal sizes so that compact quartz tends to be more voluminous than needle quartz. Thus, in order to obtain representative fracture sealing where progressive fluid flow behavior should be governed by crystallization induced roughness, the initial planar fracture for needle quartz growth (grid resolution $150 \times 150 \times 80$, voxel dimension 13 μm^3) is smaller than for compact quartz (grid resolution $300 \times 300 \times 160$ μm^3, voxel dimension 23 μm^3). Each fracture surface contains the same number of

initial quartz ‘seeds’ (150 grains) mimicking a quartziferous rock with respective mean diameters of 7 µm (for needle quartz) and 55 µm (for compact quartz).

4.2.2 Computational fluid dynamics

Computational fluid dynamics (CFD) are used to solve and analyse potential fluid flow behavior in the sealing fractures. The qualitative results of the simulations for needle and compact quartz are exemplarily illustrated in Fig. 4.2, where fluid enters at the visible left plane and enters at the opposite side. CFD simulations are performed for different stages of sealing based on the fracture geometries provided by PFM.

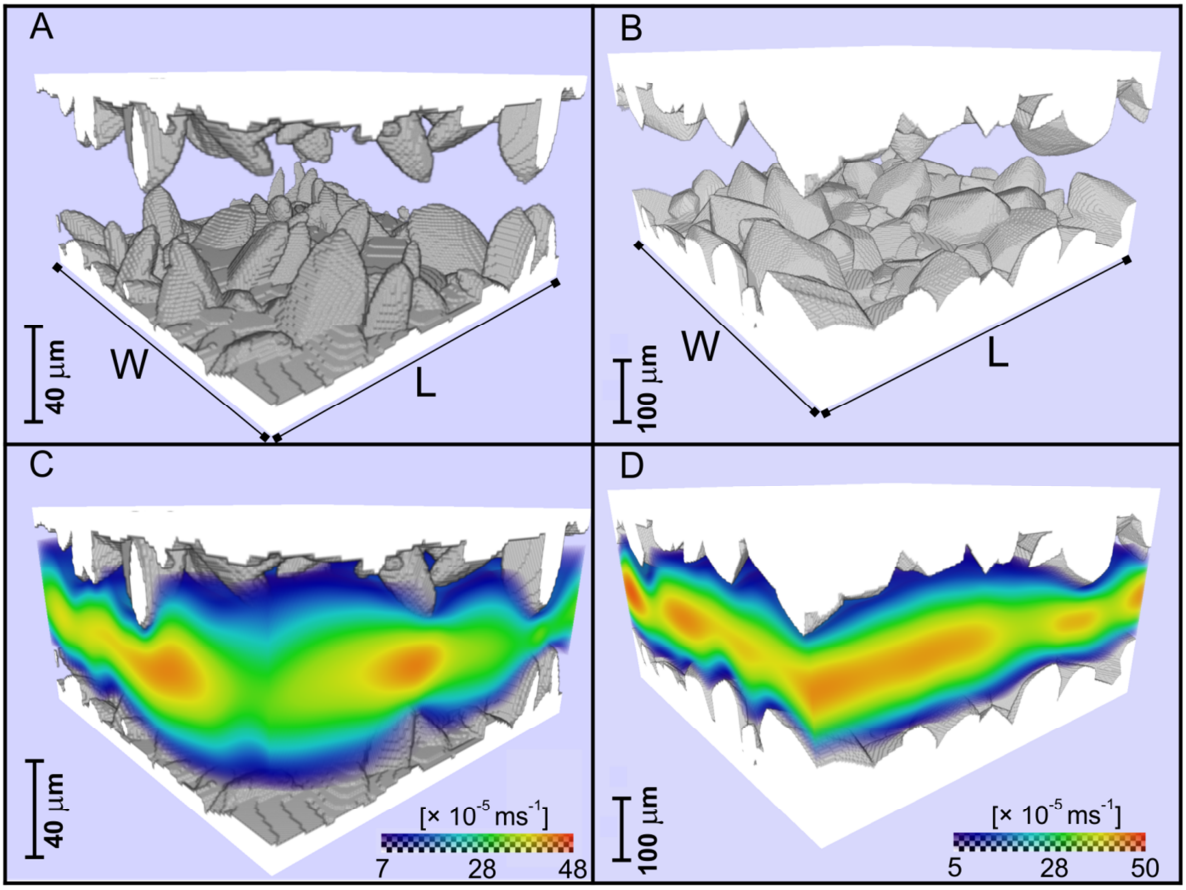

Fig. 4.2: Geometry of a planar fracture sealed by needle (A) and compact (B) quartz crystals at intermediate stages of respective sealing processes. CFD derived fluid flow field based on the quartz habit are visualized respectively (C and D). Red colors indicate high fluid flow velocity, whereas bluish colors denote low fluid flow velocity. Fluid flows from the left (*W*-axis) along the length (*L*-axis) direction.

The flow in the open (non-solid) regions of the fracture is described for viscous, incompressible fluids and stationary flows. Conservation of momentum (Eq. 4.3) and conservation of mass (Eq. 4.4) can be written as the stationary Navier-Stokes equation (NSE) in the pressure-velocity formulation:

$$-\mu\Delta\vec{u} + (\rho\vec{u}\cdot\nabla)\vec{u} + \nabla p = f_{NS} \tag{4.3}$$

$$\nabla\cdot\vec{u} = 0 \tag{4.4}$$

In Eqs. (4.3) and (4.4), $\vec{u}$ represents the fluid velocity, p is the pressure, μ is the dynamic viscosity of the fluid, ρ denotes fluid density and f_{NS} is the force density. The simulations compute the velocity field for a given pressure drop using periodic boundary conditions on the computational box and a Dirichlet boundary condition for the pressure. At the solid-to-fluid interface the no-slip boundary condition is applied considering adhesive forces between the two phases implying locally:

$$\vec{u}|_{boundary} = 0 \tag{4.5}$$

The NSE (Eqs. 4.3 and 4.4) are solved by using an explicit finite volume (EFV) method employing either the SIMPLE (Patankar and Spalding 1972) or the SIMPLEC method (Van Doormaal and Raithby 1984). Simulations are performed by using the commercial, voxel-based GeoDict (Math2Market GmbH) software package, which implements the mathematical requirements while enabling full parallelization of calculations.

In a post-processing step, GeoDict computes the permeability by default according to Darcy's law from the simulated velocity field (Kehrwald 2004; Schulz et al. 2005). However, Darcy's law is based on the permeability of a homogenous, porous medium so that the resulting permeability represents the entire computational domain. Hence, in order to consider only the exclusive permeability arising from the interconnectivity of local fracture voids, an adjusted form of Darcy's law is applied as outlined in Section 2.3. Admittedly, using the permeability as a measure for the hydraulic properties is more suitable for porous media, whereas Zimmerman and Bodvarsson (1996) correctly proposed the transmissivity as the more appropriate parameter for rock fractures. Nevertheless, ‘fracture permeability’ is standardly used for various macroscale models dealing with e.g. reservoir characterization (Nelson 2001; Toublanc et al. 2005; André et al. 2006), wellbore leakage (Huerta et al. 2016) or hydromechanical processes (Rutqvist et al. 2013b). Since the expected results of this study are intended to contribute to such issues, the hydraulic results are also presented as permeability.

The simulations are carried out for a fluid with the physical properties of water at a temperature of T = 20 °C and the respective values for density and dynamic viscosity (Fluid pressure p = 31 MPa) representing similar conditions as used for well tests at several geothermal fields such as the Icelandic Krafla (Bodvarsson et al. 1984) or the Mexican Los Azufres site (Benson et al. 1987). Pressure drops across the fracture length are set to 0.1 Pa for compact quartz and 2.8 Pa for needle quartz so that resulting Reynold's numbers are about 1.0 for the initial planar fracture and even lower for further stages to maintain laminar flow conditions. The simulation termination criteria are set to end the simulation when either an accuracy (ratio of current permeability and previously iterated permeability) of 1×10^{-5} is reached or after 10^5 iterations. The simulations are performed on a 32-core, 64-bit Intel Xeon server with 512GB of shared RAM. With this configuration and predefined discretization a 3D fluid flow simulation is performed in less than 30 min for both quartz types.

4.2.3 Fracture permeability

As mentioned above, an adjusted form of Darcy's law is applied to evaluate the simulated fracture permeabilities. In general, Darcy's law represents a special case of the incompressible, creeping, stationary Stokes equation (Whitaker 1986) and is written as

$$Q = \frac{k \cdot A}{\mu} \frac{\partial p}{\partial x} \tag{4.6}$$

to ascertain the volumetric flow rate Q (in m³/s) based on the bulk permeability k (in m²) of the medium, its cross-sectional area A (in m²), dynamic viscosity μ (in Pa·s) and a pressure gradient ($\partial p/\partial x$ in Pa·m^{-1}). By assuming laminar flow, Q can also be described as a linear function of the (superficial) Darcy velocity $\tilde{v}$ (in m·s^{-1}) in the whole flux surface which is represented by the computed mean velocity within the computational box:

$$Q = \tilde{v} \cdot A \tag{4.7}$$

Hence, the CFD code derives the permeability k of the medium by combining Eqs. (4.6) and (4.7) so that

$$k = \frac{\mu \tilde{v}}{\partial p / \partial x} \tag{4.8}$$

However, for each sealing fracture evolving in time a correction for the increasing amount of solid precipitate is required. Based on the assumption of a lateral continuation along the fracture plane

fracture flow rather depends on the interstitial velocity ⟨v⟩ within the non-solid regions which by definition is the ratio of the computed Darcy velocity $\tilde{v}$ and the effective porosity n_e so that the fracture permeability K can be written as

$$K = \frac{\langle v \rangle \mu}{(\partial p / \partial x)} = \frac{\tilde{v}\,\mu}{n_e(\partial p / \partial x)} \tag{4.9}$$

Thus, the effective porosity ne, which can be described by the ratio of the 'liquid voxels' volume to the total fracture volume, can be applied to correct the permeabilities computed by the GeoDict.

4.2.4 Fracture apertures

Fluid flow in single fractures most often is approximated by the well-known cubic law (CL) representing the one-dimensional, vertical integration of the Stokes equation (Brush and Thomson 2003; Zimmerman and Yeo 2013; Wang et al. 2015). When applying the cubic law

$$Q = \frac{a^3 W}{12\mu} \frac{\partial p}{\partial x} \tag{4.10}$$

the fracture is approximated by a pair of smooth parallel plates separated by a uniform mechanical aperture a (in m) while W (in m) represents the fracture width perpendicular to the flow direction. Analogous to Darcy's law Eq. (4.6), the CL reveals a simple relationship between the flow rate, a 'transmissivity term' and a potential gradient. Due to the equivalency of the 'transmissivity terms' in Eqs. (4.6) and (4.10) the transmissivity T of the fracture thus is equal to

$$\mathrm{T} = kA = \frac{a^3 W}{12} \tag{4.11}$$

where T is proportional to the cube of the aperture. Since this study however focusses the fracture permeability K, Eq. (4.11) requires a further simplification by assuming A = W · a so that the fracture permeability K can be expressed by

$$K = \frac{a^2}{12} \tag{4.12}$$

However, natural fractures typically do not behave like parallel plates with a uniform aperture *a*. Instead, fracture surfaces reveal a certain roughness that can be more or less significant and causes

deviations from the parallel plate approach. Therefore, a can be described by an equivalent aperture a_m which is defined as a mean of the local apertures along the rough fracture planes (Brown 1987; Zimmerman and Bodvarsson 1996). There are various synonyms for a_m in literature such as mechanical, geometrical or macroscopic aperture (Neuville et al. 2010). Unfortunately, the term "mechanical" implies a kinematic background. In order to avoid this misleading, in this study a_m is defined as the mean aperture which is equivalent to the chemical aperture introduced by Wen et al. (2016) which refers to the mineral volume change. Indeed, a_m represents a practical reference value to describe the relative position of both surfaces, however neglects existent aperture patterns or hydraulic features such as turbulence contributing significantly to actual fracture flow (Tsang 1984). Hence, the effective hydraulic aperture a_h is introduced, which directly relates to the actual fluid flow through the fracture (Zimmerman and Bodvarsson 1996) and can be seen as the aperture of a virtual 'parallel plate' fracture that is required to allow a certain volumetric flow rate. Typically, the hydraulic aperture a_h is smaller than a_m on the (global) fracture scale, but can also be occasionally larger when considering local values along the discretized fracture plane (Neuville et al. 2010). Thus, several empirical correction factors are introduced to account for e.g. the fracture roughness and to scale down global a_m values (Louis 1972; Witherspoon et al. 1980). Over time, several authors established different correlations between a_h and a_m, based on either the joint roughness coefficient (Barton et al. 1985; Olsson and Barton 2001), the fractal geometry (Drazer and Koplik 2002), the Z2-value (Zhao et al. 2014) or the relative roughness (Lomize 1951; Louis 1972; Patir and Cheng 1978; Brown 1987; Zimmerman et al. 1991; Amadei and Illangasekare 1994; Renshaw 1995; Barton and de Quadros 1997; Matsuki et al. 1999; Rasouli and Hosseinian 2011; Xiong et al. 2011; Xie et al. 2015). In this study, we focus on the relative roughness (σ/a_m) depending on the (averaged) mean aperture a_m of a fracture and its standard deviation σ. In the past, several equations were derived for chemically unaffected fractures that are summarized in Table 4.1. These equations often represent valuable approaches to approximate actual a_h values, however also reveal individual limitations and do not provide a universal solution for permeability prediction (Souley et al. 2015). Among others, these limitations most widely rely on the fact that these models agree with study-specific fractures, which do not cover the full range of possible roughness features such as anisotropy, spatial correlation or tortuosity. For this reason, Zimmerman and co-authors (Zimmerman et al. 1992; Zimmerman and Bodvarsson 1996), for instance, introduce an additional term based on contact areas improving their previous approach (Table 4.1, Zimmerman et al. 1991) for tortuosity.

Table 4.1: Summary of formulations to describe hydraulic apertures (a_h) based on mean apertures (a_m) and the relative roughness depending on the standard deviation (σ) of a_m caused by the unevenness of the fracture surfaces. The originally cubic notations of the equations, which directly refer to the fracture transmissivity, are depicted by their cube root, which is more convenient to calculate fracture permeabilities of this study.

Equation	Annotations	Fracture type	Reference
$a_h \approx \frac{a_m}{\sqrt[3]{1+A\left(\frac{\sigma}{2a_m}\right)^{1.5}}}$	A=17.0 A=8.8 A=20.5	Sand coated plates Rough concrete plates Natural granite fractures	Lomize (1951) Louis (1972) Barton and de Quadros (1997)
	A depends on fractal dimension (F_D) where A=2.7 to 3.22 for F_D =2.5 to 2.0	Numerical fractal model	Brown (1987)
$a_h \approx a_m \sqrt[3]{1 - B \cdot \exp\left(-C\left(\frac{a_m}{\sigma}\right)\right)}$	B and C depend on Peklenik number γ, roughness (σ/a_m) or fractal dimension (F_D):	Stochastically generated surfaces	Patir and Cheng (1978)
	Typically: B=0.9 and C=0.56 (for γ=1, σ/a_m = 1.3 to 2.0) For γ≠1, $\sigma/a_m \neq$ 1.3–2.0 or F_D= 2.0–2.5: cf. References	Numerical fractal model	Brown (1987)
$a_h \approx a_m \sqrt[3]{\left(1 - 1.5\frac{\sigma^2}{a_m^2}\right)}$		Idealized mathematical (sinusoidal and saw-tooth) fracture models	Zimmerman et al. (1991)
$a_h \approx \frac{a_m}{\sqrt[3]{1+0.6\left(\frac{a_m}{\sigma}\right)^{-1.2}}}$		Synthetic fractal model	Amadei and Illangasekare (1994)
$a_h \approx \frac{a_m}{\sqrt[3]{\left(1+\frac{\sigma^2}{a_m^2}\right)^{1.5}}}$		Theoretical equation based on stochastics of aperture distributions	Renshaw (1995)
$a_h \approx a_m \sqrt[3]{1 - \frac{1.13}{1+0.191\left(\frac{2a_m}{\sigma_0}\right)^{1.93}}}$	Revised Lomize-equation (Lomize 1951) with an initial standard deviation σ_0 to include mechanics. However, also works for $\sigma_0 = \sigma$.	Tensile granite fracture (Scan)	Matsuki et al. (1999)
$a_h \approx a_m \sqrt[3]{\left[1 - D\frac{\sigma}{a_m}\right]}$	D = 1.0	Replicas of a split sandstone and natural granite fracture	Xiong et al. (2011)
	D ranges between D_{min} = 1.0, D_{mean} = 2.25 and D_{max} = 3.7.	Synthetic statistical model	Rasouli and Hosseinian (2011)
$a_h \approx a_m \sqrt[3]{0.94 - 5.0\frac{\sigma^2}{a_m^2}}$		Tensile sandstone fracture	Xie et al. (2015)

From the PFM simulation data, the mean aperture can be calculated as the ratio of the integrated overall non-solid volume and the 2D fracture plane (e.g. for needle quartz: width (W) × length (L) = 150 × 150 µm²). This is fully equivalent to averaging of local apertures. In order to determine the distribution of local apertures along the fracture the vertical summation of all non-solid voxels for each mesh element over the fracture plane is required. The global hydraulic aperture a_h is computed from each CFD model by using Eq. (4.10) based on the volumetric flow rate Q. The latter is calculated by areal integration of all fluid velocity components in the free-flow voxels, perpendicular to a slice of the simulation box that is, in turn, perpendicular to the pressure gradient. Here, by implementing a_h into Eq. (4.12) reveals, that calculated permeabilities are in good accordance with simulated permeabilities derived by Eq. (4.9).

Local hydraulic apertures are calculated based on Eq. (4.10) taking account of the local volumetric flow rates and pressure gradients for each mesh element of the fracture plane. The local flow rate is determined by vertically summing up simulated local flow velocities and multiplying the single sums with their respective cross sectional areas (e.g. voxel face area × number of non-solid voxels). Local pressure gradients also are determined by vertically averaging all simulated pressure values in the fluid voxels. Finally, local gradients are derived by differentiating between the single local pressures and their respective neighboring pressures along the global flow direction.

4.3 Results and discussion

This section is split in three parts, namely in (1) an overview about the global fracture properties and hydraulics, (2) a careful consideration of fracture properties at local scales and (3) the discussion of possible interconnections to global hydraulic properties. Different stages of sealing are represented as a function of dimensionless (numerical) time steps, since this study only focusses on the effect of different fracture geometries and does not consider time-dependent growth kinetics of the crystals. Otherwise, the time steps can be multiplied with t_0 = 1162 s (Wendler et al. 2015) to infer the physical times from the respective simulation steps (~10.0 days for 'needle quartz', ~7.7 days for compact quartz).

4.3.1 Global fracture hydraulics

The results of fluid flow simulations show a distinct negative correlation between progressive fracture sealing and permeability evolution (Fig. 4.3). However, the intensity of this correlation depends on the hydraulic properties (Fig. 4.4 and Fig. 4.6) which in turn rely on growth characteristics of the quartz phase. The most prominent impacts of the crystal shape are (I) the different velocities at which the fracture is closed, (II) the influence on corresponding fracture permeabilities (Fig. 4.3 and Fig. 4.4) and

(III) the formation of locally different aperture geometries (cf. Fig. 4.2) or fracture porosities (Fig. 4.4). To avoid cumbersome terms, the fractures that are sealed by needle or compact quartz in the following are termed ‘needle fracture’ and ‘compact fracture’, respectively.

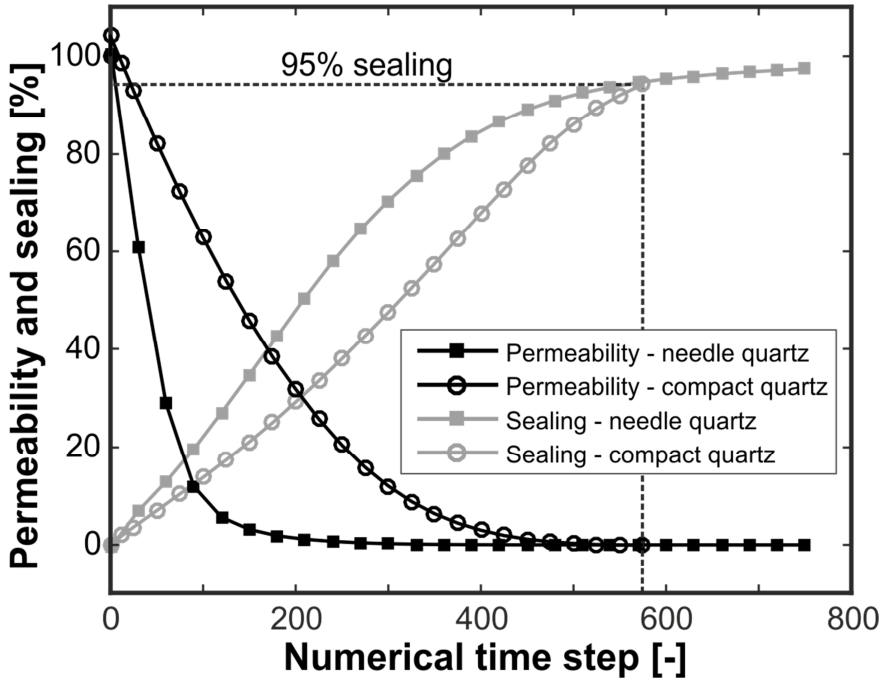

Fig. 4.3: Relative evolution (in percent) of fracture sealing and permeability caused by needle or compact quartz growth.

For both fractures maximum hydraulically effective sealing (less than 1% of initial permeability)is reached when approximately 95% of the fractures are filled with quartz, which for both fractures applies after similar growth intervals (~7.7 days) (Fig. 4.3). Hence, both growth scenarios of needle and compact quartz should be comparable although there are different initial fracture and crystal dimensions. The varying rates of fracture sealing most widely can be subjected to the growth behavior of the different quartz crystals. While needle quartz preferably grows vertical, compact quartz also features more significant lateral growth, where some crystals are overgrown. Thus, at the beginning several compact quartz crystals are obstructed by neighboring crystals, which in turn need more time to fully evolve over the enhanced growth area (Fig. 4.2). Such a growth competition is also observed by Hilgers et al. (2004) for syntaxial growth of ‘compact’ alum crystals.

The initial decrease in permeability is more pronounced for the ‘needle fracture’ than for the ‘compact fracture’ (Fig. 4.3). After 20% of sealing, the ‘needle fracture’ exposes less than 20% of its initial permeability, but the ‘compact fracture’ still disposes more than 40% (Fig. 4.3). Since both fractures

are equally sealed with respect to their initial fluid volume, this effect cannot be attributed to the differences in initial aperture. Instead, this effect can be attributed to the different crystal habits and their growth behavior within the fractures. According to the different parallel plate models initial permeability of the 'needle fracture' (4.0×10^{-10} m²) is significantly smaller compared to the 'compact fracture' (7.1×10^{-9} m²). However, with progressive sealing the permeability of the 'needle fracture' drops by nearly 5 orders of magnitude to a minimum permeability of 5.6×10^{-15} m² (Fig. 4.4A). The residual permeability of the 'compact fracture' even attains a lower value of 1.7×10^{-16} m² corresponding to a drop by almost 8 orders of magnitude (Fig. 4.4B). Both fractures exhibit an approximately exponential decrease in permeability in the initial stage of sealing as also observed for mechanical fracture closure (Huo and Benson 2015; Kling et al. 2016) (Fig. 4.4). The main permeability reduction of the 'needle fracture' occurs at the initial sealing stages ($t < 125$); however its slope significantly decreases with ongoing sealing (cf. Fig. 4.3). In contrast, major permeability reduction of the 'compact fracture' occurs at later stages ($t > 375$) where permeability abruptly decreases.

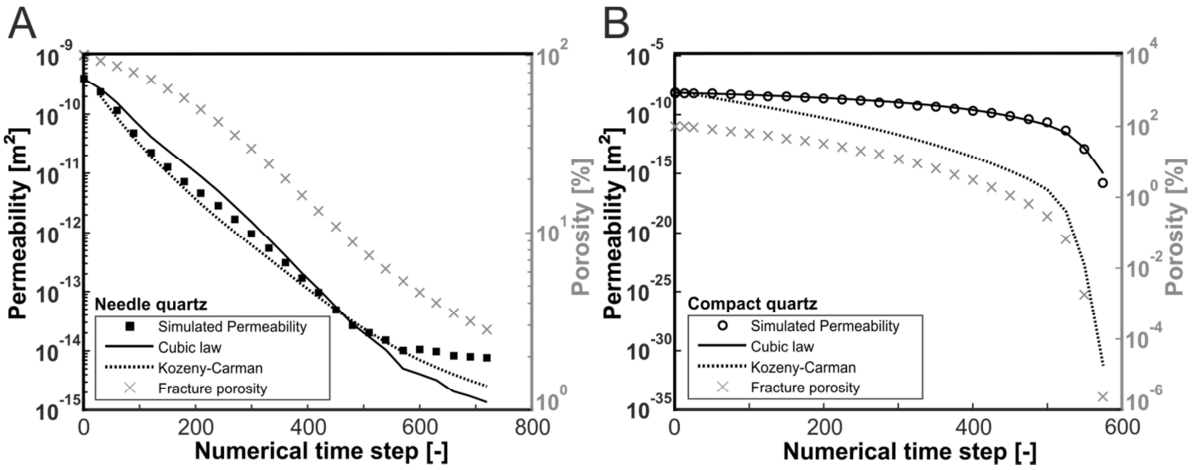

Fig. 4.4: Time evolution of simulated permeabilities and porosities for needle and compact quartz sealing. Empirical permeability models are also shown.

The different behaviors in permeability reduction significantly refer to differences in the morphology of the sealing structures due to needle or compact quartz crystallization. Compact quartz typically forms contiguous growth fronts growing against each other resembling two rough fracture walls that are closed mechanically. This growth behavior is also reflected by the initially slow decrease in permeability and the abrupt drop once both growth fronts meet each other where most voids are rapidly closed (Fig. 4.4). On the contrary, randomly orientated growth of isolated needle quartz forms void structures resembling a porous medium. With increasing length, single quartz crystals meet each other

and establish a mesh of randomly orientated bridge structures. Both, the growth of isolated crystals as well as the resulting formation of bridges implicate all permeability-reducing factors described by Tsang (1984): fast fracture closure (or sealing); a decrease in connectivity by forming fewer flow channels; and an increase in tortuosity by forming additional barriers. Accordingly, the initial permeability-reduction is more pronounced for the 'needle fracture' than for the 'compact fracture' (Fig. 4.4), however levels off as soon as sealing is inhibited by missing space for further free growth.

The fact that the 'needle fracture' rather resembles a porous medium is not only represented qualitatively e.g. by Fig. 4.1, but also becomes evident when applying the Carman–Kozeny (CK) equation (Carman 1937). The CK equation typically describes the porosity-permeability relationship of a packed bed of solids, and within the scope of this study is applied in its classical form:

$$K = c\frac{n^3}{S^2} \tag{4.13}$$

where fracture permeability K relates to the porosity *n*, Kozeny's (geometry) coefficient c and the specific surface area *S* (crystal-surface area / bulk volume). In order to determine surface areas of the quartz crystals, a marching cubes algorithm (Newman and Yi 2006) of the Python image processing tool 'scikit-image' is added to the PFM code. Kozeny's coefficient c was introduced as an empirical correction value for the shape of the channels conducting the fluid through the porous medium. However, Mortensen et al. (1998) found that c also can be described analytically as a function of porosity assuming two equivalent model approaches containing circular or rectangular tubes. Assuming polygonal void geometries for the sealing fractures, this study only refers to the circular tubes model, for which coefficient c can be written as follows

$$c = \left[4\cos\left(\frac{1}{3}\cos^{-1}\left(n\frac{8^2}{\pi^3} - 1\right) + \frac{4}{3}\pi\right) + 4\right]^{-1}. \tag{4.14}$$

Based on this, the KC equation (Eq. 4.13) and the hydraulic aperture related cubic law (Eq. 4.12) were applied for both, 'needle' and 'compact fractures' (Fig. 4.4). Results for the 'needle fracture' indicate that both equations fit simulated permeabilities quite well. In particular, the good fit with the KC equation (Eq. 4.13) reflects the porous structure of the fracture geometry after sealing starts. However, both permeability models appear to underestimate permeability significantly at later sealing stages. Here, the fracture is almost closed and features a significant increase in tortuosity (cf. Fig. 4.1), but also forms isolated areas of fluid within the quartz crystals. Hence, the deviations most probably are caused by the effective porosity ne values to determine simulated permeabilities, which are based on

the respective bulk fluid volumes, so that the isolated pore surfaces factor into Eq. (4.9) and overestimate actual permeabilities. Analytically derived Kozeny's coefficients c range between a minimum value of 0.17 and 0.40 with decreasing sealing, while c for natural porous media typically range between 0.22 and 0.24 (Mortensen et al. 1998)(Mortensen et al., 1998). In contrast, the KC approach does not reproduce the permeabilities of the 'compact fracture', while cubic law results almost coincide (Fig. 4.4B). These deviations are caused by the closing mechanism of the two growth fronts forming rather locally varying flat to irregular plates than a bundle of capillary tubes. Instead, a capillary tubes model representing a porous medium was applied to calibrate Kozeny's coefficients c. In fact, c should be significantly higher to fit CK equation for the 'compact fracture', which requires a geometrical correction as e.g. applied for also KC-based "equivalent channel models" in the past (Walsh and Brace 1984; Bernabe 1986b).

4.3.2 Local hydraulic fracture properties

Before considering hydraulic properties as commonly used area-related averaged (global) values, the local hydraulic fracture properties are carefully discussed. This is important, since fluid flow strongly depends on the spatial distribution and correlation of aperture sizes (Hakami and Larsson 1996; Schwarz and Enzmann 2013). In other words, fractures theoretically can have similar average apertures a_m and standard deviations σ, however different distributions of voids and contact areas affecting the spatial alignment (e.g. connectivity or tortuosity) of flow channels.

For this reason, the 2D spatial distributions of the local apertures (SDA) (Fig. 4.5A and B) as well as the fluid flow rates are considered (Fig. 4.5C and D). Complementary to these spatial representations, respective statistical aperture size distributions (ASD) are given for further details as histograms (Fig. 4.5E and F). Exemplarily, the SDAs, local flow rates and ASDs are considered for the 'needle' and 'compact fractures' at 20% fracture sealing (Fig. 4.5).

The results indicate that the flow behavior within both fractures significantly depends on local apertures und related flow paths and thus is directly related to the crystal habit of the sealing phase. In the case of needle quartz (Fig. 4.5A), several areas exist where crystals approached by forming high angular bridge structures. The presence of bridges causes a distribution of locally accumulated contact areas ('Swiss cheese pattern') that form effective barriers for fluid flow and result in adjacent large downstream areas, where fluid flow is significantly reduced (Fig. 4.5C). Such bridging structures are a widespread features in many permeable fractures and were most widely found in sedimentary rocks such as sandstones, dolostones and mudstones as calcitic or silica fracture fillings (Lander and Laubach 2015). However, these bridge structures arise from localized cement accumulations disconnected by areas of thin veneers of cement (Laubach et al. 2004). It was found that porosity as well as connectivity

of such fracture sealing highly depend on the initial aperture width of the pre-sealed fracture (Laubach et al. 2004; Gale et al. 2010). Especially, for fracture apertures > 0.1 mm bridges are slim enough to provide sufficient pore connectivity (Gale et al. 2010). Hence, the simulations for the 'needle fracture' can provide first insights into the hydraulics of such natural sealing structures.

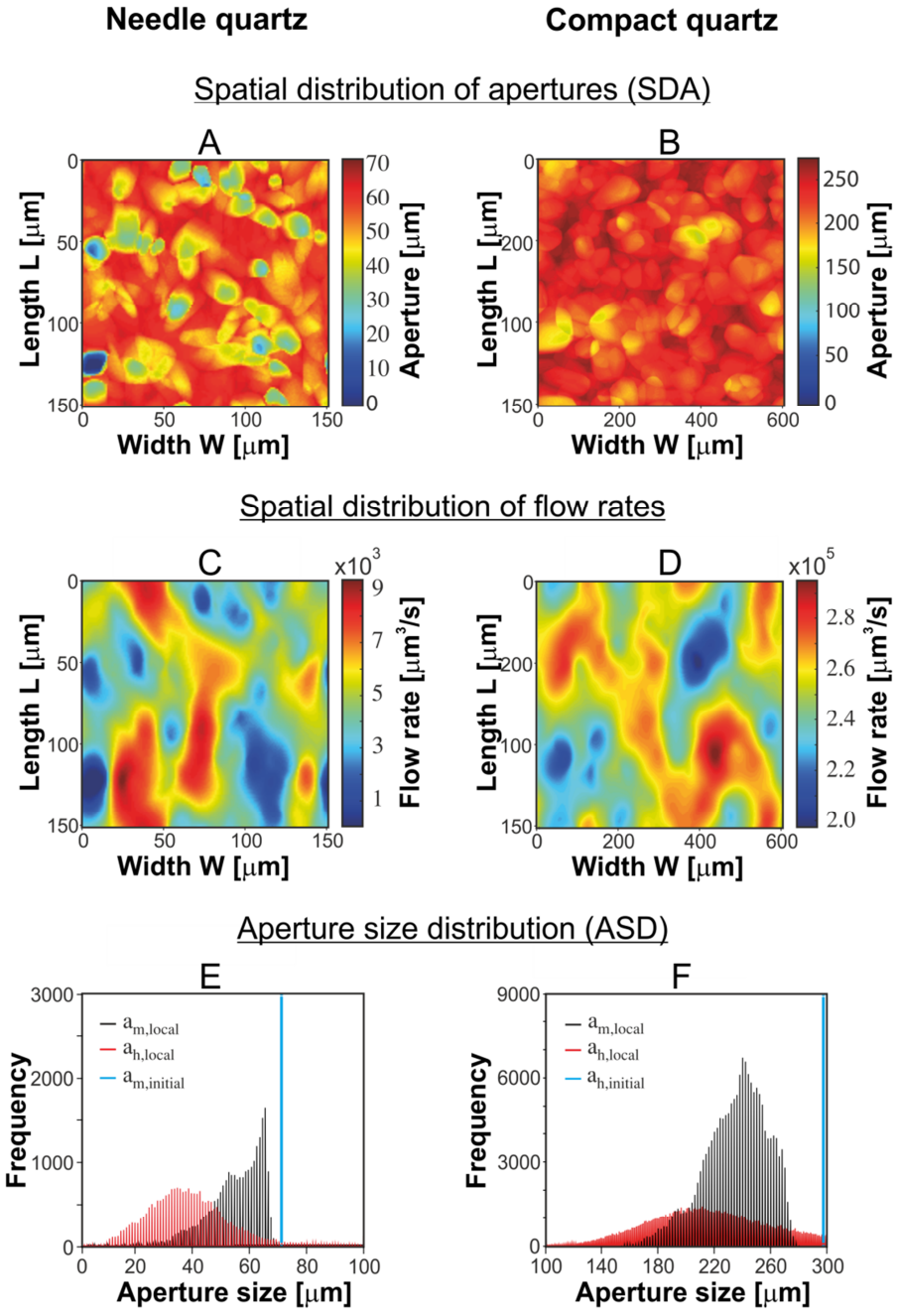

Fig. 4.5: Spatial distribution of local apertures (A, B), spatial distributions of flow rates (C, D) and aperture size distributions for the local mean ($a_{m,local}$) and hydraulic ($a_{h,local}$) apertures (E, F) for needle (left) and prismatic quartz (right). Both simulations are at 20% fracture sealing. The dotted blue line (E and F) describes the aperture ($a_{m,initial}$) of the respective initial (parallel plate) fracture. Fluid is injected (C, D) at the lower *W*-axis and flows along the *L*-axis.

For the ‘compact fracture’ bridging most widely occurs only towards the end of the sealing process being in accordance with (nearly) simultaneous coalescence of the growth fronts as discussed in Section 3.2. Considering the fracture at 20% sealing neither bridges nor contact areas are developed (Fig. 4.5B). Nevertheless, regions with a lower aperture built bottlenecks for fluid flow and cause the development of flow anisotropy (Fig. 4.5D), where enhanced fluid flow occurs along preferred less resistant pathways (channels).

Accordingly, ASDs of the local geometrical and hydraulically effective apertures (Fig. 4.5E and F) expose that the mode of the hydraulically effective apertures is smaller than the mode of geometrical aperture distribution ($\tilde{a}_m$). In contrast to mechanically induced aperture distributions, which typically are described as lognormal, gamma or truncated normal distributions (Renshaw 1995; Oron and Berkowitz 1998), both sealing fractures reveal a negatively skewed (non-normal) aperture distribution, while hydraulic apertures are somewhat lognormal distributed. Hence, the ASDs illustrate that in parts the number of local hydraulic apertures ($a_{h,local}$) even exceed the number of larger geometrical apertures (where $a_{m,\ local} > \tilde{a}_m$). Locally values for $a_{h,local}$ even exceed the initial aperture of the parallel plates. Accordingly, in some parts of the fracture more fluid is conducted than it is anticipated by the cubic law which assumes $a_h \leq a_m$. This shows that hydraulics within apertures is not entirely defined by the local geometries and pressure gradient, but also depends on the properties of surrounding fracture parts. This was also concluded by Neuville et al. (2010) for rough fracture models without a sealing component. However, this finding does not affect the flow properties on the global scale of rough fractures (equivalent to the means of the ASDs), where a_m typically remains larger than a_h.

For this reason, the 2D spatial distributions of the local apertures (SDA) (Fig. 4.5A and B) as well as the fluid flow rates are considered (Fig. 4.5C and D). Complementary to these spatial representations, respective statistical aperture size distributions (ASD) are given for further details as histograms (Fig. 4.5E and F). Exemplarily, the SDAs, local flow rates and ASDs are considered for the ‘needle’ and ‘compact fractures’ at 20% fracture sealing (Fig. 4.5).

4.3.3 Global hydraulic fracture properties

The results for mean (a_m) and hydraulic apertures (a_h) agree with theoretical expectations (Fig. 4.6A and C) where $a_h \leq a_m$. Contemporaneously, this decrease in apertures is coupled with an increase in relative roughness (σ/a_m). The initial increase in relative roughness for both fractures is highly related to the formation of the euhedral faces of the quartz crystals causing a decrease in a_m and - with ongoing crystal evolution - an increase of unevenness reflected by a significant increase of the standard deviations σ of a_m. Particularly, this becomes obvious for the ‘needle fracture’ where free growth of the quartz crystals establishes “Manhattan skyline” -like fracture surfaces, so that σ/a_m is highly

pronounced (for t = 0–100). While the rates of increase in roughness for the 'needle fracture' mitigate with ongoing sealing, due to the filling of previously formed interspaces, rates for the 'compact fracture' are more constant reflecting the growth fronts (Fig. 4.6A and C).

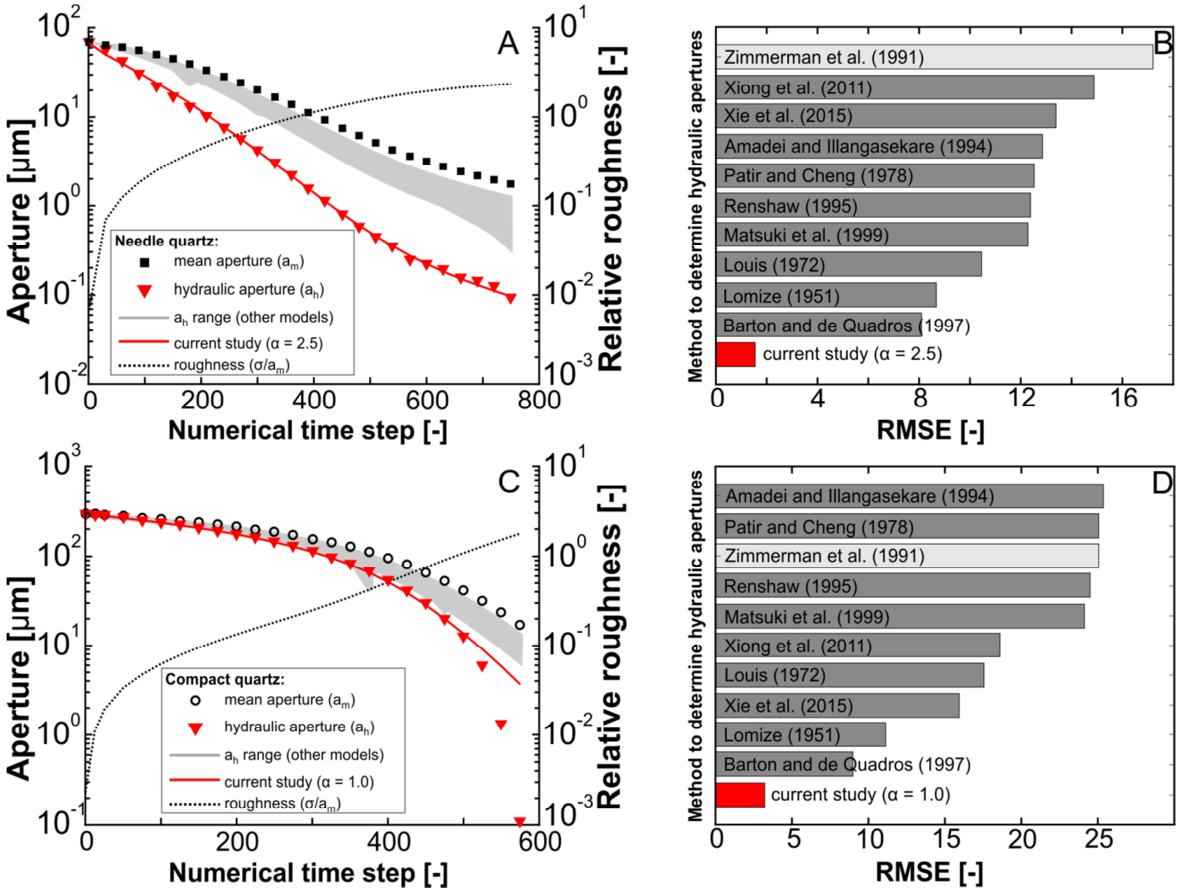

Fig. 4.6: Comparison of time-dependent development (A and C) of average hydraulic (a_h) and mean apertures (a_m) for needle and compact quartz discerned from the phase-field and fluid flow simulations. The red line represents results for the semi-theoretical equation introduced in this study (cf. Eq. 4.19). Additionally, hydraulic apertures are compared to the range of further a_h–a_m–relationships (cf. Table 4.1) directly (A and C) and absolute by the root-mean-square error (RMSE, B and D). The light grey RMSE bar for the (Zimmerman et al. 1991) equation is comprised for the sake of completeness but not competing since the authors explicitly discussed the shortcomings of this equation in subsequent papers (Zimmerman et al. 1992; Zimmerman and Bodvarsson 1996) and even enhanced it.

Considering the increasing deviations of a_h from a_m indicates that there should be a direct relationship to the progressive changes in relative roughness, but these changes also appear to implicate further changes of properties such as tortuosity and connectivity. Hence, to find a direct relationship between mean and hydraulic apertures several assumptions are made. As stated in Section 2.4 (Louis 1972;

Witherspoon et al. 1980) both aperture types are directly correlated to the reciprocal of a correction factor (*f*) considering roughness-related friction:

$$\left(\frac{a_h}{a_m}\right)^3 = \frac{1}{f} \tag{4.15}$$

This friction factor must be one ($f = 1$) in the case of two parallel plates with zero roughness (σ/a_m) so that $a_m = a_h$. However, *f* must be larger one to account of roughness and to correct a_m (Witherspoon et al. 1980). Hence, an initial simplified correction factor (f_I) is predefined by

$$f_I = 1 + \frac{\sigma}{a_m} \tag{4.16}$$

However, Patir and Cheng (1978) found that friction not only depends on simple roughness, but also depends on the shape of contact areas having a direct effect on tortuosity, and introduced the Peklenik number (Peklenik 1967) to correct the roughness for the directionality of contact areas (cf. Table 4.1). Thus, a new geometry factor α is introduced and implemented in Eq. (4.16) resulting in another preliminary friction factor f_{II}:

$$f_{II} = 1 + \alpha\frac{\sigma}{a_m} \tag{4.17}$$

According to Eq. (4.15) there has to be a total positive correlation between $(a_h/a_m)^3$ and $(1/f)$ However, replacing the actual friction factor *f* by the theoretically derived, preliminary f_{II} (Eq. 4.17) indicates a significant non-linear relationship (Fig. 4.7). In order to obtain the total positive correlation two assumptions are made: (1) the curves of the data points for both fractures have to conform and (2) the following power law relationship is valid:

$$\frac{1}{f} = \left(\frac{1}{f_{II}}\right)^b \tag{4.18}$$

By fitting both curves of the fractures (Fig. 4.7) by the unknown α (Eq. 4.17) and b (Eq. 4.18), it is found that the geometry factor is about α = 2.5 for the 'needle fracture' and α = 1.0 for the 'compact fracture' with common exponent b = 4.5. Subsequently, Eqs. (4.15), (4.17) and (4.18) can be combined to obtain following relationship between a_h and a_m

$$a_h = a_m \left(1 + \alpha \frac{\sigma}{a_m}\right)^{-\frac{3}{2}} \tag{4.19}$$

Calculated hydraulic apertures (a_h) by applying Eq. (4.18) and predefined input parameters are depicted in Fig. 4.6A and C. As was expected, the derived a_h values for both fractures are in line with the simulated a_h values. Larger deviations are observed for the final sealing stages of the 'compact fracture'. This seems to be due to merging of both surfaces offering a significant transition of the fracture morphologies. The transition from an open, rough to a porous-like, bridged fracture also implies a possible change of the geometry factor towards higher α values similar to the 'needle fracture'.

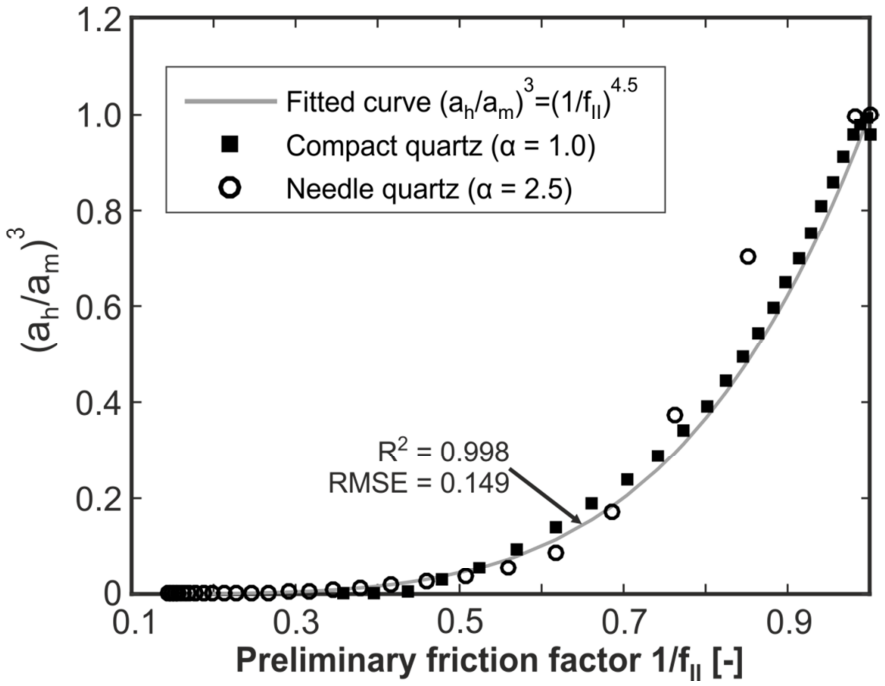

Fig. 4.7: Calibration function fitting the ratios of hydraulic (a_h) and mean apertures (a_m) as well as the reciprocal friction factor (f_{II}). The latter is based on fracture roughness and a respective geometry factors (α) according to Eq. (17). Fitting is performed by excluding outliers which are below the 10th and above the 90th percentile of cumulative ratios of the logarithmized input parameters for needle and compact quartz growth.

Typically, values for the friction factors (f) range between 1.04 and 1.65 for chemically unaffected, rough fractures (Witherspoon et al. 1980). This applies for the initial sealing phase (t = 0 to ~90) for the 'needle fracture' and until the merging-phase (t = 0 to ~400) for the 'compact fracture'. Accordingly, f-values confirm the assumption that partly sealed 'compact fractures' hydraulically

behave like tensile fractures without a sealing component. However, with ongoing sealing, f-values increase to a maximum of 18.3 (‘needle fracture’) and 4.7 (‘compact fracture’). Hence, the formation of highly tortuous flow paths in sealing fractures causes *f*-values that are significantly higher than those of tensile fractures. The extraordinary high *f*-values ($f \gg 5$) of the ‘needle fracture’ can be ascribed to the pronounced 3D tortuosity of the flow paths (cf. Fig. 4.1) due to the capillary structure of the void pattern (as compared to with ‘compact fracture’ or tensile fractures).

For comparison and demonstration of the new equation (Eq. 4.19), several congeneric empirical a_h–a_m–relationships (Table 4.1) are applied and also depicted by their summarized range of possible results (Fig. 4.6A and C). These equations are applied to the full range of available fracture properties, except for three approaches (Zimmerman et al. 1991; Xiong et al. 2011; Xie et al. 2015), where the functions become discontinuous, if σ/a_m exceeds its range of validity (cf. Table 4.2). The results of these equations indicate a general overestimation of the resulting a_h values, particularly for the ‘needle fracture’ (Fig. 4.6A and C). Although Fig. 4.6C does not indicate significant deviations between the used formulations for the ‘compact fracture’, root-mean-square errors (RMSE) are similar or even higher than RMSEs of the ‘needle fracture’ (Fig. 4.6B and D), which can be ascribed to an artefact due the scaling of the ordinate. Indeed, RMSEs are determined for the full range of calculated values as long as the functions are continuous, however can also be restricted due to their theoretical range of validity, according the fracture roughness (Table 4.2). In this study, values for σ/a_m vary from 0 to 2.4 for the ‘needle fracture’ and from 0 to 1.8 for the ‘compact fracture’ so that maximum roughness values are significantly higher than predefined for most other equations. Thus, limitations of the prior equations are not only caused by the validity of σ/a_m, but are also linked to fact that these models are calibrated for different chemically unaffected fracture types (e.g. idealized, synthetic, artificial or natural fractures, cf. Table 4.1) and therefore are valid only for specific fracture geometries.

The equation introduced in this study (Eq. 4.19) takes account of different geometries by comprising a constant geometry factor α. Thus, the geometry factor for ‘compact quartz’ ($\alpha = 1.0$) indicates that the moderately irregular geometries, evolving within the fracture, effectively are negligible. Fracture flow appears to rely only on the surface roughness. In contrast, the ‘needle fracture’, requires a significantly higher geometry factor ($\alpha = 2.5$) accounting for additional effects besides the surface roughness. This correction appears to be related to the heterogeneous growth fronts forming geometry-related flow paths which significantly differ from the ‘compact fracture’. Thus, the high geometry factor appears to be linked to more pronounced tortuosity which in turn is directly linked to the presence, amount and shape of contact areas (Patir and Cheng 1978; Zimmerman et al. 1992). This link to tortuosity would also explain why the ‘compact fracture’, which do not feature any pronounced tortuous flow paths, exhibits a geometry factor ($\alpha = 1.0$) similar to potential zero-tortuosity factors. Based on their

definitions (Ghanbarian et al. 2013), geometrical as well as hydraulic tortuosity values should approximate a value of one for nearly straight flow paths. Unfortunately, there are no information about either geometrical or hydraulic tortuosity of the simulated fractures to proof weather the geometry factor only represents a correction factor for tortuosity. However, a direct link between α and tortuosity appears to be questionable due to the observation of morphological changes during sealing. Hence, there should also be a change in tortuosity with progressive sealing in particular for the 'needle fracture'. Therefore, it seems to be more likely that the factor α can be associated with an additional correlation of further variable fracture and/or fluid properties that have not been considered yet.

Table 4.2: Theoretical or reported ranges of validity concerning relative roughness for previous (cf. Table 4.1) and new equations to predict hydraulic apertures of fractures.

Equations	**Range of validity of relative roughness (σ/a_m)**
Lomize (1951) Louis (1972) Barton and de Quadros (1997)	0.066–1.724 0.066–1.0 > 0.066
Patir and Cheng (1978)	1.111–1.786
Zimmerman et al. (1991)	< 0.816
Amadei and Illangasekare (1994)	< 1.0
Renshaw (1995)	< 1.0 *
Matsuki et al. (1999)	< 2.441 *
Xiong et al. (2011)	< 0.939
Xie et al. (2015)	< 0.434 *
Current study	0–2.386 (needle quartz) 0–1.789 (compact quartz)

* Describes minimum roughness (σ/a_m) before hydraulic apertures become unrealistic ($a_h < 0\mu m$).

4.3.4 Implications for geoscientific applications

Precipitation of mineral phases can play an important role particularly for the engineering of naturally fractured rock formations. This issue is unambiguous and easy to handle for completely sealed fractures, where preferential flow paths are clogged and form non-permeable hydraulic barriers (Nelson 2001). However, partially sealed fractures are significantly more challenging. Nelson (2001) even goes so far and depicts such rock features as "the nemesis of flow prediction and quantification in

fractured reservoirs". This becomes clear, when considering conventional analytical upscaling approaches or numerical flow models based on discrete fracture networks (DFN), where the hydraulic aperture or fracture permeability is a necessary input parameter (Blum et al. 2005; Zeeb et al. 2010). Of course, required hydraulic properties also could be approximated by only accounting for the mean aperture a_m or (if possible) by incorporating one of the already existing, roughness-related correction terms (cf. Table 4.1), but should be treated with caution. As shown in Fig. 4.6, accounting only for a_m may works well for 'compact fractures' (with < 60% of sealing). In comparison, the 'needle fracture' reveals deviations in mean apertures and simulated hydraulic apertures up to a factor of one, which causes deficiencies in permeability prediction of approximately 10^{-2} m². Significant deviations are also observed for hydraulic apertures that are calculated by traditional models using the relative roughness. Thus, applying Eq. (4.19) in particular is recommended for 'needle fractures'. Fractures are ubiquitous in almost all solid rocks and often contribute to rock mass permeability so that sealing structures can be an issue of for various tasks (Laubach 2003). Quartz, which is central in this study, is a typical mineral occurring in fractures, however not uncommonly forms different paragenetic associations as shown for various underground laboratories in crystalline rocks (Schill et al. 2016). Even so, Eq. (4.19) should be applicable or a good approximation as long as the present minerals also form adequate sealing morphologies. As mentioned in the introduction of this study, the findings of this study can have economical, technical or environmental aspects concerning the feasibility of exploiting naturally fractured geothermal (Meller et al. 2017) or hydrocarbon reservoirs (Nelson 2001). An overestimation of permeability also could affect decision making, concerning permeability control or groundwater control methods (e.g. grouting, water curtains or drainage pumps) as hydraulic barriers, whose functionality is essential for underground repositories hosting natural gas, oil or nuclear waste (Kjørholt and Broch 1992; Kim et al. 2011; Li et al. 2017). Especially in grout penetration of tunnels, dams and foundation works the cubic law still is a common method in fractured rocks to optimize workflows (Hernqvist et al. 2012; Stille et al. 2012; Kvartsberg and Fransson 2013), so that an adequate description of the hydraulic rock properties is the basis for the penetrability of the grout material and quality of the barrier (Stille et al. 2012).

Fortunately, Eq. (4.19) theoretically only requires two measured values (a_m and σ) which, depending on the fracture size, can be derived from outcrop/core images, thin sections or optical high resolution borehole logging tools. Since aperture estimation appears to be challenging for 'needle fractures', the applicability of Carman-Kozeny (CK) equation (Eq. 4.13) represents a practical alternative to deduce the theoretical hydraulic aperture (a_h) from the calculated permeability (K). By applying Eq. (4.14) to derive Kozeny's coefficient (c), there remain two parameters, where the porosity n and the specific surface area (S) could be obtained by preparing dyed thin-sections and applying the methods proposed by Rabbani et al. (2014; 2016), Rabbani and Ayatollahi (2015) and Rabbani and Jamshidi (2014) and

references therein. However, applicable thin-sections have to represent the unimpaired morphology of the partially sealed fracture, which could be a challenging task during preparation. Furthermore, the proposed evaluation methods may have to be re-examined for 'needle fracture' patterns since these methods were developed for porous rocks.

4.4 Conclusions

A numerical study is presented to determine hydraulic properties for fractures under two types of fracture sealing, which both typically occur in natural rock fractures: needle and compact quartz growth. The simulations are performed by applying a phase-field model of syntaxial and idiomorphic quartz growth into a fluid flow simulation solving the Navier-Stokes equation. The results provide insights into different sealing stages and consequent changes in permeability. The main conclusions of this study can be summarized as follows:

(1) Permeabilities of partially sealed fracture significantly depend on the crystal growth behavior evolving in the fracture voids. Due to the significant impact on the tortuosity of fracture flow - especially at lower sealing stages and even at identical relative sealing - the drop of fracture permeability K is particularly pronounced for the 'needle fracture' compared to the 'compact fracture'.

(2) The simulations indicate that fracture flow in 'compact fractures' most widely is governed by the cubic law. Fluid flow in 'needle fractures' can be described by both, the cubic law and the Kozeny-Carman equation. The latter is caused by the capillary tubes structures made up by the isolated crystal growth that resembles a porous medium.

(3) Typical structures evolving in the 'needle fracture' are crystal bridges. Results of this study provide further indications how such bridges in natural fractures can affect fluid flow behavior in the case of geoscientific utilization.

(4) A semi-theoretical equation (Eq. 4.19) is successfully introduced describing the relationship between mean (a_m) and hydraulic aperture (a_h) as well as relative roughness (σ/a_m). In order to account for different crystal habits a geometry factor α is introduced being 2.5 for needle quartz and 1.0 for compact quartz. This geometry factor α appears to be related to the tortuosity of the fluid flow paths.

(5) In contrast to most common a_h-a_m-relationships the new equation reveals a larger range of validity concerning the roughness of the 'needle' ($\sigma/a_m = 0–2.4$) and the 'compact fractures' ($\sigma/a_m = 0–1.8$). However, previous equations were validated for mechanically-induced

fractures. Reversely, the new equation still has to be validated or falsified for other fracture types.

(6) Eq. (4.19) can be a more effective alternative to common hydraulic aperture models to achieve the successful realization of rock engineering projects in partially sealed fractured rocks.

In this study, only pure quartz sealing within a fracture idealized by two parallel plates is considered. Future studies are encouraged to conduct simulations starting with rough initial fracture surfaces or adapt the model to additional prominent fracture sealings such as calcite or sulphide mineralization (Nelson 2001). Furthermore, growth rates along the fracture can be heterogeneous depending on the flow velocity and/or coupled sealing/dissolution processes due to concentration gradients and will be taken into account in future work. Supplementary, the coupling of *in situ* imaging techniques such as X-ray computed tomography as presented by Tokan-Lawal et al. (2017) and core-scale natural sealing structures (e.g. as presented by Fischer et al. (2003)) can provide additional insights into naturally grown sealing geometries.

Acknowledgement

This study was supported by the Helmholtz Association of German Research Centres (HGF) portfolio project "Geoenergy" and is part of the comprised reservoir engineering cluster. In addition, we acknowledge the postdoctoral grants to Jens-Oliver Schwarz and Frank Wendler, which was funded within the framework of DGMK (German Society for Petroleum and Coal Science and Technology) research project 718 "Mineral Vein Dynamics Modelling". The latter is funded by the companies ExxonMobil Production Deutschland GmbH, ENGIE E&P Deutschland GmbH, DEA Deutsche Erdoel AG and Wintershall Holding GmbH, within the basic research program of the BVEG (Bundesverband Erdgas, Erdöl und Geoenergie e.V.). In particular, we thank Math2Market for providing the GeoDict software package for fluid flow simulations. Finally, we also thank both anonymous reviewers for their helpful comments and suggestions that improved this manuscript.

Chapter 5

Synthesis

5.1 Conclusions

Fractured reservoir simulations, which are often based on a discrete fracture network (DFN) model, typically rely on one-dimensional, but representative fracture properties. Hence, fundamental understanding of coupled fracture processes but also practical and efficient methods are required to define these parameters, particularly for geothermal energy production. Both of these requirements are addressed in this thesis and findings are discussed hereafter separately:

Methods

In the first study, a novel Fast Fourier Transform (FFT)-based web application is introduced and validated, which considers both elastic and elastic-plastic contact deformation to reproduce normal closure based on high-resolution fracture surface scans. Simulations are validated for uniaxial laboratory tests on a granodiorite fracture with applied stresses between 0.25 and 10 MPa. In comparison with the experimental results, a root-mean squared error (RMSE) of about 9 µm indicates the higher validity of the elastic-plastic model. The RMSE of the elastic model is slightly higher (11 µm) and indicates more pronounced deviations from the experimental results (up to 17 %) with increasing normal stress. Errors of the elastic-plastic model can be related to experimental and surface scan uncertainties, to the mineralogical heterogeneity of the fracture material and to minor sliding or shearing during early fracture mating. Although the elastic-plastic model shows a lower RMSE value, no significant differences between the general normal closures and mean apertures are found for both the elastic and elastic-plastic models, indicating a general resistance of hard granodiorite fractures to significant non-elastic deformation at the applied stresses. However, stress distributions along the fracture emphasize that the elastic-plastic model is more appropriate particularly for subsequent fluid flow or transport studies, which rely on the resulting local aperture and contact patterns that differ from the elastic model. The application of the elastic-plastic model is of particular importance when studying softer rocks such as many evaporites (e.g. limestones, anhydrite and halite) or mudrocks (e.g. claystones and shales). In this context, study 1 reveals that the performance of the models relies mostly on the appropriate choice of the governing material properties represented by the Young's modulus and the indentation hardness. Hence, the introduced web application represents a useful, fast, free and easy-to-apply toolbox to simulate stress-dependent normal closure of fractures and also provides two-

dimensional output files such as pressure or aperture distributions for subsequent fracture studies. Additionally, the web application is also able to consider circular fractures as considered in this study and thus is also applicable on drilling core scans. In comparison to interpenetration models, which are often used for fast normally closed fractures, the web application incorporates physically more exact contact mechanics and their impact on neighboring regions.

For fracture analyses, which do not only rely on normal closure problems, a practical approach is proposed in the second study. This approach allows a coupling of fluid flow simulations with *in situ* images of fractured rocks by using common medical X-ray computed tomography (CT) data. Validating this approach with CT scans of a fractured rock sample under loading/unloading conditions shows that the proposed method is useful to approximate experimentally derived flow through results. However, this new approach merely indicates the expected hysteretic curve shape of the stress-dependent fracture permeability, for the following reasons: (1) Calibration errors, which result from the choice of an appropriate threshold value defining the density of the non-fractured matrix material, where only 1 % deviation can cause permeability differences by up to 2.6 orders of magnitude. (2) Additionally, this material parameter presumes a perfectly homogeneous matrix, instead of compositional heterogeneities such as pores or potassium-enriched minerals, which implicates local deviations. (3) The major reason for the deviations from the ideal hysteretic behaviour can be ascribed to the coarse resolution ($0.5 \times 0.5 \times 1.0$ mm³) of the CT scans, which is not able to capture sub-voxel features that significantly contribute to fracture flow and contact mechanical changes. Nevertheless, comparison with an analogous CT-based simulation approach reveals that the presented alternative approach is competitive and theoretically less time-consuming. However, it is applicable only to tightly-closed fractures with very small apertures (< 35 µm).

The third study sheds light onto the geometry-related hydraulic behaviour of partially sealed fractures, which up-to-now is one of the great unknown in fractured rock research. Hydrothermally induced quartz growth is simulated by using a phase field model and then Navier-Stokes flow simulations are performed to reveal laminar flow behaviour for different stages of the sealing process and for two types of typical fracture sealing. This method provides comprehensive information about the local and general hydraulics of sealing fractures, which are discussed in the following subchapter. Since this method is also computationally expensive and elaborate, a semi-theoretical equation to estimate the hydraulic aperture a_h of partially sealed fractures is introduced based on the simulation results. This novel equation is based only on the mechanical aperture a_m and relative roughness σ/a_m and a geometry factor α, which accounts for different crystal habits. In this study, α is found to be 2.5 for elongated (needle) quartz structures and 1.0 for more compact quartz crystals. In contrast to other existing a_h-a_m-relationships, this equation explicitly applies for sealing fractures since it accounts for the internal

crystal geometries and also works for sealing structure specific relative roughnesses > 1. Hence, this equation provides a more effective alternative to define hydraulic input parameters for numerical and analytical fractured rock models.

Fracture properties

Based on the web application results in study 1, it is shown that contact areas of the hard granodiorite fracture even at normal stresses of 10 MPa represent less than 2 % of the total fracture area, which agrees well with experimental observations from literature. Larger experimentally derived contact areas (> 10 %), which are often reported in literature, are commonly affected by scale-dependent limitations of the measurement methods. Resulting contacts typically are microscopically small and locally clustered features, which do however still offer open interspaces. How the contacts behave, typically depends on the hardness of the fracture surface. In the web application, this hardness is represented by the relative hardness (ratio of the indentation hardness and the effective Young's modulus), which is around 0.14 for the granodiorite fracture and other granitic rocks. Softer rocks such as many evaporites or mudstone should have hardness values significantly below 0.1. Furthermore, it is shown that aperture distributions become more right skewed with increasing stresses due to the heterogeneous local displacements, which are related to the initial aperture size. In this context, absolute local displacements are more pronounced for initially larger apertures. However, relative aperture changes are more heterogeneous for initially smaller apertures, which are affected by adjacent contact deformations.

Fluid flow simulations in study 2 indicate that significant flow channeling also occurs in smooth and tightly-closed fractures. In such fractures fluid flow is governed by few preferred flow channels with less pronounced tortuosity. Some of these channels can be closed temporarily or permanently under loading/unloading conditions. These flow channels contribute significantly to the overall core permeability (between 10^{-15} and 10^{-13} m²), while the matrix permeability is significantly lower (5×10^{-19} m²). However, simulation results indicate that fracture geometries below the CT resolution significantly contribute to the stress-dependent permeability hysteresis. This finding is in line with Study 1, which shows that stress-dependent contact evolution and local closure significantly depends on the small-scale roughness of the fracture.

The phase-field model for hydrothermally induced quartz growth in study 3 shows that fluid flow significantly depends on the crystal habit evolving in partially mineralized (or sealing) fractures. Especially at a low relative sealing, the presence of elongated ('needle') crystals facilitates more pronounced decrease in fracture permeability (e.g. 20 % of the initial permeability at 20 % sealing) as compared to the presence of more compact mineral habits (e.g. 40 % of the initial permeability at 20 %

sealing). It is shown that isolated growth of 'needle quartz' fractures facilitates an early development of crystal bridges. These bridges form pronounced barriers for fluid flow, which contribute to a more pronounced tortuosity of the intrinsic flow channels and reduces fracture permeability. In this context, the growth of 'needle quartz' facilitates the formation of tubes structures resembling a porous media so that fracture flow can be described by the Kozeny-Carman equation for porous media. In contrast, fluid flow in 'compact quartz' fractures is governed only by the cubic law, which is also valid for 'needle quartz' fractures as long as the newly derived a_h-a_m-relationship is applied.

In the present thesis, three valuable and efficient approaches are introduced to solve coupled problems in fractured rocks and to provide useful input parameters for discrete fracture network (DFN) models. Particularly, for industrial purposes easy-to-apply methods are required, which is also considered by the new approaches:

- The free web application-based numerical contact model (study 1) allows for the fast and physically exact calculation of normal closure and only requires reliable material parameters and surface scans derived from customary scan devices.

- The approach proposed in study 2 indicates applicability for tightly-closed fractures, which for example revealed significant chemical alteration along contacts. Such fractures require non-destructive methods to capture their interior, which theoretically can be utilized in many local hospitals, where medical X-ray CT devices are basic equipment.

- The semi-empirical equation presented in study 3 allows the user to estimate the hydraulic aperture for sealing fractures with geometries similar to the ones considered in this study. This method also only requires a few input parameters, which can be approximated for real fractures by using thin sections or image log analyses.

5.2 Perspective and Outlook

One of the main limitations of the current study is that the introduced approaches are only applied to a limited number of fractures and on the laboratory scale. However, flow in fractured rock masses not uncommonly is governed by larger fractures up to the (multiple) meter scale (e.g. Blum et al. 2007; Müller et al. 2010; Zeeb et al. 2010). Hence, a comprehensive multi-step fracture evaluation approach is required, which contains:

(1) The mapping and evaluation of analogous fracture networks.

(2) Finding the necessary input parameters based on the detection, evaluation and (if necessary) the upscaling of single surface data.

(3) Combining information gained from (1) and (2) into a representative discrete fracture network (DFN) model for further numerical treatment.

While there are some useful applications concerning (1) (e.g. Zeeb et al. 2013a; Healy et al. 2017) and (3) (e.g. Blum et al. 2005; Alghalandis 2017), an appropriate application for (2) is still missing. This gap could be closed by adopting a single fracture evaluation approach, which is split into three parts:

(1) **Fracture mining:** Since fractures and their geometry typically depend on the tectonic history of the target area, field data of analogous fractures derived from outcrops are the basis for fracture analyses. Non-contacting surface scanners have been proven to be a useful tool to capture the full fracture roughness even on field-scale (e.g. Candela et al. 2009; Tatone and Grasselli 2012a), but often lack flexibility due to their size and their complex configuration requiring a tripods, a laptop and a generator. First tests performed with a portable (handheld) 3D scanner (Go!SCAN 3D^{TM}, Creaform GmbH), indicate a more flexible alternative to scan fracture surfaces in the field although powerful energy sources and processing equipment are required. A further alternative could be open-source photogrammetry based on customary digital or smartphone cameras and open-source photogrammetry software such as VisualSFM as utilized by Wernecke and Marsch (2015). The authors found that this approach is able to reproduce the large-scale roughness (or general topography), but in contrast to scanning devices as the one used in study 1 cannot capture small-scale roughness. One solution to this issue could be a local downscaling after image processing based on the statistical (or fractal) properties of the surfaces by using fractal or multifractal interpolation methods (e.g. Sun 2012a, b).

(2) **Fracture evaluation:** The primary problem involving fracture evaluation is that fracture scans in nature often only provide information of a single surface of the complete fracture, which is an issue particularly for shearing fractures, which can reveal a significant hydraulic anisotropy. For shearing fractures, it is shown that hydraulic anisotropy is partially related to the statistical properties of the single surfaces and resulting aperture distributions (Matsuki et al. 2006). In order to solve this issue, Matsuki et al. (2006) apply scans of a single tensile fracture (1.0×0.2 m²), where the scanned surfaces are shifted computationally to represent a shearing fracture. This approach is often assumed to be equivalent to real shear fractures (Watanabe et al. 2009), but neglects the different underlying breakage mechanisms (Morgan et al. 2013; Vogler et al. 2017). An open question still remains, whether there is any correlation between scans of real shearing (mode II and III) fracture surfaces (e.g. Vogler et al. 2016a, 2017) and resulting

aperture distributions. Finding such correlations can be used to generate representative (and upscaled) 2D aperture distributions, which also reflect the actual hydraulic anisotropy. Up-to-now shearing-induced anisotropy is only considered for synthetic fracture surfaces (Candela et al. 2009). Existing codes, which directly generate synthetic aperture distributions, typically only reproduce isotropic fractures (Nolte and Pyrak-Nolte 1991; Co and Horne 2015). A useful tool to investigate the statistical fracture properties could be the introduced web application (study 1), which is also able to evaluate the direction-dependent statistical properties of fracture scans and aperture fields. Finding new methods to produce synthetic (anisotropic) aperture distributions would also facilitate multi-fracture analyses in the subsequent fracture processing step to evaluate the range of the simulated fracture property.

(3) **Fracture processing:** Multiple (natural or synthetic) fracture geometries can be the basis for subsequent Monte-Carlo simulations assessing the impact of the different surface morphologies on required DFN input parameters such as hydraulic and mechanical aperture or the normal stiffness. In order to solve that issue, an advanced version of the source-code used in the web application in study 1 can be useful. As shown in previous studies this approach could be enhanced by adding subsequent fracture unloading (Li et al. 2015), compositional fracture surface heterogeneities (Wu and Sharma 2017), local cubic law (LCL) simulations (Lang et al. 2015, 2016; Wu and Sharma 2017) or the modified LCL (Wang et al. 2015) and reactive transport approaches pressure dissolution and precipitation of quartz (Lang et al. 2015, 2016) or calcite (Crandall et al. 2014). Furthermore, multi-phase flow models such as the invasion-percolation approach could be implemented to estimate the relative permeability or capillary pressure-saturation relationships, which are also important for many other geoscientific issues such as carbon sequestration, hydrocarbon recovery or contaminations with nonaqueous phase liquids (NAPLs) (Yang et al. 2013). The aim should be a “Swiss Army knife” providing a variety of fracture properties for different purposes.

Since the first subitem (fracture mining) is not always possible due to missing outcrops or measurement techniques, a comprehensive database, which summarizes analogous fractures and their properties, could be supportive for many geoscientific projects. In the last years, a vast number of fracture studies have been published in literature. In such a database, these data could be compiled according to the fracture type (e.g. tensile, shearing fracture), scale, rock type and locality, quantitative and qualitative roughness parameters (cf. Li and Zhang 2015), (universal and direction-dependent) statistical properties (cf. Candela et al. 2009), grain sizes affecting resulting topography (e.g. Ogilvie et al. 2006; Chen et al. 2017) and mechanical properties such as the Young’s modulus of the rock and its hardness. Such a database would not only provide an uncomplicated procedure to acquire analogous

fracture data to generate potential synthetic surfaces, but also could be helpful to better understand generic relationships. However, most of the available rock fracture studies focus on a few rock types such as different granites, sandstones, shales and micritic limestones. In order to comprise the full geological spectrum this list could be enhanced by independent fracture studies including oolitic limestones such as the Jurassic Hauptrogenstein and conglomerates of the Rotliegend, which both represent potential source rocks for geothermal energy production in Germany (Stober and Jodocy 2009; Zimmermann and Reinicke 2010). Furthermore, only less is known about quantitative indentation hardness values (Vickers or Knoop method) of the different rock types as required for elastic-plastic normal closure simulations. Such parameter studies can also comprise investigations of correlations with portable material testing methods such as the Schmidt rebound hammer, Equotip ball rebound tester, Duroscopes or the needle penetrometer (e.g. Viles et al. 2011; Ulusay and Erguler 2012).

One major shortcoming of this thesis is that all the investigated fracture processes are based on the assumption that fluid flow most widely occurs in the rock fractures and under laminar flow conditions. However, in reality flow and particularly transport processes can be affected by advection, dispersion, adsorption, matrix diffusion and several chemical reactions (Bodin et al. 2003; Huber et al. 2012; Zhao et al. 2012). Hence, combined positron emission tomography and computed tomography (PET/CT) should be used to investigate fracture-matrix interactions and transport behaviour. While CTs image the solid medium, PETs image fracture and matrix flow, where radionuclides act as a tracer (e.g. Kulenkampff et al. 2008; Fernø et al. 2015). PETs allow the investigation of potential stress-dependent fracture-matrix interactions as numerically investigated by Zhao et al. (2012) and allow to consider rock heterogeneity effects such as lamination or intersecting fractures. Based on the PET data and the recommendations presented in study 2, new CT-based model approaches can be developed to numerically reproduce transport processes in fractured-porous media.

Since CTs image density contrasts, this technique could be additionally used to reproduce reactive transport phenomena such as the precipitation of dense galena minerals, which are also observed in sealing fractures of the Buntsandstein in the Upper Rhine Graben (Vidal et al. 2015). In order to ensure distinct density contrasts due to local mineral precipitation, monomineralic porous quartz ceramics resembling sandstones (e.g. Casalino et al. 2005) can be used for first test experiments.

Concerning study 3 further phase-field models and corresponding crystal growth experiments are required for other common fracture sealings such as calcite, barite or gypsum. Furthermore, simulations in study 3 are performed for an idealized parallel plate fracture. Crystal growth simulations between two rough surfaces as presented by Ankit et al. (2015) could refine the semi-empirical equation. Based on these simulations, it could also be further pursued to find out if the recent equation

is applicable for a locally corrected local cubic law in (rough) sealing fractures. Last but not least, the novel equation has to be validated or falsified for shearing and tensile fractures.

Acknowledgement

The thesis was made possible by so many people who supported me and I have to express my gratitude to so many people. I would like to thank…

… my supervisor Prof. Dr. Philipp Blum for giving me the opportunity to do a PhD, for his excellent mentoring during the course of my thesis, for giving me the freedom to develop my own ideas, for opening my eyes for interdisciplinarity, for his patience and motivation during "periods of drought", and of course for the endless, intensive and prolific scientific (and sometimes not-so-scientific) discussions. There are so many further things I have to thank for, but I do not find the right words. So I keep it as you taught me (maybe for the first time) "short and simple".

…Dr. Jens-Oliver Schwarz and Dr. Frieder Enzmann for introducing me into the world of pore-scale tomography and computational fluid dynamics, and of course for sharing their time and profound knowledge during my visits in Mainz.

…Prof. Dr. Lars Pastewka for his uncomplicated willingness to collaborate, for the immediate fixing of bugs in the web app and the countless instructive discussions.

…Prof. Dr. Florian Amann and especially Dr. Daniel Vogler for their uncomplicated willingness to collaborate, the instructive visit in Zurich and for sharing their profound knowledge.

…Prof. Sally Benson and in particular Dr. Da Huo for their collaboration, for providing the experimental data, the instructive visit in Stanford and for answering so many questions.

…Dr. Frank Wendler for the many fruitful discussions about his fancy phase-field models.

…Prof. Dr. Christoph Butscher for the countless discussions during his time in Karlsruhe, for sharing his scientific experience and for his uncomplicated willingness to be the second reviewer.

… The Helmholtz-Gemeinschaft Deutscher Forschungszentren (HGF) for funding my PhD within the framework the portfolio project "Geoenergy".

… The Open Access Publishing Fund of Karlsruhe Institute of Technology for funding my Solid Earth article.

…Dr. Susanne Benz, M.Sc. Anna Ender, Dr. Zhao Chen and especially Dr. Julian Xanke for the comprehensive support during the end of my PhD.

…M.Sc. Paul Fleuchaus, Dipl.-Geol. Michael Augenstein and M.Sc. Markus Merk for the great time in the office.

…Dipl.-Ing. Thomas Mutschler and Dr. Hagen Steger for sharing profound and never-ending knowledge.

…Dr. Valentin Wagner for introducing me into the world of MATLAB.

…Prof. Dr. Frank Schilling, Prof. Dr. Thomas Kohl and Prof. Dr. Ingrid Stober for the nice talks on the corridor, in the office or during conferences/workshops, and for inspiring me even before I started my PhD. I am honest to have you in my board of examiners.

…the engineering geology, hydrogeology and geothermal working groups for the enjoyable collaboration and the nice scientific and not-so-scientific discussions. The same applies for all the people of other institutes, divisions of the AGW and universities that took part during my PhD.

…Ines Knoch, Petra Linder, Nicole Suteu and Sibylle Grünenwald for supporting me with the administrative stuff.

…Sarah Siegrist, Helena Young and Giorgia Lucianetti for the language editing of chapter one and five.

… Dr. Horst Kreuter, Dr. John Reinecker, Dr. Michael Kraml and Dr. René Grobe and my “besties” for encouraging me to do my PhD.

… Finally, I would like to express my deepest gratitude to my entire family, my siblings and especially to my beloved parents. All my life, you have been my greatest supporters, motivators and my safe haven during stormy periods. You are the best parents a son can wish for. *Einfach unendlich viel Dank für alles* ♥!

Declaration of Authorship

Study 1

Citation: *Kling T, Vogler D, Pastewka L, Amann F, Blum P: Numerical simulations of contact mechanics in a granodiorite fracture. Rock Mechanics and Rock Engineering [under review].*

Declaration of authorship: Daniel Vogler (DV) and Florian Amann (FA) prepared and executed the uniaxial laboratory tests. Lars Pastewka (LP) developed and improved the web app-based numerical model with the help of TK, who repeatedly tested the app for plausibility and functionality. TK did the parameter studies, accomplished the numerical models and analysed the Gigabytes of resulting 1D and 2D data by developing MATLAB codes in consultation with LP and PB. Experimental and numerical results were evaluated in consultation with LP, DV, FA and PB. TK wrote the manuscript. LP significantly improved the manuscript in the methods part, where the theory behind the web application is described. The final manuscript was reviewed by all authors. TK is going to handle the review process.

Study 2

Citation: *Kling T, Huo D, Schwarz JO, Enzmann F, Benson S, Blum P (2016): Simulating stress-dependent fluid flow in a fractured core sample using real-time X-ray CT data. Solid Earth, 7:1109-1124, doi:10.5194/se-7-1109-2016.*

Declaration of authorship: Da Huo (DH) and Sally Benson (SB) prepared and executed the flow-through experiments and CT scans. Jens-Oliver Schwarz (JOS) and Frieder Enzmann (FE) implemented an initial MATLAB code to post-process the raw CT data. This code subsequently was adjusted with the help of Tobias Kling (TK). 3D image reconstruction of CT data and simulated flow patterns was performed by TK and FE. TK accomplished and evaluated the numerical simulations in consultation with FE, PB, DH and SB. TK wrote the manuscript and accompanied it through the review process. The final manuscript was reviewed by all authors.

Study 3

Citation: *Kling T, Schwarz J-O, Wendler F, Enzmann F, Blum P (2017): Fracture flow due to hydrothermally induced quartz growth. Advances in Water Resources, 107:93-107, doi:10.1016/j.advwatres.2017.06.011.*

Declaration of authorship: Frank Wendler (FW) developed the phase-field models (PFMs), did the marching cubes analyses and provided the 3D visualization of the PFMs. Jens-Oliver Schwarz (JOS) and Frieder Enzmann developed the fluid flow simulations with GeoDict and provided the 2D and 3D visualizations of simulated fluid flow patterns. The newly derived equation and its derivation were established by FW and Tobias Kling (TK). TK reanalyzed, restructured and evaluated the results in consultation with FW and JOS. TK wrote the manuscript, whereby JOS and FW provided significant contributions to the methods part. PB significantly improved the manuscript. TK accompanied it through the review process. The final manuscript was reviewed by all authors.

References

Agemar T, Hese F, Moeck I, Stober I (2017) Kriterienkatalog für die Erfassung tiefreichender Störungen und ihrer geothermischen Nutzbarkeit in Deutschland. Z Dtsch Ges Für Geowiss ZDGG 285–300. doi: 10.1127/zdgg/2017/0084

Akarapu S, Sharp T, Robbins MO (2011) Stiffness of contacts between rough surfaces. Phys Rev Lett 106:204301. doi: 10.1103/PhysRevLett.106.204301

Akin S, Kovscek AR (2003) Computed tomography in petroleum engineering research. Geol Soc Lond Spec Publ 215:23–38. doi: 10.1144/gsl.sp.2003.215.01.03

Alghalandis YF (2017) ADFNE: Open source software for discrete fracture network engineering, two and three dimensional applications. Comput Geosci 102:1–11. doi: 10.1016/j.cageo.2017.02.002

Almqvist A, Campañá C, Prodanov N, Persson BNJ (2011) Interfacial separation between elastic solids with randomly rough surfaces: Comparison between theory and numerical techniques. J Mech Phys Solids 59:2355–2369. doi: 10.1016/j.jmps.2011.08.004

Almqvist A, Sahlin F, Larsson R, Glavatskih S (2007) On the dry elasto-plastic contact of nominally flat surfaces. Tribol Int 40:574–579. doi: 10.1016/j.triboint.2005.11.008

Al-Yaarubi AH, Pain CC, Grattoni CA, Zimmerman RW (2005) Navier-Stokes simulations of fluid flow through a rock fracture. In: Faybishenko B, Witherspoon PA (eds) Proceedings of the 2nd International Symposium on Dynamics of Fluids and Transport in Fractured Rock. American Geophysical Union, pp 201–205

Amadei B, Illangasekare T (1994) A mathematical model for flow and solute transport in non-homogeneous rock fractures. Int J Rock Mech Min Sci Geomech Abstr 31:719–731. doi: 10.1016/0148-9062(94)90011-6

Amaral P, Cruz Fernandes J, Frisa A, et al (2000) Evaluation of the workability by means of diamond tools of a series of portuguese commercial granites. In: Convegno su "Le cave di Pietre Ornamenteli." Associazone Georisorse e Ambiente, Torino (Italy), pp 323–329

Amba-rao CL (1969) Fourier transform methods in elasticity problems and an application. J Frankl Inst 287:241–249. doi: 10.1016/0016-0032(69)90100-8

André L, Rabemanana V, Vuataz F-D (2006) Influence of water–rock interactions on fracture permeability of the deep reservoir at Soultz-sous-Forêts, France. Geothermics 35:507–531. doi: 10.1016/j.geothermics.2006.09.006

Ankit K, Nestler B, Selzer M, Reichardt M (2013) Phase-field study of grain boundary tracking behavior in crack-seal microstructures. Contrib Mineral Petrol 166:1709–1723. doi: 10.1007/s00410-013-0950-x

Ankit K, Selzer M, Hilgers C, Nestler B (2015a) Phase-field modeling of fracture cementation processes in 3-D. J Pet Sci Res 4:79–96. doi: 10.12783/jpsr.2015.0402.04

Ankit K, Urai JL, Nestler B (2015b) Microstructural evolution in bitaxial crack-seal veins: A phase-field study. J Geophys Res Solid Earth 120:3096–3118. doi: 10.1002/2015jb011934

Ayachit U (2015) The Paraview Guide: A parallel visualization application

Aydin A, Basu A (2005) The Schmidt hammer in rock material characterization. Eng Geol 81:1–14. doi: 10.1016/j.enggeo.2005.06.006

Babadagli T, Ren X, Develi K (2015) Effects of fractal surface roughness and lithology on single and multiphase flow in a single fracture: An experimental investigation. Int J Multiph Flow 68:40–58. doi: 10.1016/j.ijmultiphaseflow.2014.10.004

Baisch S, Vörös R, Rothert E, et al (2010) A numerical model for fluid injection induced seismicity at Soultz-sous-Forêts. Int J Rock Mech Min Sci 47:405–413. doi: 10.1016/j.ijrmms.2009.10.001

Bandis SC, Lumsden AC, Barton NR (1983) Fundamentals of rock joint deformation. Int J Rock Mech Min Sci 20:249–268. doi: 10.1016/0148-9062(83)90595-8

Barbot S, Fialko Y (2010) Fourier-domain Green's function for an elastic semi-infinite solid under gravity, with applications to earthquake and volcano deformation. Geophys J Int 182:568–582. doi: 10.1111/j.1365-246X.2010.04655.x

Barton CC (1995) Fractal analysis of scaling and spatial clustering of fractures. In: Fractals in the Earth Sciences. Springer, Boston, MA, pp 141–178

Barton N, Bandis S, Bakhtar K (1985) Strength, deformation and conductivity coupling of rock joints. Int J Rock Mech Min Sci Geomech Abstr 22:121–140. doi: 10.1016/0148-9062(85)93227-9

Barton N, de Quadros EF (1997) Joint aperture and roughness in the prediction of flow and groutability of rock masses. Int J Rock Mech Min Sci 34:252(e1-e14). doi: 10.1016/S1365-1609(97)00081-6

Belem T, Homand-Etienne F, Souley M (2000) Quantitative Parameters for Rock Joint Surface Roughness. Rock Mech Rock Eng 33:217–242. doi: 10.1007/s006030070001

Benson SM, Daggett JS, Iglesias E, et al (1987) Analysis of thermally induced permeability enhancement in geothermal injection wells. In: Proceedings of the 12th workshop on Geothermal Reservoir Engineering. Stanford, California (United States), pp 57–65

Benz M, Rosenberg KJ, Kramer EJ, Israelachvili JN (2006) The deformation and adhesion of randomly rough and patterned surfaces. J Phys Chem B 110:11884–11893. doi: 10.1021/jp0602880

Berkowitz B (2002) Characterizing flow and transport in fractured geological media: A review. Adv Water Resour 25:861–884. doi: 10.1016/S0309-1708(02)00042-8

Bernabe Y (1986a) The effective pressure law for permeability in Chelmsford granite and Barre granite. Int J Rock Mech Min Sci Geomech Abstr 23:267–275. doi: 10.1016/0148-9062(86)90972-1

Bernabe Y (1986b) Pore volume and transport properties changes during pressure cycling of several crystalline rocks. Mech Mater 5:235–249. doi: 10.1016/0167-6636(86)90021-9

Bertels SP, DiCarlo DA, Blunt MJ (2001) Measurement of aperture distribution, capillary pressure, relative permeability, and in situ saturation in a rock fracture using computed tomography scanning. Water Resour Res 37:649–662. doi: 10.1029/2000wr900316

Berthoud P, Baumberger T (1998) Shear stiffness of a solid–solid multicontact interface. Proc R Soc Lond Math Phys Eng Sci 454:1615–1634. doi: 10.1098/rspa.1998.0223

Blum P, Mackay R, Riley MS (2009) Stochastic simulations of regional scale advective transport in fractured rock masses using block upscaled hydro-mechanical rock property data. J Hydrol 369:318–325. doi: 10.1016/j.jhydrol.2009.02.009

Blum P, Mackay R, Riley MS, Knight JL (2005) Performance assessment of a nuclear waste repository: Upscaling coupled hydro-mechanical properties for far-field transport analysis. Int J Rock Mech Min Sci 42:781–792. doi: 10.1016/j.ijrmms.2005.03.015

Blum P, Mackay R, Riley MS, Knight JL (2007) Hydraulic modelling and the evaluation of the representative elementary volume (REV) in fractured rock. Grundwasser 12:48–65. doi: 10.1007/s00767-007-0017-x

BMU (2007) Tiefe Geothermie in Deutschland. Bundesministerium für Umwelt, Naturschutz und Reaktorsicherheit (BMU), Berlin

BNetzA (2017) SMARD (Strommarktdaten-Plattform der Bundesnetzagentur). In: www.smard.de. https://www.smard.de/blueprint/servlet/page/home/marktdaten/78. Accessed 7 Sep 2017

Bodin J, Delay F, de Marsily G (2003) Solute transport in a single fracture with negligible matrix permeability: 1. fundamental mechanisms. Hydrogeol J 11:418–433. doi: 10.1007/s10040-003-0268-2

Bodvarsson GS, Benson SM, Sigurdsson O, et al (1984) The Krafla geothermal field, Iceland: 1. Analysis of well test data. Water Resour Res 20:1515–1530. doi: 10.1029/WR020i011p01515

Bond AE, Bruský I, Cao T, et al (2017) A synthesis of approaches for modelling coupled thermal–hydraulic–mechanical–chemical processes in a single novaculite fracture experiment. Environ Earth Sci 76:12. doi: 10.1007/s12665-016-6326-6

Bons PD (2001) Development of crystal morphology during unitaxial growth in a progressively widening vein: I. The numerical model. J Struct Geol 23:865–872. doi: 10.1016/S0191-8141(00)00159-0

Bons PD, Elburg MA, Gomez-Rivas E (2012) A review of the formation of tectonic veins and their microstructures. J Struct Geol 43:33–62. doi: 10.1016/j.jsg.2012.07.005

Boussinesq J (1868) Mémoire sur l'influence des Frottements dans les Mouvements Réguliers des Fluids. J Mathématiques Pures Appliquées 2:377–424

Brace WF, Kohlstedt DL (1980) Limits on lithospheric stress imposed by laboratory experiments. J Geophys Res Solid Earth 85:6248–6252. doi: 10.1029/JB085iB11p06248

Brodsky EE, Gilchrist JJ, Sagy A, Collettini C (2011) Faults smooth gradually as a function of slip. Earth Planet Sci Lett 302:185–193. doi: 10.1016/j.epsl.2010.12.010

Brown SR (1995) Simple mathematical model of a rough fracture. J Geophys Res Solid Earth 100:5941–5952. doi: 10.1029/94jb03262

Brown SR (1987) Fluid flow through rock joints: The effect of surface roughness. J Geophys Res Solid Earth 92:1337–1347. doi: 10.1029/JB092iB02p01337

Brown SR, Scholz CH (1985) Closure of random elastic surfaces in contact. J Geophys Res Solid Earth 90:5531–5545. doi: 10.1029/JB090iB07p05531

Brown SR, Scholz CH (1986) Closure of rock joints. J Geophys Res Solid Earth 91:4939–4948. doi: 10.1029/JB091iB05p04939

Brush DJ, Thomson NR (2003) Fluid flow in synthetic rough-walled fractures: Navier-Stokes, Stokes, and local cubic law simulations. Water Resour Res 39:1085. doi: 10.1029/2002wr001346

Butscher C, Mutschler T, Blum P (2016) Swelling of clay-sulfate rocks: A review of processes and controls. Rock Mech Rock Eng 49:1533–1549. doi: 10.1007/s00603-015-0827-6

Cacace M, Jacquey AB (2017) Flexible parallel implicit modelling of coupled thermal–hydraulic–mechanical processes in fractured rocks. Solid Earth 8:921–941. doi: https://doi.org/10.5194/se-8-921-2017

Campañá C, Müser MH (2006) Practical Green's function approach to the simulation of elastic semi-infinite solids. Phys Rev B 74:075420. doi: 10.1103/PhysRevB.74.075420

Campañá C, Persson BNJ, Müser MH (2011) Transverse and normal interfacial stiffness of solids with randomly rough surfaces. J Phys Condens Matter 23:085001. doi: 10.1088/0953-8984/23/8/085001

Candela T, Renard F, Bouchon M, et al (2009) Characterization of fault roughness at various scales: Implications of three-dimensional high resolution topography measurements. Pure Appl Geophys 166:1817–1851. doi: 10.1007/s00024-009-0521-2

Candela T, Renard F, Klinger Y, et al (2012) Roughness of fault surfaces over nine decades of length scales. J Geophys Res Solid Earth 117:30. doi: 10.1029/2011jb009041

Cardenas MB, Slottke DT, Ketcham RA, Sharp JM (2007) Navier-Stokes flow and transport simulations using real fractures shows heavy tailing due to eddies. Geophys Res Lett 34:L14404. doi: 10.1029/2007GL030545

Carman PC (1937) Fluid flow through granular beds. Trans Inst Chem Eng 15:150–156. doi: 10.1016/S0263-8762(97)80003-2

Casalino G, De Filippis LAC, Ludovico A (2005) A technical note on the mechanical and physical characterization of selective laser sintered sand for rapid casting. J Mater Process Technol 166:1–8. doi: 10.1016/j.jmatprotec.2004.07.102

Ceryan Ş (2008) New chemical weathering indices for estimating the mechanical properties of rocks: A case study from the Kürtün Granodiorite, NE Turkey. Turk J Earth Sci 17:187–207

Ceryan S (2015) New weathering indices for evaluating durability and weathering characterization of crystalline rock material: A case study from NE Turkey. J Afr Earth Sci 103:54–64. doi: 10.1016/j.jafrearsci.2014.12.005

Chen C-Y, Horne RN (2006) Two-phase flow in rough-walled fractures: Experiments and a flow structure model. Water Resour Res 42:W03430/1-17. doi: 10.1029/2004wr003837

Chen L, Kang Q, Viswanathan HS, Tao W-Q (2014) Pore-scale study of dissolution-induced changes in hydrologic properties of rocks with binary minerals. Water Resour Res 50:9343–9365. doi: 10.1002/2014WR015646

Chen Y, Liang W, Lian H, et al (2017) Experimental study on the effect of fracture geometric characteristics on the permeability in deformable rough-walled fractures. Int J Rock Mech Min Sci 98:121–140. doi: 10.1016/j.ijrmms.2017.07.003

Chi G, Xue C (2011) An overview of hydrodynamic studies of mineralization. Geosci Front 2:423–438. doi: 10.1016/j.gsf.2011.05.001

Christie AB, Simpson MP, Brathwaite RL, et al (2007) Epithermal Au-Ag and related deposits of the Hauraki goldfield, Coromandel volcanic zone, New Zealand. Econ Geol 102:785–816. doi: 10.2113/gsecongeo.102.5.785

Ciavarella M, Greenwood JA, Paggi M (2008) Inclusion of "interaction" in the Greenwood and Williamson contact theory. Wear 265:729–734. doi: 10.1016/j.wear.2008.01.019

Clavaud J-B, Maineult A, Zamora M, et al (2008) Permeability anisotropy and its relations with porous medium structure. J Geophys Res Solid Earth 113:B01202. doi: 10.1029/2007jb005004

Co C, Horne R (2015) Artificial rough fracture generation using sequential gaussian simulation (SGSIM): Correlating spatial aperture characteristics to flow channeling behavior. In: 17th Conference of the International Association for Mathematical Geosciences (IAMG). Freiberg (Germany), p 10

Cohen CE, Ding D, Quintard M, Bazin B (2008) From pore scale to wellbore scale: Impact of geometry on wormhole growth in carbonate acidization. Chem Eng Sci 63:3088–3099. doi: 10.1016/j.ces.2008.03.021

Crandall D, Bromhal G, Karpyn ZT (2010) Numerical simulations examining the relationship between wall-roughness and fluid flow in rock fractures. Int J Rock Mech Min Sci 47:784–796. doi: 10.1016/j.ijrmms.2010.03.015

Crandall D, Wen H, Li L, Hakala A (2014) Reactive geochemical flow modeling with CT scanned rock fractures. V01CT24A004. doi: 10.1115/FEDSM2014-21579

Creaform GmbH (2017) Portable 3D Scanners for 3D Scanning | Go!SCAN 3D by Creaform. https://www.creaform3d.com/en/metrology-solutions/handheld-portable-3d-scanner-goscan-3d. Accessed 14 Oct 2017

Curewitz D, Karson JA (1997) Structural settings of hydrothermal outflow: Fracture permeability maintained by fault propagation and interaction. J Volcanol Geotherm Res 79:149–168. doi: 10.1016/S0377-0273(97)00027-9

Cuthbert MO, McMillan LA, Handley-Sidhu S, et al (2013) A field and modeling study of fractured rock permeability reduction using microbially induced calcite precipitation. Environ Sci Technol 47:13637–13643. doi: 10.1021/es402601g

Dannwolf U, Heckelsmüller A, Steiner N, et al (2014) Umweltauswirkungen von Fracking bei der Aufsuchung und Gewinnung von Erdgas insbesondere aus Schiefergaslagerstätten (Teil 2) - Grundwassermonitoringkonzept, Frackingchemikalienkataster, Entsorgung von Flowback, Forschungsstand zur Emissions- und Klimabilanz, induzierte Seismizität, Naturhaushalt, Landschaftsbild und biologische Vielfalt. Bundesministeriums für Umwelt, Naturschutz, Bau und Reaktorsicherheit (BMUB), Dessau-Roßlau (Germany)

Dapp WB, Lücke A, Persson BNJ, Müser MH (2012) Self-affine elastic contacts: Percolation and leakage. Phys Rev Lett 108:244301. doi: 10.1103/PhysRevLett.108.244301

Davy P, Le Goc R, Darcel C, et al (2010) A likely universal model of fracture scaling and its consequence for crustal hydromechanics. J Geophys Res Solid Earth 115:B10411. doi: 10.1029/2009JB007043

De Muynck W, De Belie N, Verstraete W (2010) Microbial carbonate precipitation in construction materials: A review. Ecol Eng 36:118–136. doi: 10.1016/j.ecoleng.2009.02.006

Debbas S, Rumpf H (1966) On the randomness of beds packed with spheres or irregular shaped particles. Chem Eng Sci 21:583–608. doi: 10.1016/0009-2509(66)85072-8

Develi K, Babadagli T (2015) Experimental and visual analysis of single-phase flow through rough fracture replicas. Int J Rock Mech Min Sci 73:139–155. doi: 10.1016/j.ijrmms.2014.11.002

Dicman A, Putra E, Schechter DS (2004) Modeling fluid flow through single fractures using experimental, stochastic and simulation approaches. In: SPE/DOE Symposium on Improved Oil Recovery. Society of Petroleum Engineers, Tulsa, Oklahoma, pp 1–20

Dieterich JH, Kilgore BD (1996) Imaging surface contacts: power law contact distributions and contact stresses in quartz, calcite, glass and acrylic plastic. Tectonophysics 256:219–239. doi: 10.1016/0040-1951(95)00165-4

Dietrich P, Helmig R, Sauter M, et al (eds) (2005) Flow and Transport in Fractured Porous Media. Springer-Verlag, Berlin/Heidelberg

Dijk P, Berkowitz B (1998) Precipitation and dissolution of reactive solutes in fractures. Water Resour Res 34:457–470. doi: 10.1029/97wr03238

Doe T, Lacazette A, Dershowitz W, Knitter C (2013) Evaluating the effect of natural fractures on production from hydraulically fractured wells using discrete fracture network models. In: Unconventional Resources Technology Conference, Denver, Colorado, 12-14 August 2013. Society of Exploration Geophysicists, pp 1679–1688

Dong G, Morrison G, Jaireth S (1995) Quartz textures in epithermal veins, Queensland; classification, origin and implication. Econ Geol 90:1841–1856. doi: 10.2113/gsecongeo.90.6.1841

Dorbath L, Cuenot N, Genter A, Frogneux M (2009) Seismic response of the fractured and faulted granite of Soultz-sous-Forêts (France) to 5 km deep massive water injections. Geophys J Int 177:653–675. doi: 10.1111/j.1365-246X.2009.04030.x

Drazer G, Koplik J (2002) Transport in rough self-affine fractures. Phys Rev E 66:026303. doi: 10.1103/PhysRevE.66.026303

Enerchange (2016) Keine Geothermie für Trebur | Informationsportal Tiefe Geothermie. In: Informationsportal Tiefe Geothermie ITG. http://www.tiefegeothermie.de/news/keine-geothermie-fuer-trebur. Accessed 14 Sep 2017

Evans B (1984) The effect of temperature and impurity content on indentation hardness of quartz. J Geophys Res Solid Earth 89:4213–4222. doi: 10.1029/JB089iB06p04213

Evans KF, Kohl T, Hopkirk R, Rybach L (1992) Modeling of energy production from hot dry rock systems: Project 359 - Final Report. Swiss National Energy Research Fund (NEFF), Zurich (Switzerland)

Faoro I, Elsworth D, Candela T (2015) Evolution of the transport properties of fractures subject to thermally and mechanically activated mineral alteration and redistribution. Geofluids 396–407. doi: 10.1111/gfl.12157

Feng X-T, Chen S, Zhou H (2004) Real-time computerized tomography (CT) experiments on sandstone damage evolution during triaxial compression with chemical corrosion. Int J Rock Mech Min Sci 41:181–192. doi: 10.1016/S1365-1609(03)00059-5

Fernø MA, Gauteplass J, Hauge LP, et al (2015) Combined positron emission tomography and computed tomography to visualize and quantify fluid flow in sedimentary rocks. Water Resour Res 51:7811–7819. doi: 10.1002/2015wr017130

Fischer C, Luttge A (2017) Beyond the conventional understanding of water–rock reactivity. Earth Planet Sci Lett 457:100–105. doi: 10.1016/j.epsl.2016.10.019

Fischer M, Röller K, Küster M, et al (2003) Open fissure mineralization at 2600 m depth in Long Valley exploratory well (California) – insight into the history of the hydrothermal system. J Volcanol Geotherm Res 127:347–363. doi: 10.1016/S0377-0273(03)00176-8

Flemisch B, Berre I, Boon W, et al (2017) Benchmarks for single-phase flow in fractured porous media. http://arxiv.org/abs/1701.01496. Accessed 3 Oct 2017

Fleuchaus P, Blum P (2017) Damage event analysis of vertical ground source heat pump systems in Germany. Geotherm Energy 5:10. doi: 10.1186/s40517-017-0067-y

Fournier RO (1985) The behavior of silica in hydrothermal solution. In: Berger BR, Bethke PM (eds) Geology and geochemistry of epithermal systems. Society of Economic Geologists, El Paso, TX, USA, pp 45–61

Gale J (1982) Assessing the permeability characteristics of fractured rock. Geol Soc Am Spec Pap 189:163–182. doi: 10.1130/SPE189-p163

Gale JFW, Lander RH, Reed RM, Laubach SE (2010) Modeling fracture porosity evolution in dolostone. J Struct Geol 32:1201–1211. doi: 10.1016/j.jsg.2009.04.018

Gangi AF (1978) Variation of whole and fractured porous rock permeability with confining pressure. Int J Rock Mech Min Sci Geomech Abstr 15:249–257. doi: 10.1016/0148-9062(78)90957-9

Garcia N, Stoll E (1984) Monte Carlo calculation for electromagnetic-wave scattering from random rough surfaces. Phys Rev Lett 52:1798–1801. doi: 10.1103/PhysRevLett.52.1798

Gaucher E, Schoenball M, Heidbach O, et al (2015) Induced seismicity in geothermal reservoirs: a review of forecasting approaches. Renew Sustain Energy Rev 52:. doi: 10.1016/j.rser.2015.08.026

Ge X, Ren J, Pu Y, et al (2001) Real-in time CT test of the rock meso-damage propagation law. Sci China Ser E Technol Sci 44:328–336. doi: 10.1007/bf02916710

Gentier S, Hopkins D, Riss J (2013) Role of fracture geometry in the evolution of flow paths under stress. In: Dynamics of Fluids in Fractured Rock. American Geophysical Union, pp 169–184

Ghanbarian B, Hunt AG, Ewing RP, Sahimi M (2013) Tortuosity in porous media: A critical review. Soil Sci Soc Am J 77:1461–1477. doi: 10.2136/sssaj2012.0435

Ghasemizadeh R, Hellweger F, Butscher C, et al (2012) Review: Groundwater flow and transport modeling of karst aquifers, with particular reference to the North Coast Limestone aquifer system of Puerto Rico. Hydrogeol J 20:1441–1461. doi: 10.1007/s10040-012-0897-4

Glover PWJ, Matsuki K, Hikima R, Hayashi K (1998) Synthetic rough fractures in rocks. J Geophys Res Solid Earth 103:9609–9620. doi: 10.1029/97JB02836

Goldbrunner J (2014) Hydrothermale Nutzung. In: Handbuch Tiefe Geothermie. Springer Spektrum, Berlin, Heidelberg, pp 223–244

Goldscheider N, Drew D (2007) Methods in karst hydrogeology. Taylor & Francis, London (UK)

Goodman RE (1976) Methods of geological engineering in discontinuous rocks. West Publishing Company, New York, NY

Grader AS, Balzarini M, Radaelli F, et al (2013) Fracture-Matrix Flow: Quantification and visualization using X-Ray computerized tomography. In: Dynamics of fluids in fractured rock. American Geophysical Union, Washington, D.C. (United States), pp 157–168

Greenwood JA, Williamson JBP (1966) Contact of nominally flat surfaces. Proc R Soc Lond Math Phys Eng Sci 295:300–319. doi: 10.1098/rspa.1966.0242

Gunnarsson I, Arnórsson S (2005) Impact of silica scaling on the efficiency of heat extraction from high-temperature geothermal fluids. Geothermics 34:320–329. doi: 10.1016/j.geothermics.2005.02.002

Hakami E (1995) Aperture distribution of rock fractures. Dissertation, Royal Institute of Technology (KTH)

Hakami E, Larsson E (1996) Aperture measurements and flow experiments on a single natural fracture. Int J Rock Mech Min Sci Geomech Abstr 33:395–404. doi: 10.1016/0148-9062(95)00070-4

Hansen A, Schmittbuhl J, Batrouni GG, de Oliveira FA (2000) Normal stress distribution of rough surfaces in contact. Geophys Res Lett 27:3639–3642. doi: 10.1029/2000gl011757

Harthong B, Scholtès L, Donzé F-V (2012) Strength characterization of rock masses, using a coupled DEM–DFN model. Geophys J Int 191:467–480. doi: 10.1111/j.1365-246X.2012.05642.x

Healy D, Rizzo RE, Cornwell DG, et al (2017) FracPaQ: A MATLAB™ toolbox for the quantification of fracture patterns. J Struct Geol 95:1–16. doi: 10.1016/j.jsg.2016.12.003

Heidbach O, Tingay M, Barth A, et al (2010) Global crustal stress pattern based on the World Stress Map database release 2008. Tectonophysics 482:3–15. doi: 10.1016/j.tecto.2009.07.023

Heinze T, Hamidi S (2017) Heat transfer and parameterization in local thermal non-equilibrium for dual porosity continua. Appl Therm Eng 114:645–652. doi: 10.1016/j.applthermaleng.2016.12.015

Heriawan MN, Koike K (2015) Coal quality related to microfractures identified by CT image analysis. Int J Coal Geol 140:97–110. doi: 10.1016/j.coal.2015.02.001

Hernqvist L, Butrón C, Fransson Å, et al (2012) A hard rock tunnel case study: Characterization of the water-bearing fracture system for tunnel grouting. Tunn Undergr Space Technol 30:132–144. doi: 10.1016/j.tust.2012.02.014

Hilgers C, Dilg-Gruschinski K, Urai JL (2004) Microstructural evolution of syntaxial veins formed by advective flow. Geology 32:261–264. doi: 10.1130/g20024.1

Hilgers C, Tenthorey E (2004) Fracture sealing of quartzite under a temperature gradient: experimental results. Terra Nova 16:173–178. doi: 10.1111/j.1365-3121.2004.00545.x

Hockney RW (1970) The potential calculation and some applications. In: Methods in Computational Physics - Advances in research and applications. Academic Press, New York, pp 135–211

Hopkins DL (2000) The implications of joint deformation in analyzing the properties and behavior of fractured rock masses, underground excavations, and faults. Int J Rock Mech Min Sci 37:175–202. doi: 10.1016/S1365-1609(99)00100-8

Hopkins DL, Cook NG, Myer LR (1987) Fracture stiffness and aperture as a function of applied stress and contact geometry. American Rock Mechanics Association, pp 673–680

Horne RN (1982) Geothermal Reinjection Experience in Japan. J Pet Technol 34:495–503. doi: 10.2118/9925-pa

Huber F, Enzmann F, Wenka A, et al (2012) Natural micro-scale heterogeneity induced solute and nanoparticle retardation in fractured crystalline rock. J Contam Hydrol 133:40–52. doi: 10.1016/j.jconhyd.2012.03.004

Hubert J, Emmerich H, Urai JL (2009) Modelling the evolution of vein microstructure with phase-field techniques – a first look. J Metamorph Geol 27:523–530. doi: 10.1111/j.1525-1314.2009.00839.x

Huerta NJ, Hesse MA, Bryant SL, et al (2016) Reactive transport of CO2-saturated water in a cement fracture: Application to wellbore leakage during geologic CO2 storage. Int J Greenh Gas Control 44:276–289. doi: 10.1016/j.ijggc.2015.02.006

Huo D (2015) Measuring fracture aperture and water saturation distributions using computed tomography and its application to modeling geomechanical impact on fluid flow in fractures. Dissertation, Stanford University

Huo D, Benson SM (2015) An experimental investigation of stress-dependent permeability and permeability hysteresis behavior in rock fractures. In: Faybishenko B, Benson SM, Gale JE (eds) Dynamics of Fluids and Transport in Complex Fractured-Porous Systems (Geophysical Monograph Series 210). John Wiley & Sons, Inc, Hoboken, NJ, pp 99–114

Huo D, Pini R, Benson S (2016) A calibration-free approach for measuring fracture aperture distributions using X-ray computed tomography. Geosphere 12:558–571. doi: 10.1130/GES01175.1

Hyun S, Pei L, Molinari JF, Robbins MO (2004) Finite-element analysis of contact between elastic self-affine surfaces. Phys Rev E 70:026117. doi: 10.1103/PhysRevE.70.026117

Ikeda S, Nakano T, Nakashima Y (2000) Three-dimensional study on the interconnection and shape of crystals in a graphic granite by X-ray CT and image analysis. Mineral Mag 64:945–959. doi: 10.1180/002646100549760

Iliev O, Laptev V (2004) On numerical simulation of flow through oil filters. Comput Vis Sci 6:139–146. doi: 10.1007/s00791-003-0118-8

Indraratna B, Kumara C, Zhu S-P, Sloan S (2015) Mathematical modeling and experimental verification of fluid flow through deformable rough rock joints. Int J Geomech 15:04014065. doi: 10.1061/(ASCE)GM.1943-5622.0000413

Ishibashi T, McGuire TP, Watanabe N, et al (2013) Permeability evolution in carbonate fractures: Competing roles of confining stress and fluid pH. Water Resour Res 49:2828–2842. doi: 10.1002/wrcr.20253

Ishibashi T, Watanabe N, Hirano N, et al (2012) GeoFlow: A novel model simulator for prediction of the 3-D channeling flow in a rock fracture network. Water Resour Res 48:6. doi: 10.1029/2011wr011226

Ito H, Kato K, Ochi Y, et al (2013) Fracture flow models of core samples by X-ray CT under pressure and numerical simulation. pp 387–389

Jackson RL, Green I (2011) On the modeling of elastic contact between rough surfaces. Tribol Trans 54:300–314. doi: 10.1080/10402004.2010.542277

Jaeger JC, Cook NGW, Zimmerman R (2007) Fundamentals of rock mechanics, 4th edn. Wiley-Blackwell, Malden, MA

Jain C, Vogt C, Clauser C (2015) Maximum potential for geothermal power in Germany based on engineered geothermal systems. Geotherm Energy 3:15. doi: 10.1186/s40517-015-0033-5

Janna WS (2010) Introduction to fluid mechanics. Boca Raton [etc.] : CRC Press, Taylor & Francis Group

Jing L (2003) A review of techniques, advances and outstanding issues in numerical modelling for rock mechanics and rock engineering. Int J Rock Mech Min Sci 40:283–353. doi: 10.1016/S1365-1609(03)00013-3

Jing L, Rutqvist J, Stephansson O, et al (1995) DECOVALEX - Mathematical models of coupled T-H-M processes for nuclear waste repositories: Report of phase III (SKI-R--95-80). Sweden

Jing L, Stephansson O (2007) Fundamentals of discrete element methods for rock engineering: Theory and applications, 1st edn. Elsevier, Amsterdam, The Netherlands

Jing Y, Armstrong RT, Mostaghimi P (2017) Rough-walled discrete fracture network modelling for coal characterisation. Fuel 191:442–453. doi: 10.1016/j.fuel.2016.11.094

Johns RA, Steude JS, Castanier LM, Roberts PV (1993) Nondestructive measurements of fracture aperture in crystalline rock cores using X ray computed tomography. J Geophys Res Solid Earth 98:1889–1900. doi: 10.1029/92jb02298

Johnson KL (1985) Contact mechanics. Cambridge University Press, Cambridge

Jung SJ, Prisbrey K, Wu G (1994) Prediction of rock hardness and drillability using acoustic emission signatures during indentation. Int J Rock Mech Min Sci Geomech Abstr 31:561–567. doi: 10.1016/0148-9062(94)90159-7

Kalker JJ, Randen YV (1972) A minimum principle for frictionless elastic contact with application to non-Hertzian half-space contact problems. J Eng Math 6:193–206. doi: 10.1007/BF01535102

Karpyn ZT, Alajmi A, Radaelli F, et al (2009) X-ray CT and hydraulic evidence for a relationship between fracture conductivity and adjacent matrix porosity. Eng Geol 103:139–145. doi: 10.1016/j.enggeo.2008.06.017

Katz O, Reches Z, Roegiers JC (2000) Evaluation of mechanical rock properties using a Schmidt Hammer. Int J Rock Mech Min Sci 37:723–728. doi: 10.1016/S1365-1609(00)00004-6

Kehrwald D (2004) Parallel lattice Boltzmann simulation of complex flows. Kaiserslautern

Keller AA (1997) High resolution cat imaging of fractures in consolidated materials. Int J Rock Mech Min Sci 34:155.e1-155.e16. doi: 10.1016/S1365-1609(97)00181-0

Keller AA, Roberts PV, Blunt MJ (1999) Effect of fracture aperture variations on the dispersion of contaminants. Water Resour Res 35:55–63. doi: 10.1029/1998wr900041

Ketcham RA (2010) Accurate three-dimensional measurements of features in geological materials from X-ray computed tomography data. In: Desrues J, Viggiani G, Besuelle P (eds) Advances in X-ray Tomography for Geomaterials. ISTE Ltd., London, UK, pp 143–148

Ketcham RA (2005) Three-dimensional grain fabric measurements using high-resolution X-ray computed tomography. J Struct Geol 27:1217–1228. doi: 10.1016/j.jsg.2005.02.006

Ketcham RA, Carlson WD (2001) Acquisition, optimization and interpretation of X-ray computed tomographic imagery: applications to the geosciences. Comput Geosci 27:381–400. doi: 10.1016/S0098-3004(00)00116-3

Ketcham RA, Slottke DT, Sharp Jr JM (2010) Three-dimensional measurement of fractures in heterogeneous materials using high-resolution X-ray computed tomography. Geosphere 6:498–514. doi: 10.1130/ges00552.1

Keusen H, Ganguin J, Schuler P, Buletti M (1989) Grimsel test site–Geology (Technical Report NTB 87-14E). Nagra, Wettingen, Switzerland

Khan F, Enzmann F, Kersten M, et al (2012) 3D simulation of the permeability tensor in a soil aggregate on basis of nanotomographic imaging and LBE solver. J Soils Sediments 12:86–96. doi: 10.1007/s11368-011-0435-3

Kim I, Lindquist W, Durham W (2003) Fracture flow simulation using a finite-difference lattice Boltzmann method. Phys Rev E 67:046708. doi: 10.1103/PhysRevE.67.046708

Kim J-S, Kwon S-K, Sanchez M, Cho G-C (2011) Geological storage of high level nuclear waste. KSCE J Civ Eng 15:721–737. doi: 10.1007/s12205-011-0012-8

Kirkby A, Heinson G (2017) Three-dimensional resistor network modeling of the resistivity and permeability of fractured rocks. J Geophys Res Solid Earth 122:2016JB013854. doi: 10.1002/2016JB013854

Kjørholt H, Broch E (1992) The water curtain—a successful means of preventing gas leakage from high-pressure, unlined rock caverns. Tunn Undergr Space Technol 7:127–132. doi: 10.1016/0886-7798(92)90042-G

Kling T, Huo D, Schwarz JO, et al (2016) Simulating stress-dependent fluid flow in a fractured core sample using real-time X-ray CT data. Solid Earth 7:1109–1124. doi: 10.5194/se-7-1109-2016

Kling T, Schwarz J-O, Wendler F, et al (2017) Fracture flow due to hydrothermally induced quartz growth. Adv Water Resour 107:93–107. doi: 10.1016/j.advwatres.2017.06.011

Kohl T, Hopkirk RJ (1995) "FRACure" - A simulation code for forced fluid flow and transport in fractured, porous rock. Geothermics 24:333–343. doi: 10.1016/0375-6505(95)00012-F

Kohl T, Mégel T (2007) Predictive modeling of reservoir response to hydraulic stimulations at the European EGS site Soultz-sous-Forêts. Int J Rock Mech Min Sci 44:1118–1131. doi: 10.1016/j.ijrmms.2007.07.022

Konzuk J, Kueper BH (2002) A study on the use of cubic-law based models for simulating flow through discrete rough-walled fractures. In: Proceedings of Fractured Rock Aquifers Conference. National Ground Water Association, Denver, United States, pp 132–136

Konzuk JS, Kueper BH (2004) Evaluation of cubic law based models describing single-phase flow through a rough-walled fracture. Water Resour Res 40:W02402. doi: 10.1029/2003wr002356

Kosakowski G (2004) Anomalous transport of colloids and solutes in a shear zone. J Contam Hydrol 72:23–46. doi: 10.1016/j.jconhyd.2003.10.005

Koyama T, Neretnieks I, Jing L (2008) A numerical study on differences in using Navier–Stokes and Reynolds equations for modeling the fluid flow and particle transport in single rock fractures with shear. Int J Rock Mech Min Sci 45:1082–1101. doi: 10.1016/j.ijrmms.2007.11.006

Kranz RL, Frankel AD, Engelder T, Scholz CH (1979) The permeability of whole and jointed Barre Granite. Int J Rock Mech Min Sci Geomech Abstr 16:225–234. doi: 10.1016/0148-9062(79)91197-5

Krevor SCM, Pini R, Zuo L, Benson SM (2012) Relative permeability and trapping of CO2 and water in sandstone rocks at reservoir conditions. Water Resour Res 48:W02532. doi: 10.1029/2011wr010859

Kulatilake PHSW, Panda BB (2000) Effect of block size and joint geometry on jointed rock hydraulics and REV. J Eng Mech 126:850–858. doi: 10.1061/(ASCE)0733-9399(2000)126:8(850)

Kulenkampff J, Gründig M, Richter M, Enzmann F (2008) Evaluation of positron-emission-tomography for visualisation of migration processes in geomaterials. Phys Chem Earth Parts ABC 33:937–942. doi: 10.1016/j.pce.2008.05.005

Kvartsberg S, Fransson Å (2013) Hydrogeological characterisation and stochastic modelling of a hydraulically conductive fracture system affected by grouting: A case study of horizontal circular drifts. Tunn Undergr Space Technol 38:38–49. doi: 10.1016/j.tust.2013.05.007

Lai C, Bodvarsson G, Witherspoon P (1985) Numerical studies of silica precipitation/dissolution. pp 279–286

Lander RH, Larese RE, Bonnell LM (2008) Toward more accurate quartz cement models: The importance of euhedral versus noneuhedral growth rates. AAPG Bull 92:1537–1563

Lander RH, Laubach SE (2015) Insights into rates of fracture growth and sealing from a model for quartz cementation in fractured sandstones. Geol Soc Am Bull 127:516–538. doi: 10.1130/b31092.1

Landry CJ, Karpyn ZT (2012) Single-phase lattice Boltzmann simulations of pore-scale flow in fractured permeable media. Int J Oil Gas Coal Technol 5:182–206. doi: 10.1504/IJOGCT.2012.046320

Lang PS, Paluszny A, Zimmerman RW (2015) Hydraulic sealing due to pressure solution contact zone growth in siliciclastic rock fractures. J Geophys Res Solid Earth 120:4080–4101. doi: 10.1002/2015jb011968

Lang PS, Paluszny A, Zimmerman RW (2016) Evolution of fracture normal stiffness due to pressure dissolution and precipitation. Int J Rock Mech Min Sci 88:12–22. doi: 10.1016/j.ijrmms.2016.06.004

Laubach SE (1988) Subsurface fractures and their relationship to stress history in East Texas basin sandstone. Tectonophysics 156:37–49. doi: 10.1016/0040-1951(88)90281-8

Laubach SE (2003) Practical approaches to identifying sealed and open fractures. AAPG Bull 87:561–579

Laubach SE, Reed RM, Olson JE, et al (2004) Coevolution of crack-seal texture and fracture porosity in sedimentary rocks: cathodoluminescence observations of regional fractures. J Struct Geol 26:967–982. doi: 10.1016/j.jsg.2003.08.019

Lavrov A (2017) Fracture permeability under normal stress: a fully computational approach. J Pet Explor Prod Technol 7:181–194. doi: 10.1007/s13202-016-0254-6

Lee SH, Yeo IW, Lee K-K, Detwiler RL (2015) Tail shortening with developing eddies in a rough-walled rock fracture. Geophys Res Lett 42:2015GL065116. doi: 10.1002/2015GL065116

Lei Q, Latham J-P, Tsang C-F (2017) The use of discrete fracture networks for modelling coupled geomechanical and hydrological behaviour of fractured rocks. Comput Geotech 85:151–176. doi: 10.1016/j.compgeo.2016.12.024

Leith W, Robertson E, Bryant B, Boden P (1991) Composition and physical properties of granitic rocks from the NRDC/SAS seismic station sites, Eastern Kazakh SSR. US Geological Survey, Reston, VA, United States

Lenoir N, Bornert M, Desrues J, et al (2007) Volumetric digital image correlation applied to X-ray microtomography images from triaxial compression tests on argillaceous rock. Strain 43:193–205. doi: 10.1111/j.1475-1305.2007.00348.x

Lespinasse M, Sausse J (2000) Quantification of fluid flow: hydro-mechanical behaviour of different natural rough fractures. J Geochem Explor 69–70:483–486. doi: 10.1016/S0375-6742(00)00111-4

Leu L, Berg S, Enzmann F, et al (2014) Fast X-ray micro-tomography of multiphase flow in Berea Sandstone: A sensitivity study on image processing. Transp Porous Media 105:451–469. doi: 10.1007/s11242-014-0378-4

Li B, Zhao Z, Jiang Y, Jing L (2015) Contact mechanism of a rock fracture subjected to normal loading and its impact on fast closure behavior during initial stage of fluid flow experiment. Int J Numer Anal Methods Geomech 39:1431–1449. doi: 10.1002/nag.2365

Li X, Huang H, Meakin P (2008) Level set simulation of coupled advection-diffusion and pore structure evolution due to mineral precipitation in porous media. Water Resour Res 44:n/a-n/a. doi: 10.1029/2007wr006742

Li Y, Chen Y-F, Zhang G-J, et al (2017) A numerical procedure for modeling the seepage field of water-sealed underground oil and gas storage caverns. Tunn Undergr Space Technol 66:56–63. doi: 10.1016/j.tust.2017.04.002

Li Y, Zhang Y (2015) Quantitative estimation of joint roughness coefficient using statistical parameters. Int J Rock Mech Min Sci 77:27–35. doi: 10.1016/j.ijrmms.2015.03.016

Lisjak A, Grasselli G (2014) A review of discrete modeling techniques for fracturing processes in discontinuous rock masses. J Rock Mech Geotech Eng. doi: 10.1016/j.jrmge.2013.12.007

Liu H-H, Wei M-Y, Rutqvist J (2013) Normal-stress dependence of fracture hydraulic properties including two-phase flow properties. Hydrogeol J 21:371–382. doi: 10.1007/s10040-012-0915-6

Liu W, Li Y, Wang B (2010) Gas permeability of fractured sandstone/coal samples under variable confining pressure. Transp Porous Media 83:333–347. doi: 10.1007/s11242-009-9444-8

Lomize G (1951) Flow in fractured rocks (in Russian). Gosenergoizdat Mosc 127

López DL, Smith L (1995) Fluid flow in fault zones: analysis of the interplay of convective circulation and topographically driven groundwater flow. Water Resour Res 31:1489–1503. doi: 10.1029/95WR00422

Louis C (1972) Rock hydraulics. In: Müller L (ed) Rock mechanics. Springer Vienna, Vienna, pp 299–387

Louis C (1967) Strömungsvorgänge in klüftigen Medien und ihre Wirkung auf die Standsicherheit von Bauwerken und Boeschungen im Fels. Dissertation, University of Karlsruhe

Love AEH (1929) The stress produced in a semi-infinite solid by pressure on part of the boundary. Philos Trans R Soc Lond Ser Contain Pap Math Phys Character 228:377–420. doi: 10.1098/rsta.1929.0009

Lowell RP, Van Cappellen P, Germanovich LN (1993) Silica precipitation in fractures and the evolution of permeability in hydrothermal upflow zones. Science 260:192–194. doi: 10.1126/science.260.5105.192

Madadi M, Sahimi M (2003) Lattice Boltzmann simulation of fluid flow in fracture networks with rough, self-affine surfaces. Phys Rev E 67:026309. doi: 10.1103/PhysRevE.67.026309

Malate RCM, O'Sullivan MJ (1992) Mathematical modelling of non-isothermal silica transport and deposition in a porous medium. Geothermics 21:519–544. doi: 10.1016/0375-6505(92)90005-T

Matsuki K, Chida Y, Sakaguchi K, Glover PWJ (2006) Size effect on aperture and permeability of a fracture as estimated in large synthetic fractures. Int J Rock Mech Min Sci 43:726–755. doi: 10.1016/j.ijrmms.2005.12.001

Matsuki K, Lee JJ, Sakaguchi K, Hayashi K (1999) Size effect in flow conductance of a closed small-scale hydraulic fracture in granite. Geotherm Sci Technol 6:113–138

Matsuki K, Wang EQ, Giwelli AA, Sakaguchi K (2008) Estimation of closure of a fracture under normal stress based on aperture data. Int J Rock Mech Min Sci 45:194–209. doi: 10.1016/j.ijrmms.2007.04.009

Mazumder S, Wolf KHAA, Elewaut K, Ephraim R (2006) Application of X-ray computed tomography for analyzing cleat spacing and cleat aperture in coal samples. Int J Coal Geol 68:205–222. doi: 10.1016/j.coal.2006.02.005

McClure M, Horne R (2011) Investigation of injection-induced seismicity using a coupled fluid flow and rate/state friction model. GEOPHYSICS 76:WC181-WC198. doi: 10.1190/geo2011-0064.1

Méheust Y, Schmittbuhl J (2001) Geometrical heterogeneities and permeability anisotropy of rough fractures. J Geophys Res Solid Earth 106:2089–2102. doi: 10.1029/2000jb900306

Meier S (2016) Fault zones in potential geothermal reservoir rocks in the Upper Rhine Graben: Characteristics, permeability implications, and numerical stress field models. Dissertation, Georg-August-Universität

Meller C, Bremer J, Ankit K, et al (2017) Integrated research as key to the development of a sustainable geothermal energy technology. Energy Technol 5:965–1006. doi: 10.1002/ente.201600579

Min K-B, Jing L, Stephansson O (2004) Determining the equivalent permeability tensor for fractured rock masses using a stochastic REV approach: Method and application to the field data from Sellafield, UK. Hydrogeol J 12:497–510. doi: 10.1007/s10040-004-0331-7

Miura H (2013) Anisotropy function of kinetic coefficient for phase-field simulations: Reproduction of kinetic Wulff shape with arbitrary face angles. J Cryst Growth 367:8–17. doi: 10.1016/j.jcrysgro.2013.01.014

Moeck IS (2014) Catalog of geothermal play types based on geologic controls. Renew Sustain Energy Rev 37:867–882. doi: 10.1016/j.rser.2014.05.032

Moelans N, Blanpain B, Wollants P (2008) An introduction to phase-field modeling of microstructure evolution. Calphad 32:268–294. doi: 10.1016/j.calphad.2007.11.003

Momber AW (2015) Fracture toughness effects in geomaterial solid particle erosion. Rock Mech Rock Eng 48:1573–1588. doi: 10.1007/s00603-014-0658-x

Moncada D, Mutchler S, Nieto A, et al (2012) Mineral textures and fluid inclusion petrography of the epithermal Ag–Au deposits at Guanajuato, Mexico: Application to exploration. J Geochem Explor 114:20–35. doi: 10.1016/j.gexplo.2011.12.001

Moore DE, Lockner DA, Byerlee JD (1994) Reduction of permeability in granite at elevated temperatures. Science 265:1558–1561. doi: 10.1126/science.265.5178.1558

Moore DE, Morrow CA, Byerlee JD (1983) Chemical reactions accompanying fluid flow through granite held in a temperature gradient. Geochim Cosmochim Acta 47:445–453. doi: 10.1016/0016-7037(83)90267-3

Morgan SP, Johnson CA, Einstein HH (2013) Cracking processes in Barre granite: fracture process zones and crack coalescence. Int J Fract 180:177–204. doi: 10.1007/s10704-013-9810-y

Morrow CA, Moore DE, Byerlee JD (1984) Permeability Changes in Crystalline Rocks Due to Temperature: Effects of Mineral Assemblage. MRS Online Proc Libr 44:null-null. doi: 10.1557/PROC-44-467

Morrow CA, Moore DE, Lockner DA (2001) Permeability reduction in granite under hydrothermal conditions. J Geophys Res Solid Earth 106:30551–30560. doi: 10.1029/2000jb000010

Mortensen J, Engstrom F, Lind I (1998) The relation among porosity, permeability, and specific surface of chalk from the Gorm field, Danish North Sea. SPE-31062-PA. doi: 10.2118/31062-pa

Mountassir GE, Lunn RJ, Moir H, MacLachlan E (2014) Hydrodynamic coupling in microbially mediated fracture mineralization: Formation of self-organized groundwater flow channels. Water Resour Res 50:1–16. doi: 10.1002/2013wr013578

Müller C, Siegesmund S, Blum P (2010) Evaluation of the representative elementary volume (REV) of a fractured geothermal sandstone reservoir. Environ Earth Sci 61:1713–1724. doi: 10.1007/s12665-010-0485-7

Muralidharan V, Chakravarthy D, Putra E, Schechter DS (2004) Investigating fracture Aperture distributions under various stress conditions using X-ray CT scanner. In: Canadian International Petroleum Conference. Petroleum Society of Canada, PETSOC, p 14

Nakashima Y (2013) The use of sodium polytungstate as an X-ray contrast agent to reduce the beam hardening artifact in hydrological laboratory experiments. J Hydrol Hydromech 61:347. doi: 10.2478/johh-2013-0043

Nakashima Y, Nakano T (2014) Optimizing contrast agents with respect to reducing beam hardening in nonmedical X-ray computed tomography experiments. J X-Ray Sci Technol 22:91–103. doi: 10.3233/xst-130411

National Research Council (1996) Rock Fractures and Fluid Flow: Contemporary Understanding and Applications. National Academy Press, Washington, D.C.

Nelson R (2001) Geologic analysis of naturally fractured reservoirs, 2nd edn. Gulf Professional Publishing, Houston, TX

Nemoto K, Watanabe N, Hirano N, Tsuchiya N (2009) Direct measurement of contact area and stress dependence of anisotropic flow through rock fracture with heterogeneous aperture distribution. Earth Planet Sci Lett 281:81–87. doi: 10.1016/j.epsl.2009.02.005

Neuman SP (1988) Stochastic continuum representation of fractured rock permeability as an alternative to the REV and fracture network concepts. In: Groundwater Flow and Quality Modelling. Springer, Dordrecht, pp 331–362

Neuville A, Toussaint R, Schmittbuhl J (2010) Hydrothermal coupling in a self-affine rough fracture. Phys Rev E 82:036317. doi: 10.1103/PhysRevE.82.036317

Newman TS, Yi H (2006) A survey of the marching cubes algorithm. Comput Graph 30:854–879. doi: 10.1016/j.cag.2006.07.021

Nicholl MJ, Rajaram H, Glass RJ, Detwiler R (1999) Saturated flow in a single fracture: evaluation of the Reynolds Equation in measured aperture fields. Water Resour Res 35:3361–3373. doi: 10.1029/1999WR900241

Noiriel C, Gouze P, Madé B (2013) 3D analysis of geometry and flow changes in a limestone fracture during dissolution. J Hydrol 486:211–223. doi: 10.1016/j.jhydrol.2013.01.035

Noiriel C, Madé B, Gouze P (2007) Impact of coating development on the hydraulic and transport properties in argillaceous limestone fracture. Water Resour Res 43:W09406. doi: 10.1029/2006WR005379

Nolte DD, Pyrak-Nolte LJ (1991) Stratified continuum percolation: Scaling geometry of hierarchical cascades. Phys Rev A 44:6320–6333. doi: 10.1103/PhysRevA.44.6320

Nolte DD, Pyrak-Nolte LJ, Cook NGW (1989) The fractal geometry of flow paths in natural fractures in rock and the approach to percolation. Pure Appl Geophys 131:111–138. doi: 10.1007/bf00874483

Ogilvie SR, Isakov E, Glover PWJ (2006) Fluid flow through rough fractures in rocks. II: A new matching model for rough rock fractures. Earth Planet Sci Lett 241:454–465. doi: 10.1016/j.epsl.2005.11.041

Ogilvie SR, Isakov E, Taylor CW, Glover PWJ (2003) Characterization of rough-walled fractures in crystalline rocks. Geol Soc Lond Spec Publ 214:125–141. doi: 10.1144/gsl.sp.2003.214.01.08

Oh J, Kim K-Y, Han WS, et al (2013) Experimental and numerical study on supercritical CO2/brine transport in a fractured rock: Implications of mass transfer, capillary pressure and storage capacity. Adv Water Resour 62, Part C:442–453. doi: 10.1016/j.advwatres.2013.03.007

Ohnishi Y, Chan T, Jing L (1996) Constitutive models for rock joints. In: Ove Stephansson, Lanru Jing, Tsang C-F (eds) Developments in Geotechnical Engineering. Elsevier, pp 57–92

Okamoto A, Saishu H, Hirano N, Tsuchiya N (2010) Mineralogical and textural variation of silica minerals in hydrothermal flow-through experiments: Implications for quartz vein formation. Geochim Cosmochim Acta 74:3692–3706. doi: 10.1016/j.gca.2010.03.031

Okamoto A, Sekine K (2011) Textures of syntaxial quartz veins synthesized by hydrothermal experiments. J Struct Geol 33:1764–1775. doi: 10.1016/j.jsg.2011.10.004

Oliver WC, Pharr GM (1992) An improved technique for determining hardness and elastic modulus using load and displacement sensing indentation experiments. J Mater Res 7:1564–1583. doi: 10.1557/jmr.1992.1564

Olsson R, Barton N (2001) An improved model for hydromechanical coupling during shearing of rock joints. Int J Rock Mech Min Sci 38:317–329. doi: 10.1016/S1365-1609(00)00079-4

Oron AP, Berkowitz B (1998) Flow in rock fractures - The local cubic law assumption reexamined. Water Resour Res 34:2811–2825. doi: 10.1029/98wr02285

Pabst W, Gregorova E (2013) Elastic properties of silica polymorphs-a review. Ceram-Silik 57:167–184

Pandey SN, Chaudhuri A, Rajaram H, Kelkar S (2015) Fracture transmissivity evolution due to silica dissolution/precipitation during geothermal heat extraction. Geothermics 57:111–126. doi: 10.1016/j.geothermics.2015.06.011

Paschen H, Oertel D, Grünwald R (2003) Possibilities of geothermal energy generation in Germany. Büro für Technikfolgen-Abschätzung beim Deutschen Bundestag, Berlin

Pastewka L, Prodanov N, Lorenz B, et al (2013) Finite-size scaling in the interfacial stiffness of rough elastic contacts. Phys Rev E 87:062809. doi: 10.1103/PhysRevE.87.062809

Pastewka L, Robbins MO (2016) Contact area of rough spheres: Large scale simulations and simple scaling laws. Appl Phys Lett 108:221601. doi: 10.1063/1.4950802

Pastewka L, Sharp TA, Robbins MO (2012) Seamless elastic boundaries for atomistic calculations. Phys Rev B 86:075459. doi: 10.1103/PhysRevB.86.075459

Patankar SV, Spalding DB (1972) A calculation procedure for heat, mass and momentum transfer in three-dimensional parabolic flows. Int J Heat Mass Transf 15:1787–1806. doi: 10.1016/0017-9310(72)90054-3

Patir N, Cheng HS (1978) An average flow model for determining effects of three-dimensional roughness on partial hydrodynamic lubrication. J Lubr Technol 100:12–17. doi: 10.1115/1.3453103

Pei L, Hyun S, Molinari JF, Robbins MO (2005) Finite element modeling of elasto-plastic contact between rough surfaces. J Mech Phys Solids 53:2385–2409. doi: 10.1016/j.jmps.2005.06.008

Peklenik J (1967) New developments in surface characterization and measurements by means of random process analysis. In: Proceedings of the institution of mechanical engineers: Properties and metrology of surfaces. Westminster, London, pp 108–126

Perrin J-C, Benson S (2010) An experimental study on the influence of sub-core scale heterogeneities on CO2 distribution in reservoir rocks. Transp Porous Media 82:93–109. doi: 10.1007/s11242-009-9426-x

Persson BNJ (2001) Theory of rubber friction and contact mechanics. J Chem Phys 115:3840–3861. doi: 10.1063/1.1388626

Persson BNJ (2007) Relation between interfacial separation and load: A general theory of contact mechanics. Phys Rev Lett 99:125502. doi: 10.1103/PhysRevLett.99.125502

Pfrang A, Schladitz K, Wiegmann A, Schimmel T (2007) Calculation of the evolution of surface area and free volume during the infiltration of fiber felts. Chem Vap Depos 13:705–715. doi: 10.1002/cvde.200706590

Pini R, Benson SM (2013) Simultaneous determination of capillary pressure and relative permeability curves from core-flooding experiments with various fluid pairs. Water Resour Res 49:3516–3530. doi: 10.1002/wrcr.20274

Pini R, Krevor SCM, Benson SM (2012) Capillary pressure and heterogeneity for the CO2/water system in sandstone rocks at reservoir conditions. Adv Water Resour 38:48–59. doi: 10.1016/j.advwatres.2011.12.007

Pippan R, Gumbsch P (2010) Multiscale modelling of plasticity and fracture by means of dislocation mechanics., 1st edn. Springer Science & Business Media, New York

Plenefisch T, Bönnemann C, Brückner L, et al (2015) Tiefe Geothermie - mögliche Umweltauswirkungen infolge hydraulischer und chemischer Stimualtion. Bundesanstalt für Geowissenschaften und Rohstoffe (BGR), Hannover

Polak A, Elsworth D, Yasuhara H, et al (2003) Permeability reduction of a natural fracture under net dissolution by hydrothermal fluids. Geophys Res Lett 30:2020. doi: 10.1029/2003GL017575

Polonsky IA, Keer LM (1999) A numerical method for solving rough contact problems based on the multi-level multi-summation and conjugate gradient techniques. Wear 231:206–219. doi: 10.1016/S0043-1648(99)00113-1

Poulet T, Paesold M, Veveakis M (2017) Multi-Physics Modelling of Fault Mechanics Using REDBACK: A Parallel Open-Source Simulator for Tightly Coupled Problems. Rock Mech Rock Eng 50:733–749. doi: 10.1007/s00603-016-0927-y

Power WL, Durham WB (1997) Topography of natural and artificial fractures in granitic rocks: Implications for studies of rock friction and fluid migration. Int J Rock Mech Min Sci 34:979–989. doi: 10.1016/S1365-1609(97)80007-X

Přikryl R (2006) Assessment of rock geomechanical quality by quantitative rock fabric coefficients: Limitations and possible source of misinterpretations. Eng Geol 87:149–162. doi: 10.1016/j.enggeo.2006.05.011

Pritchard G (1994) Anti-corrosion polymers: PEEK, PEKK and other polyaryls. Rapra Technology Ltd., Shawbury/Shrewsbury/Shropshire, UK

Pruess K (1983) Heat transfer in fractured geothermal reservoirs with boiling. Water Resour Res 19:201–208. doi: 10.1029/WR019i001p00201

Pudlo D, Henkel S, Enzmann F, et al (2014) The relevance of mineral mobilization and dissolution on the reservoir quality of sandstones in CO2 storage sites. Energy Procedia 59:390–396. doi: 10.1016/j.egypro.2014.10.393

Putnis A, Prieto M, Fernandez-Diaz L (1995) Fluid supersaturation and crystallization in porous media. Geol Mag 132:1–13. doi: 10.1017/S0016756800011389

Pyrak-Nolte LJ (1996) The seismic response of fractures and the interrelations among fracture properties. Int J Rock Mech Min Sci Geomech Abstr 33:787–802. doi: 10.1016/S0148-9062(96)00022-8

Pyrak-Nolte LJ, Morris JP (2000) Single fractures under normal stress: The relation between fracture specific stiffness and fluid flow. Int J Rock Mech Min Sci 37:245–262. doi: 10.1016/S1365-1609(99)00104-5

Pyrak-Nolte LJ, Nolte DD (2016) Approaching a universal scaling relationship between fracture stiffness and fluid flow. Nat Commun 7:10663. doi: 10.1038/ncomms10663

Qian J, Chen Z, Zhan H, Guan H (2011) Experimental study of the effect of roughness and Reynolds number on fluid flow in rough-walled single fractures: a check of local cubic law. Hydrol Process 25:614–622. doi: 10.1002/hyp.7849

Qian J, Zhan H, Luo S, Zhao W (2007) Experimental evidence of scale-dependent hydraulic conductivity for fully developed turbulent flow in a single fracture. J Hydrol 339:206–215. doi: 10.1016/j.jhydrol.2007.03.015

Qin RS, Bhadeshia HK (2010) Phase field method. Mater Sci Technol 26:803–811. doi: 10.1179/174328409X453190

Rabbani A, Ayatollahi S (2015) Comparing three image processing algorithms to estimate the grain-size distribution of porous rocks from binary 2D images and sensitivity analysis of the grain overlapping degree. Spec Top Rev Porous Media 6:71–89. doi: 10.1615/SpecialTopicsRevPorousMedia.v6.i1.60

Rabbani A, Ayatollahi S, Kharrat R, Dashti N (2016) Estimation of 3-D pore network coordination number of rocks from watershed segmentation of a single 2-D image. Adv Water Resour 94:264–277. doi: 10.1016/j.advwatres.2016.05.020

Rabbani A, Jamshidi S (2014) Specific surface and porosity relationship for sandstones for prediction of permeability. Int J Rock Mech Min Sci 71:25–32. doi: 10.1016/j.ijrmms.2014.06.013

Rabbani A, Jamshidi S, Salehi S (2014) Determination of specific surface of rock grains by 2D imaging. J Geol Res 2014:7. doi: 10.1155/2014/945387

Rangel-German E, Akin S, Castanier L (2006) Multiphase-flow properties of fractured porous media. J Pet Sci Eng 51:197–213. doi: 10.1016/j.petrol.2005.12.010

Rasouli V, Hosseinian A (2011) Correlations developed for estimation of hydraulic parameters of rough fractures through the simulation of JRC flow channels. Rock Mech Rock Eng 44:447–461. doi: 10.1007/s00603-011-0148-3

Raven KG, Gale JE (1985) Water flow in a natural rock fracture as a function of stress and sample size. Int J Rock Mech Min Sci Geomech Abstr 22:251–261. doi: 10.1016/0148-9062(85)92952-3

Re F, Scavia C (1999) Determination of contact areas in rock joints by X-ray computer tomography. Int J Rock Mech Min Sci 36:883–890. doi: 10.1016/S0148-9062(99)00056-X

Ren J, Ge X (2004) Computerized tomography examination of damage tests on rocks under triaxial compression. Rock Mech Rock Eng 37:83–93. doi: 10.1007/s00603-003-0007-y

Renard F, Candela T (2017) Scaling of fault roughness and implications for earthquake mechanics. In: Thomas rion Y, Mitchell TM, Bhat HS (eds) Fault Zone Dynamic Processes. John Wiley & Sons, Inc., pp 195–215

Renshaw CE (1995) On the relationship between mechanical and hydraulic apertures in rough-walled fractures. J Geophys Res Solid Earth 100:24629–24636. doi: 10.1029/95jb02159

Robinson BA, Pendergrass J (1989) A combined heat transfer and quartz dissolution/deposition model for a hot dry rock geothermal reservoir. In: Proceedings of the 14th workshop on geothermal reservoir engineering. Stanford, California, p 6

Rogers S, Elmo D, Dunphy R, Bearinger D (2010) Understanding hydraulic fracture geometry and interactions in the Horn River Basin through DFN and numerical modeling. In: Canadian Unconventional Resources and International Petroleum Conference. Society of Petroleum Engineers, Calgary, Alberta, p 12

Ross TP, Rose AW, Poulson SR (1994) Pore fluid chemistry of a pressure seal zone, Moore-Sams-Morganza gas field, Tuscaloosa Trend, Louisiana. In: Ortoleva PJ (ed) Basin Compartements and Seals. American Association of Petroleum Geologists, Tulsa, Oklahoma, pp 139–149

Rubio-Maya C, Ambríz Díaz VM, Pastor Martínez E, Belman-Flores JM (2015) Cascade utilization of low and medium enthalpy geothermal resources − A review. Renew Sustain Energy Rev 52:689–716. doi: 10.1016/j.rser.2015.07.162

Rücker M, Berg S, Armstrong RT, et al (2015) From connected pathway flow to ganglion dynamics. Geophys Res Lett 42:3888–3894. doi: 10.1002/2015gl064007

Rutqvist J (2011) Status of the TOUGH-FLAC simulator and recent applications related to coupled fluid flow and crustal deformations. Comput Geosci 37:739–750. doi: 10.1016/j.cageo.2010.08.006

Rutqvist J, Bäckström A, Chijimatsu M, et al (2009) A multiple-code simulation study of the long-term EDZ evolution of geological nuclear waste repositories. Environ Geol 57:1313–1324. doi: 10.1007/s00254-008-1536-1

Rutqvist J, Leung C, Hoch A, et al (2013a) Linked multicontinuum and crack tensor approach for modeling of coupled geomechanics, fluid flow and transport in fractured rock. J Rock Mech Geotech Eng 5:18–31. doi: 10.1016/j.jrmge.2012.08.001

Rutqvist J, Rinaldi AP, Cappa F, Moridis GJ (2013b) Modeling of fault reactivation and induced seismicity during hydraulic fracturing of shale-gas reservoirs. J Pet Sci Eng 107:31–44. doi: 10.1016/j.petrol.2013.04.023

Rutqvist J, Stephansson O (2003) The role of hydromechanical coupling in fractured rock engineering. Hydrogeol J 11:7–40. doi: 10.1007/s10040-002-0241-5

Rutqvist J, Tsang C-F (2003) Analysis of thermal–hydrologic–mechanical behavior near an emplacement drift at Yucca Mountain. J Contam Hydrol 62:637–652. doi: 10.1016/S0169-7722(02)00184-5

Sahimi M (2011) Flow and transport in porous media and fractured rock: from classical methods to modern approaches. John Wiley & Sons, Weinheim, Germany

Saishu H, Okamoto A, Tsuchiya N (2014) The significance of silica precipitation on the formation of the permeable–impermeable boundary within Earth's crust. Terra Nova 26:253–259. doi: 10.1111/ter.12093

Sanjuan B, Millot R, Innocent C, et al (2016) Major geochemical characteristics of geothermal brines from the Upper Rhine Graben granitic basement with constraints on temperature and circulation. Chem Geol 428:27–47. doi: 10.1016/j.chemgeo.2016.02.021

Santos J, Vargas E, Barroso E, et al (2010) Studies of mechanisms associated with sand production using X-ray CT scan. In: Desrues J, Viggiani G, Besuelle P (eds) Advances in X-ray Tomography for Geomaterials. ISTE Ltd., London, UK, pp 199–205

Schembre JM, Kovscek AR (2003) A technique for measuring two-phase relative permeability in porous media via X-ray CT measurements. J Pet Sci Eng 39:159–174. doi: 10.1016/S0920-4105(03)00046-9

Schild M, Siegesmund S, Vollbrecht A, Mazurek M (2001) Characterization of granite matrix porosity and pore-space geometry by in situ and laboratory methods. Geophys J Int 146:111–125. doi: 10.1046/j.0956-540x.2001.01427.x

Schill E, Meixner J, Meller C, et al (2016) Criteria and geological setting for the generic geothermal underground research laboratory, GEOLAB. Geotherm Energy 4:7. doi: 10.1186/s40517-016-0049-5

Schmidt R, Seithel R, Stober I (2016) Verbundvorhaben „Störtief": die Rolle von tiefreichenden Störungszonen bei der geothermischen Energienutzung; Teilprojekt 3: Südwestdeutschland. Karlsruher Institut für Technologie (KIT), Karlsruhe

Schmittbuhl J, Steyer A, Jouniaux L, Toussaint R (2008) Fracture morphology and viscous transport. Int J Rock Mech Min Sci 45:422–430. doi: 10.1016/j.ijrmms.2007.07.007

Schulte T, Zimmermann G, Vuataz F, et al (2010) Enhancing Geothermal Reservoirs. In: Huenges E (ed) Geothermal Energy Systems. Wiley-VCH Verlag GmbH & Co. KGaA, pp 173–243

Schulz V, Kehrwald D, Wiegmann A, Steiner K (2005) Flow, heat conductivity, and gas diffusion in partly saturated microstructures. In: Proceedings of NAFEMS CFD Seminar: Simulation of complex flows. Niedernhausen/Wiesbaden, Germany

Schwarz J-O, Enzmann F (2013) Simulation of fluid flow on fractures and implications for reactive transport simulations. Transp Porous Media 96:501–525. doi: 10.1007/s11242-012-0103-0

Searle OB, Pfeiffer RH (1985) Victrex® poly(ethersulfone) (PES) and Victrex® poly(etheretherketone) (PEEK). Polym Eng Sci 25:474–476. doi: 10.1002/pen.760250808

Seiedi O, Rahbar M, Nabipour M, et al (2011) Atomic Force Microscopy (AFM) investigation on the surfactant wettability alteration mechanism of aged mica mineral surfaces. Energy Fuels 25:183–188. doi: 10.1021/ef100699t

Sekerka RF (2005) Equilibrium and growth shapes of crystals: how do they differ and why should we care? Cryst Res Technol 40:291–306. doi: 10.1002/crat.200410342

Settgast RR, Fu P, Walsh SDC, et al (2017) A fully coupled method for massively parallel simulation of hydraulically driven fractures in 3-dimensions. Int J Numer Anal Methods Geomech 41:627–653. doi: 10.1002/nag.2557

Shi J-Q, Xue Z, Durucan S (2009) History matching of CO2 core flooding CT scan saturation profiles with porosity dependent capillary pressure. Energy Procedia 1:3205–3211. doi: 10.1016/j.egypro.2009.02.104

Shimizu T (2014) Reinterpretation of quartz textures in terms of hydrothermal fluid evolution at the Koryu Au-Ag deposit, Japan. Econ Geol 109:2051–2065. doi: 10.2113/econgeo.109.7.2051

Singhal BBS, Gupta RP (2010) Applied hydrogeology of fractured rocks. Springer Science & Business Media

Singurindy O, Berkowitz B (2005) The role of fractures on coupled dissolution and precipitation patterns in carbonate rocks. Adv Water Resour 28:507–521. doi: 10.1016/j.advwatres.2005.01.002

Snow DT (1965) A parallel plate model of fractured permeable media. Dissertation, University of California (UC)

Souley M, Lopez P, Boulon M, Thoraval A (2015) Experimental hydromechanical characterization and numerical modelling of a fractured and porous sandstone. Rock Mech Rock Eng 48:1143–1161. doi: 10.1007/s00603-014-0626-5

Sousa LMO (2014) Petrophysical properties and durability of granites employed as building stone: a comprehensive evaluation. Bull Eng Geol Environ 73:569–588. doi: 10.1007/s10064-013-0553-9

Soyk D (2015) Diagenesis and reservoir quality of the Lower and Middle Buntsandstein (Lower Triassic), SW Germany. Dissertation, Ruprecht-Karls-University

Stanley HM, Kato T (1997) An FFT-based method for rough surface contact. J Tribol 119:481–485. doi: 10.1115/1.2833523

Steefel CI, Appelo C a. J, Arora B, et al (2015) Reactive transport codes for subsurface environmental simulation. Comput Geosci 19:445–478. doi: 10.1007/s10596-014-9443-x

Steefel CI, Molins S, Trebotich D (2013) Pore scale processes associated with subsurface CO2 injection and sequestration. Rev Mineral Geochem 77:259–303. doi: 10.2138/rmg.2013.77.8

Steiner U, Savvatis A, Böhm F, Schubert A (2014) Explorationsstrategie tiefer geothermischer Ressourcen am Beispiel des süddeutschen Oberjuras (Malm). In: Handbuch Tiefe Geothermie. Springer Spektrum, Berlin, Heidelberg, pp 429–461

Stille H, Gustafson G, Hassler L (2012) Application of new theories and technology for grouting of dams and foundations on rock. Geotech Geol Eng 30:603–624. doi: 10.1007/s10706-012-9512-7

Stober I, Jodocy M (2009) Eigenschaften geothermischer Nutzhorizonte im baden-württembergischen und französischen Teil des Oberrheingrabens. Grundwasser 14:127–137. doi: 10.1007/s00767-009-0103-3

Sun H (2012a) A practical MATLAB program for multifractal interpolation surface. In: 2012 8th International Conference on Natural Computation. IEEEXplore, Chongqing, Sichuan, China, pp 909–913

Sun H (2012b) The theory of fractal interpolated surface and its MATLAB Program. In: 2012 IEEE Symposium on Electrical Electronics Engineering (EEESYM). IEEEXplore, Kuala Lumpur, Malaysia, pp 231–234

Swain MV, Lawn BR (1976) Indentation fracture in brittle rocks and glasses. Int J Rock Mech Min Sci Geomech Abstr 13:311–319. doi: 10.1016/0148-9062(76)91830-1

Swan G (1983) Determination of stiffness and other joint properties from roughness measurements. Rock Mech Rock Eng 16:19–38. doi: 10.1007/bf01030216

Tan JC, Cheetham AK (2011) Mechanical properties of hybrid inorganic-organic framework materials: establishing fundamental structure-property. relationships. Chem Soc Rev 40:1059–1080. doi: 10.1039/c0cs00163e

Tatone BA, Grasselli G (2015) Characterization of the effect of normal load on the discontinuity morphology in direct shear specimens using X-ray micro-CT. Acta Geotech 10:31–54. doi: 10.1007/s11440-014-0320-5

Tatone BSA, Grasselli G (2012a) An Investigation of Discontinuity Roughness Scale Dependency Using High-Resolution Surface Measurements. Rock Mech Rock Eng 46:657–681. doi: 10.1007/s00603-012-0294-2

Tatone BSA, Grasselli G (2012b) Quantitative measurements of fracture aperture and directional roughness from rock cores. Rock Mech Rock Eng 45:619–629. doi: 10.1007/s00603-011-0219-5

Tenthorey E, Cox SF, Todd HF (2003) Evolution of strength recovery and permeability during fluid–rock reaction in experimental fault zones. Earth Planet Sci Lett 206:161–172. doi: 10.1016/S0012-821X(02)01082-8

Tokan-Lawal A, Prodanović M, Landry CJ, Eichhubl P (2017) Influence of numerical cementation on multiphase displacement in rough fractures. Transp Porous Media 116:275–293. doi: 10.1007/s11242-016-0773-0

Toublanc A, Renaud S, Sylte JE, et al (2005) Ekofisk Field: fracture permeability evaluation and implementation in the flow model. Pet Geosci 11:321–330. doi: 10.1144/1354-079304-622

Tsang C-F (1991) Coupled hydromechanical-thermochemical processes in rock fractures. Rev Geophys 29:537–551. doi: 10.1029/91rg01832

Tsang C-F, Neretnieks I (1998) Flow channeling in heterogeneous fractured rocks. Rev Geophys 36:275–298. doi: 10.1029/97rg03319

Tsang C-F, Stephansson O (1996) A conceptual introduction to coupled thermo-hydro-mechanical processes in fractured rocks. In: Stephansson O, Jing L, Tsang C-F (eds) Developments in Geotechnical Engineering. Elsevier, pp 1–24

Tsang YW (1984) The effect of tortuosity on fluid flow through a single fracture. Water Resour Res 20:1209–1215. doi: 10.1029/WR020i009p01209

Tsang YW, Tsang CF (1989) Flow channeling in a single fracture as a two-dimensional strongly heterogeneous permeable medium. Water Resour Res 25:2076–2080. doi: 10.1029/WR025i009p02076

Tsuchiyama A, Uesugi K, Nakano T, Ikeda S (2005) Quantitative evaluation of attenuation contrast of X-ray computed tomography images using monochromatized beams. Am Mineral 90:132–142. doi: 10.2138/am.2005.1552

Tuğrul A, Zarif IH (1999) Correlation of mineralogical and textural characteristics with engineering properties of selected granitic rocks from Turkey. Eng Geol 51:303–317. doi: 10.1016/S0013-7952(98)00071-4

Ulusay R, Erguler ZA (2012) Needle penetration test: Evaluation of its performance and possible uses in predicting strength of weak and soft rocks. Eng Geol 149:47–56. doi: 10.1016/j.enggeo.2012.08.007

Van Doormaal JP, Raithby GD (1984) Enhancements of the simple method for predicting incompressible fluid flows. Numer Heat Transf 7:147–163. doi: 10.1080/01495728408961817

Van Geet M, Swennen R (2001) Quantitative 3D-fracture analysis by means of microfocus X-ray computer tomography (μCT) - An example from coal. Geophys Res Lett 28:3333–3336. doi: 10.1029/2001gl013247

van Genabeek O, Rothman DH (1999) Critical behavior in flow through a rough-walled channel. Phys Lett A 255:31–36. doi: 10.1016/S0375-9601(99)00152-8

Vandersteen K, Busselen B, Van Den Abeele K, Carmeliet J (2003) Quantitative characterization of fracture apertures using microfocus computed tomography. Geol Soc Lond Spec Publ 215:61–68. doi: 10.1144/gsl.sp.2003.215.01.06

Vidal J, Genter A, Schmittbuhl J (2015) How do permeable fractures in the Triassic sediments of Northern Alsace characterize the top of hydrothermal convective cells? Evidence from Soultz geothermal boreholes (France). Geotherm Energy 3:8. doi: 10.1186/s40517-015-0026-4

Viles H, Goudie A, Grab S, Lalley J (2011) The use of the Schmidt Hammer and Equotip for rock hardness assessment in geomorphology and heritage science: a comparative analysis. Earth Surf Process Landf 36:320–333. doi: 10.1002/esp.2040

Vinegar HJ, De Waal JA, Wellington SL (1991) CT studies of brittle failure in castlegate sandstone. Int J Rock Mech Min Sci Geomech Abstr 28:441–450. doi: 10.1016/0148-9062(91)90082-W

Vogler D (2016) Hydro-mechanically coupled processes in heterogeneous fractures: experiments and numerical simulations. Dissertation, ETH Zurich

Vogler D, Amann F, Bayer P, Elsworth D (2016a) Permeability evolution in natural fractures subject to cyclic loading and gouge formation. Rock Mech Rock Eng 49:3463–3479. doi: 10.1007/s00603-016-1022-0

Vogler D, Settgast RR, Annavarapu C, et al (2016b) Hydro-mechanically coupled flow through heterogeneous fractures. In: Proceedings of the 41st Workshop on Geothermal Reservoir Engineering. Stanford University (California), SGP-TR-209

Vogler D, Settgast RR, Annavarapu C, et al (2018) Experiments and simulations of fully hydro-mechanically coupled response of rough fractures exposed to high pressure fluid injection. J Geophys Res Solid Earth 123. doi: 10.1002/2017JB015057

Vogler D, Walsh SDC, Bayer P, Amann F (2017) Comparison of surface properties in natural and artificially generated fractures in a crystalline rock. Rock Mech Rock Eng 50:2891–2909. doi: 10.1007/s00603-017-1281-4

Walsh JB (1981) Effect of pore pressure and confining pressure on fracture permeability. Int J Rock Mech Min Sci Geomech Abstr 18:429–435. doi: 10.1016/0148-9062(81)90006-1

Walsh JB, Brace WF (1984) The effect of pressure on porosity and the transport properties of rock. J Geophys Res Solid Earth 89:9425–9431. doi: 10.1029/JB089iB11p09425

Walsh JB, Brown SR, Durham WB (1997) Effective media theory with spatial correlation for flow in a fracture. J Geophys Res Solid Earth 102:22587–22594. doi: 10.1029/97jb01895

Walsh R, McDermott C, Kolditz O (2008) Numerical modeling of stress-permeability coupling in rough fractures. Hydrogeol J 16:613. doi: 10.1007/s10040-007-0254-1

Wang HF (2000) Theory of linear poroelasticity with applications to geomechanics and hydrogeology. Princeton University Press, Princeton, NJ

Wang L, Cardenas MB (2016) Development of an empirical model relating permeability and specific stiffness for rough fractures from numerical deformation experiments. J Geophys Res Solid Earth 121:4977–4989. doi: 10.1002/2016jb013004

Wang L, Cardenas MB, Slottke DT, et al (2015) Modification of the local cubic law of fracture flow for weak inertia, tortuosity, and roughness. Water Resour Res 51:2064–2080. doi: 10.1002/2014wr015815

Watanabe N, Hirano N, Tamagawa T, et al (2005) Numerical estimation of aperture structure and flow wetted field in rock fracture. Geotherm Resour Counc Trans 29:431–436

Watanabe N, Hirano N, Tsuchiya N (2008) Determination of aperture structure and fluid flow in a rock fracture by high-resolution numerical modeling on the basis of a flow-through experiment under confining pressure. Water Resour Res 44:W06412. doi: 10.1029/2006wr005411

Watanabe N, Hirano N, Tsuchiya N (2009) Diversity of channeling flow in heterogeneous aperture distribution inferred from integrated experimental-numerical analysis on flow through shear fracture in granite. J Geophys Res Solid Earth 114:B04208. doi: 10.1029/2008jb005959

Watanabe N, Ishibashi T, Ohsaki Y, et al (2011) X-ray CT based numerical analysis of fracture flow for core samples under various confining pressures. Eng Geol 123:338–346. doi: 10.1016/j.enggeo.2011.09.010

Watanabe N, Ishibashi T, Tsuchiya N, et al (2013) Geologic core holder with a CFR PEEK body for the X-ray CT-based numerical analysis of fracture flow under confining pressure. Rock Mech Rock Eng 46:413–418. doi: 10.1007/s00603-012-0311-5

Watanabe N, Numakura T, Sakaguchi K, et al (2017) Potentially exploitable supercritical geothermal resources in the ductile crust. Nat Geosci 10:140–144. doi: 10.1038/ngeo2879

Weerakone WMSB, Wong RCK (2010) Characterization of variable aperture rock fractures using X-ray computer tomography. In: Desrues J, Viggiani G, Besuelle P (eds) Advances in X-ray Tomography for Geomaterials. ISTE LTd., London, UK, pp 229–235

Wehrens P, Baumberger R, Berger A, Herwegh M (2017) How is strain localized in a meta-granitoid, mid-crustal basement section? Spatial distribution of deformation in the central Aar massif (Switzerland). J Struct Geol 94:47–67. doi: 10.1016/j.jsg.2016.11.004

Weibel R, Olivarius M, Kristensen L, et al (2017) Predicting permeability of low-enthalpy geothermal reservoirs: A case study from the Upper Triassic – Lower Jurassic Gassum Formation, Norwegian–Danish Basin. Geothermics 65:135–157. doi: 10.1016/j.geothermics.2016.09.003

Weissbrod T, Sneh A (2002) Sedimentology and paleogeography of the Late Precambrian-Early Cambrian arkosic and conglomeratic facies in the northern margins of the Arabo-Nubian Shield. Geological Survey of Israel, Jerusalem

Wen H, Li L, Crandall D, Hakala A (2016) Where lower calcite abundance creates more alteration: Enhanced rock matrix diffusivity induced by preferential dissolution. Energy Fuels 30:4197–4208. doi: 10.1021/acs.energyfuels.5b02932

Wendler F, Mennerich C, Nestler B (2011) A phase-field model for polycrystalline thin film growth. J Cryst Growth 327:189–201. doi: 10.1016/j.jcrysgro.2011.04.044

Wendler F, Okamoto A, Blum P (2015) Phase-field modeling of epitaxial growth of polycrystalline quartz veins in hydrothermal experiments. Geofluids 16:211–230. doi: 10.1111/gfl.12144

Wernecke C, Marsch K (2015) Mapping Rock Surface Roughness with Photogrammetry. In: 64th ISRM Regional Symposium - EUROCK 2015. International Society for Rock Mechanics, Salzburg, Austria, p 6

Whitaker S (1986) Flow in porous media I: A theoretical derivation of Darcy's law. Transp Porous Media 1:3–25. doi: 10.1007/bf01036523

Winchell H (1945) The Knoop microhardness tester as a mineralogical tool. Am Mineral 30:583–595

Witherspoon PA, Wang JSY, Iwai K, Gale JE (1980) Validity of cubic law for fluid flow in a deformable rock fracture. Water Resour Res 16:1016–1024. doi: 10.1029/WR016i006p01016

Wu W, Sharma MM (2017) A model for the conductivity and compliance of unpropped fractures. In: SPE Hydraulic Fracturing Technology Conference and Exhibition. Society of Petroleum Engineers, SPE, p 29

Xanke J (2017) Managed aquifer recharge into a karst groundwater system at the Wala reservoir, Jordan. Dissertation, Karlsruhe Institute of Technology (KIT)

Xie LZ, Gao C, Ren L, Li CB (2015) Numerical investigation of geometrical and hydraulic properties in a single rock fracture during shear displacement with the Navier–Stokes equations. Environ Earth Sci 73:7061–7074. doi: 10.1007/s12665-015-4256-3

Xiong X, Li B, Jiang Y, et al (2011) Experimental and numerical study of the geometrical and hydraulic characteristics of a single rock fracture during shear. Int J Rock Mech Min Sci 48:1292–1302. doi: 10.1016/j.ijrmms.2011.09.009

Yang C, Persson BNJ (2008) Contact mechanics: contact area and interfacial separation from small contact to full contact. J Phys Condens Matter 20:215214. doi: 10.1088/0953-8984/20/21/215214

Yang Z, Niemi A, Fagerlund F, Illangasekare T (2013) Two-phase flow in rough-walled fractures: Comparison of continuum and invasion-percolation models. Water Resour Res 49:993–1002. doi: 10.1002/wrcr.20111

Yasuhara H, Kinoshita N, Ohfuji H, et al (2011) Temporal alteration of fracture permeability in granite under hydrothermal conditions and its interpretation by coupled chemo-mechanical model. Appl Geochem 26:2074–2088. doi: 10.1016/j.apgeochem.2011.07.005

Yasuhara H, Polak A, Mitani Y, et al (2006) Evolution of fracture permeability through fluid–rock reaction under hydrothermal conditions. Earth Planet Sci Lett 244:186–200. doi: 10.1016/j.epsl.2006.01.046

Ye Z, Liu H-H, Jiang Q, Zhou C (2015) Two-phase flow properties of a horizontal fracture: The effect of aperture distribution. Adv Water Resour 76:43–54. doi: 10.1016/j.advwatres.2014.12.001

Yoon H, Valocchi AJ, Werth CJ, Dewers T (2012) Pore-scale simulation of mixing-induced calcium carbonate precipitation and dissolution in a microfluidic pore network. Water Resour Res 48:n/a-n/a. doi: 10.1029/2011wr011192

Yoshioka N (1994a) Elastic behavior of contacting surfaces under normal loads: A computer simulation using three-dimensional surface topographies. J Geophys Res Solid Earth 99:15549–15560. doi: 10.1029/94jb00938

Yoshioka N (1994b) The role of plastic deformation in normal loading and unloading cycles. J Geophys Res Solid Earth 99:15561–15568. doi: 10.1029/94jb00931

Zeeb C, Göckus D, Bons P, et al (2010) Fracture flow modelling based on satellite images of the Wajid Sandstone, Saudi Arabia. Hydrogeol J 18:1699–1712. doi: 10.1007/s10040-010-0609-x

Zeeb C, Gomez-Rivas E, Bons PD, et al (2013a) Fracture network evaluation program (FraNEP): A software for analyzing 2D fracture trace-line maps. Comput Geosci 60:11–22. doi: 10.1016/j.cageo.2013.04.027

Zeeb C, Gomez-Rivas E, Bons PD, Blum P (2013b) Evaluation of sampling methods for fracture network characterization using outcrops. AAPG Bull 97:1545–1566. doi: 10.1306/02131312042

Zhang X, Sanderson DJ (1995) Anisotropic features of geometry and permeability in fractured rock masses. Eng Geol 40:65–75. doi: 10.1016/0013-7952(95)00040-2

Zhao J (1997) Joint surface matching and shear strength part A: joint matching coefficient (JMC). Int J Rock Mech Min Sci 34:173–178. doi: 10.1016/S0148-9062(96)00062-9

Zhao Z, Jing L, Neretnieks I (2012) Particle mechanics model for the effects of shear on solute retardation coefficient in rock fractures. Int J Rock Mech Min Sci 52:92–102. doi: 10.1016/j.ijrmms.2012.03.001

Zhao Z, Jing L, Neretnieks I, Moreno L (2011) Analytical solution of coupled stress-flow-transport processes in a single rock fracture. Comput Geosci 37:1437–1449. doi: 10.1016/j.cageo.2011.02.015

Zhao Z, Li B, Jiang Y (2014) Effects of fracture surface roughness on macroscopic fluid flow and solute transport in fracture networks. Rock Mech Rock Eng 47:2279–2286. doi: 10.1007/s00603-013-0497-1

Zhou XP, Zhang YX, Ha QL (2008) Real-time computerized tomography (CT) experiments on limestone damage evolution during unloading. Theor Appl Fract Mech 50:49–56. doi: 10.1016/j.tafmec.2008.04.005

Zichella L, Bellopede R, Marini P, et al (2017) Diamond wire cutting: A methodology to evaluate stone workability. Mater Manuf Process 1–7. doi: 10.1080/10426914.2016.1269912

Zimmerman R, Bodvarsson G (1996) Hydraulic conductivity of rock fractures. Transp Porous Media 23:1–30. doi: 10.1007/bf00145263

Zimmerman RW (1985) The effect of microcracks on the elastic moduli of brittle materials. J Mater Sci Lett 4:1457–1460. doi: 10.1007/bf00721363

Zimmerman RW, Chen D-W, Cook NGW (1992) The effect of contact area on the permeability of fractures. J Hydrol 139:79–96. doi: 10.1016/0022-1694(92)90196-3

Zimmerman RW, Kumar S, Bodvarsson GS (1991) Lubrication theory analysis of the permeability of rough-walled fractures. Int J Rock Mech Min Sci Geomech Abstr 28:325–331. doi: 10.1016/0148-9062(91)90597-F

Zimmerman RW, Yeo I-W (2013) Fluid flow in rock fractures: From the Navier-Stokes equations to the cubic law. In: Faybishenko B, Witherspoon PA, Gale JE (eds) Dynamics of fluids in fractured rock (Geophysical Monograph Series 162). American Geophysical Union, Washington, D.C., pp 213–224

Zimmermann G, Reinicke A (2010) Hydraulic stimulation of a deep sandstone reservoir to develop an Enhanced Geothermal System: Laboratory and field experiments. Geothermics 39:70–77. doi: 10.1016/j.geothermics.2009.12.003

Zou L, Jing L, Cvetkovic V (2015) Roughness decomposition and nonlinear fluid flow in a single rock fracture. Int J Rock Mech Min Sci 75:102–118. doi: 10.1016/j.ijrmms.2015.01.016

Publications

Journal publications (peer-reviewed)

Kling, T., Huo, D., Schwarz, J. O., Enzmann, F., Benson, S., and Blum, P. (2016): Simulating stress-dependent fluid flow in a fractured core sample using real-time X-ray CT data, Solid Earth, 7, doi:1109-1124, 10.5194/se-7-1109-2016.

Kling, T., Schwarz, J.-O., Wendler, F., Enzmann, F., and Blum, P. (2017): Fracture flow due to hydrothermally induced quartz growth, *Advances in Water Resources*, 107, 93-107, doi:10.1016/j.advwatres.2017.06.011.

Kling, T., Vogler, D., Pastewka, L., Amann, F. and Blum, P.: Contact mechanical simulations of a granodiorite fracture, *Rock Mechanics and Rock Engineering* [under review].

Meller, C., Bremer, J., Ankit, K., Baur, S., Bergfeldt, T., Blum, P., Canic, T., Eiche, E., Gaucher, E., Hagenmeyer, V., Heberling, F., Held, S., Herfurth, S., Isele, J., Kling, T., Kuhn, D., Mayer, D., Müller, B., Nestler, B., Neumann, T., Nitschke, F., Nothstein, A., Nusiaputra, Y., Orywall, P., Peters, M., Sahara, D., Schäfer, T., Schill, E., Schilling, F., Schröder, E., Selzer, M., Stoll, M., Wiemer, H.-J., Wolf, S., Zimmermann, M., and Kohl, T. (2017): Integrated research as key to the development of a sustainable geothermal energy technology., *Energy Technology*, 5, doi:965-1006, 10.1002/ente.201600579.

Reports

Urai, J. L., Virgo, S., Arndt, M., Abe, S., Enzmann, F., Schwarz, J. O., Gomez-Rivas, E., Varga-Vass, A., Pataki-Rood, M., Blum, P., Kling, T., Bons, P. D., Sachau, T., and Koehn, D. (2016): Mineral vein dynamics modelling (FRACS II) - DGMK Research Report 718-2, German Society for Petroleum and Coal Science and Technology (DGMK), Hamburg, 227 pages.

Conference proceedings

Kraml, M., Ochmann, N., Leible, D., Kling, T., Chiragwile, S.A., Jodocy, M., Kreuter, H. & GPT Exploration Team (2014): Results of the pre-feasibility study on Ngozi Geothermal Project in Tanzania, *5th African Rift Geothermal Conference*, Arusha (Tanzania), 27 October - 2 November, 10 pages.

Kling, T., Schwarz, J. O., Wendler, F., Enzmann, F., and Blum, P. (2016): Quartz-driven fracture healing and its impact on fluid flow, *European Geothermal Congress (EGC)*, Strasbourg (France), 19-23 September, 5 pages (presented as poster).

Conference abstracts

Kling, T., Huo, D., Schwarz, J. O., Enzmann, F., Blum, P., and Benson, S. (2014): Numerical simulation of fluid flow in a single fracture under loading and unloading conditions, 47th *American Geophysical Union (AGU) Fall Meeting*, San Francisco (United States), 15-19 December, (presented as poster).

Kling, T., Huo, D., Schwarz, J. O., Enzmann, F., Benson, S., and Blum, P. (2016): CT-basierte numerische Simulationen druckabhängiger Fluidflüsse in einem geklüfteten porösen Sandstein, *25. Tagung der FH-DGGV „Grundwasser – Mensch- Ökosysteme“*, Karlsruhe (Germany), 13-17 April, (presented as talk).

Kling, T., Schwarz, J.-O., Wendler, F., Enzmann, F., and Blum, P. (2017): Hydraulic apertures of open and sealing fractures, *6th International Conference on Coupled THCM Processes in Geosystems (GeoProc)*, Paris (France), 5-7 July, (presented as talk).